UNIVERSIDAD AUTÓNOMA DE BAJA CALIFORNIA

INSTITUTO DE INGENIERÍA

MAESTRÍA Y DOCTORADO EN CIENCIAS E INGENIERÍA

"THEORETICAL METHOD TO INCREASE THE SPEED OF CONTINUOUS MAPPING IN A THREE-DIMENSIONAL LASER SCANNING SYSTEM USING SERVOMOTORS CONTROL"

TESIS PARA OBTENER EL GRADO DE:
DOCTOR EN CIENCIAS

PRESENTA
LARS LINDNER

Dr. OLEG SERGIYENKO
Dr. JULIO C. RODRIGUEZ-QUIÑONEZ

Mexicali, B. C. ***Enero, 2017***

Acknowledgments

First of all, I would like to express my sincere and deeply gratitude to my Ph.D. advisor Dr. Oleg Sergiyenko for many stimulating discussions and ideas during my 3.5 year doctoral thesis. His help and instructions have always given me new ideas and certitude throughout my time of studies.

Furthermore, I would like to thank my co-advisor Dr. Julio C. Rodríguez-Quiñonez for many practical support and ideas over the years and to provide me with good comments for my scientific writings.

Besides my advisors, I also would like to thank the rest of my thesis committee, namely: Dr. Moisés Rivas-López, Dr. Daniel Hernández-Balbuena and Dr. Luis Carlos Básaca-Preciado.

My sincere thanks also go to the Universidad Autónoma de Baja California, for the doctoral program MyDCI and for both directors of the Instituto de Ingeníeria Dr. Benjamin Valdez-Salas and Dr. Gisela Montero-Alpirez for giving me access to the laboratory and research facility.

At last, I also want thank my parents for supporting me over all the years and back me up for any problem, which cannot be resolved scientifically.

Resumen

de la Tesis de Lars Lindner, presentada como requisito parcial para la obtención del grado de DOCTOR EN CIENCIAS, EN EL AREA DE ELECTRONICA, Mexicali, Baja California, México. Enero de 2017.

MÉTODO TEÓRICO PARA AUMENTAR LA VELOCIDAD DEL MAPEO CONTINÚO DE UN ESCÁNER LASER TRIDIMENSIONAL USANDO CONTROL DE SERVOMOTORES

Resumen aprobado por:

Dr. Oleg Sergiyenko

Escáneres de láser son dispositivos de escaneo ópticos, que miden la topografía de una superficie por escaneo físico de láser usando un punto de luz que se mueve sobre una superficie. En el Instituto de Ingeniería de la UABC se desarrolló un nuevo Sistema Técnica de Visión (STV), que consiste principalmente en un sistema de escaneo láser usando triangulación dinámica, para obtener coordenadas 3D de cualquier objeto examinado. Para determinar estas coordenadas 3D, el antecesor STV prototipo No.2 utiliza motores de pasos, lo que resulta en desventajas importantes, debido al comportamiento discreto de estos tipos de actuadores. Los motores de pasos resultan un campo de visión discreto, cuya resolución depende de la distancia del objeto examinado y zonas muertas inevitables, donde no se pueden detectar las coordenadas 3D. El presente trabajo describe la sustitución de estos actuadores discretos por motores de corriente continua (CC), para eliminar zonas muertas y realizar un escaneo láser continuo en el campo de visión del STV. El objetivo principal del presente trabajo es el desarrollo de todos los formalismos teóricos requeridos para ofrecer el escaneo láser en modo continuo. El uso de motores CC como actuadores en el nuevo STV prototipo No.3 elimina las desventajas de un campo de visión discreto, sustituyéndolo por un campo continuo. Al cambiar el principio de funcionamiento físico de discreto a continuo, se habilita la implementación de aplicaciones, que anteriormente estaban limitadas por el tamaño fijo de pasos o por la distancia del objeto observado. Usando motores CC en lugar de motores de pasos, se puede lograr un tiempo de posicionamiento reducido significativo, manteniendo el error de posicionamiento relativo menos del 1 por ciento. En este trabajo y para el STV prototipo No.3 se

describen los algoritmos de control para el control de posición y velocidad de motores CC en bucle cerrada y en bucle abierto y se implementan usando un controlador digital. Se derivan conceptos importantes del controlador digital, que son necesarios cuando se controla la posición y la velocidad del eje del motor CC. Estos conceptos se consideran para la implementación práctica del control de posición y velocidad del motor CC. Se realizan experimentaciones extensas para controlar el ángulo del eje del motor del motor CC propuesto, para lograr un tiempo de subida de control mínimo y un error de posición angular mínimo. Los resultados de la experimentación se resumen en forma tabular y se analizan con detalle. Mostrando en general la veracidad total de las hipótesis preliminares definidas, así como algunas desviaciones prácticas que están analizadas y las que ayudan a reforzar el diseño final práctico.

Abstract

of the thesis, presented by Lars Lindner, in order to obtain the DOCTOR IN SCIENCES, ELECTRICAL AREA, Mexicali, Baja California, México. January, 2017.

THEORETICAL METHOD TO INCREASE THE SPEED OF CONTINUOUS MAPPING IN A THREE-DIMENSIONAL LASER SCANNING SYSTEM USING SERVOMOTORS CONTROL

Approved by:

Dr. Oleg Sergiyenko

Laser scanners are optical scanning devices, which measure surface topography using physical laser scanning by light spot moving across a surface. A novel Technical Vision System (TVS) was developed at the Engineering Institute of UABC, which mainly consists in a laser scanning system using dynamic triangulation, to obtain 3D coordinates of any examined object. To determine this 3D coordinates, the TVS predecessor prototype No.2 uses stepping motors, which result in major disadvantages, due to the discrete behavior of these types of actuators. Stepping motors leads to a discrete field of view (FOV), which resolution depends on the distance to the examined object, and inevitable dead zones, where 3D coordinates cannot be detected. Present work describes the substitution of these discrete actuators by DC Motors, to eliminate dead zones and to perform a continuous laser scan in the TVS FOV. The main objective of present work is the development of all required theoretical formalism to provide laser scanning in continuous mode. Using DC motors as actuators in the new TVS successor prototype No.3 eliminates the disadvantages of a discrete FOV and replaces it with a continuous one. By changing the physical operation principle from discrete to continuous, the implementation of applications gets available, which previously were limited by the fixed step size or by the observed object distance. Using DC instead of stepping motors, a significant reduced positioning time can be accomplished, maintaining the relative positioning error less than 1 per cent. For the TVS prototype No.3 the control algorithms for position and speed control of DC motors in closed and open-loop configuration are described in this work and implemented using digital controller. Important concepts of digital controller are derived, which are necessary when controlling the position and speed of the DC motor shaft. These concepts

are considered for practical implementation of the DC motor position and speed control. Extensive experimentations are realized to control the DC motor shaft angle of the proposed DC motor, to achieve a minimal step response rising time and a minimal angular position error. The experimentation results are summarized in tabular form and analyzed in detail. They show in overall the total correctness of the preliminary defined hypotheses, as well as some practical deviations are analyzed, which helps to enforce the final practical design.

Objectives

The general objective is represented by the creation of a novel theoretical method for continuous laser scanning of a Technical Vision System (TVS), based on closed-loop Direct-Current Motor (DC Motor) control using digital controller. This TVS, researched and further developed in this thesis, represents a laser scanning system, which by using the Dynamic Triangulation measurement method determines 3D coordinates of *n* points on the surface of any examined object with preliminary defined accuracy and during reasonable time. In order to achieve this general objective, in present thesis are achieved the next particular objectives:

1. Definition of a novel physical principle of laser beam propulsion, which aim to achieve the possibility to position a laser beam on any position in a continuous field of view (FOV) and using any arbitrary trajectory.
2. Definition of a scanning element, to convert the discontinued FOV into continuous one, which thereby defines a novel geometrical strategy for detecting 3D coordinates of any examined object.
3. Substitution of previously used Stepping Motors by DC motors, to eliminate dead zones in the FOV and to perform a continuous laser scan in the scanning field of laser scanner system.
4. Development and implementation of an algorithm for positioning the laser beam in the FOV using digital controllers and Direct-Current Motors (DC Motors) in open and closed-loop configuration.
5. Use of linear control theory and the Routh Criterion, to proof the stability of the DC motor continuous model for different controller parameters and for different control loop configurations using simulation.
6. Design of digital controller algorithm using various parameters and constants, to control position and speed of the proposed DC motor shaft, which is the basic principle needed to perform a continuous laser scan of dynamic triangulation.
7. The different algorithms for positioning the laser beam are experimentally tested and proved, using comparing values as the laser beam position accuracy / precision and step response rising time after control.
8. The Taguchi Statistical Method shall be used to design and realize the experimentations, to approve the novel physical principle of a continuous laser scan in the TVS FOV.

List of Figures

List of Tables

List of Symbols

L_A	Armature inductance	φ_e, Φ_e	Angular position error	a	TVS base distance
R_A	Armature resistance	φ_∞	Final angular position	b	Striking distance
K_E	Armature gain	φ_e'	Relative angular error	c	Receiving distance
T_E	Electrical time constant	$\bar{\varphi}_e'$	Relative angular error average	d	Object distance
K_T	Torque constant	t_{rise}	Step response rising time	d'	Object distance projection
r	Motor damping	$\bar{t}_{rise}$	Step response rising time average	β	SA angle
J	Total moment of inertia	ρ_o	Actual counted pulses	γ	PL angle
T_M	Mechanical time constant	K_{ref}	Reference value for relative position error calculation	η	TVS vertical angle
J_R	Rotor moment of inertia	K_{emp}	Empirical constant	$f(x)$	Real polynomial
J_{Mi}	Mirror moment of inertia	K_{PWM}	Resolution of PWM signal	$f(s)$	Complex polynomial
ω_0	Characteristic angular frequency	i_{max}	Maximum iteration number	n	Degree of polynomial
ω_c	Cutoff angular frequency	τ	PWM on time	k	Zeros with positive real part
D	Damping	f_{PWM}	PWM frequency	P_k	Real polynomial
K_R	Amplification factor of positioning algorithm	T_{PWM}	PWM period	Q_k	Polynomial divisor
$\overline{K}_R$	Upper limit of amplification factor	d	PWM duty cycle	$V(\tilde{x})$	Number of sign changes
$\overline{K}_{R_{min}}$	Minimum value of $\overline{K}_R$	d_{const}	Constant PWM duty cycle	$V_{-\infty}$	Number of negative sign changes
$\overline{K}_{R_{max}}$	Maximum value of $\overline{K}_R$	d_{var}	Variable PWM duty cycle	$V_{+\infty}$	Number of positive sign changes

T_N	Controller reset time	$y(t)$	Controller output variable	$G(s)$	Transfer function
u_A, U_A	Armature voltage	y_{φ_r}	Controller output variable for $K_{ref} = \varphi_r$	$N(s)$	Transfer function nominator
u_N, U_N	Nominal voltage	y_{360}	Controller output variable for $K_{ref} = 360$	$D(s)$	Transfer function denominator
U_{op}	Operating voltage	y'	Relative controller output variable+	a_n	Real polynomial coefficients
i_A, I_A	Armature current	f_P	Standard reference signal frequency	s_n	Polynomial zero
i_N, I_N	Nominal current	T_P	Standard reference signal period	z_n	Complex number
M	Motor torque	$f_{2\pi}$	Zero sensor signal frequency	$\widetilde{\omega}$	Point of discontinuity
M_f	Friction torque	$T_{2\pi}$	Full revolution period	ε	Neighborhood
$\omega_{\mathrm{N}}, \Omega_N$	Nominal angular speed	$N_{2\pi}$	Full revolution pulse number	$H(s)$	S&H element
$\omega_{\mathrm{o}}, \Omega_o$	Actual angular speed	$\bar{f}_{2\pi}$	Zero sensor mean value	T_S	Sampling period
$\omega_{\mathrm{m}}, \Omega_m$	Measured angular speed	$\epsilon_{2\pi}$	Zero sensor error value	f_S	Sampling rate
ω_r, Ω_r	Reference angular speed	ϵ	Absolute measurement error	$f(t)$	Continuous time signal
ω_e, Ω_e	Angular speed error	ϵ'	Relative measurement error	t_k	Discrete time points
φ_o, Φ_o	Actual angular position	T_A	Time phase shift	f_{CPU}	CPU clock rate
φ_m, Φ_m	Measured angular position	N_A	SA angle pulse number	BOTTOM	Timer zero value
φ_r, Φ_r	Reference angular position	T_{serial}	Serial communication execution period	TOP	Timer maximum value

List of Abbreviations

AC	Alternating Current
ADC	Analog Digital Converter
AMR	Autonomous Mobile Robot
CCD	Charge Coupled Device
CCW	Counterclockwise
CMM	Coordinate Measuring Machine
CMOS	Complementary Metal Oxide Semiconductor
COMPA	Compare Match Interrupt
CPU	Central Processing Unit
CTC	Clear Timer on Compare match
CW	Clockwise
DAC	Digital Analog Converter
DC	Direct Current
DMD	Digital Micro Mirror Devices
FOM	Field Of Motion
FOV	Field Of View
GUI	Graphical Unit Interface
IC	Integrated Circuit
IR	Infrared
ISP	In System Programming
LCD	Liquid-crystal display
MAE	Mean Absolute Error
MOSFET	Metal Oxide Semiconductor Field Effect Transistor
OCR	Output Compare Register
OST	Optical Scanning Tomography
PCB	Printed Circuit Board
PL	Positioning Laser
ppr	Pulses per revolution
PWM	Pulse Width Modulation
RISC	Reduced Instruction Set Computing
RX	Receive
SA	Scanning Aperture
SD	Standard Deviation
TF	Transfer Function

TOV	Timer Overflow Interrupt
TTL	Transistor Transistor Logic
TVS	Technical Vision System
TX	Transmit
UABC	Autonomous University of Baja California
USART	Universal Synchronous and Asynchronous serial Receiver and Transmitter
US	Ultrasonic Sensor

List of Equations

List of Trademarks

Arduino

Atmel

AVR

C#

Futaba

Matlab / Simulink

Maxon Motors

Microsoft

1 Introduction

Geodesy is the science of measuring and mapping the earth's surface, including its geometric form, its gravity field and its orientation in space [1]. It is part of engineering science and connects astronomy with geophysics. Especially Topography, which represents the engineering of land measurement and delimitation of surfaces, is also involved in the determination of geometric parameters (position, shape, size) and its derivative with respect to time (speed, acceleration) [2]. Part of the work of topographers is measurement of 3D Coordinates, which is a great need and used in modern science and industry. The main task is to determine coordinates of an examined object, which is mainly realized by optical methods in a very large amount of applications.

For example paper [3] describes a concept of large 3D structure measurement using four portable high-accurate tracking laser interferometers. Each of these interferometers tracks a single moving retroreflector and sends their data to a central control, which calculates the 3D point coordinates using Pythagorean´s Theorem in space. An optical scanning tomography (OST) for time-resolved measurements of kinematic fields in the volume of structures is presented in paper [4]. This tomography uses a plane laser beam, which illuminates a transparent probe in layers and the scattered light of each layer is recorded with a single camera then. Another example for determination of 3D coordinates is introduced in paper [5], where a coordinate-measuring machine (CMM) is combined with two CCD-cameras to perform 3D inspections of complex and freeform surfaces. This hybrid system uses a new development in coordinate unification, to merge the measured data of tactile and optical sensors. Measuring 3D coordinates using a non-diffracting beam is presented in paper [6]. It is also used a combined system with a laser beam and an optical system to measure the attitude angle of a probe. A 3D shape measurement system which uses digital micro-mirror devices (DMD) with high-speed refreshing rate is proposed in paper [7]. A DMD chip contains a large amount of individual microscopic mirrors, in which every mirror represents one pixel in the projected or scanned image. These mirrors can be rotated on high speed, which allows a superfast 3D shape measurement. Another application of 3D coordinate measurement can be found in laser welding used within the automotive industry [8]. The main objective is to monitor the welding conditions online, in order to guarantee a constant product quality. A panoramic fringe projection system to retrieve the three-dimensional topography of quasi-cylindrical objects is demonstrated in paper [9]. Thereby the examined object is located in a conical mirror and gets illuminated by a LCD projector. Then, the reflected light from the conical mirror is observed using a CCD camera over a 45° staggered beam splitter. Paper [10] shows the possibility for stereo measurements with one CCD camera, using a biprism between an observed object and the camera. The biprism in front of the camera split the scene into two equivalent lateral stereo views, which get captured by the two halves of the CCD sensor. This approach allows a compact set-up suitable for miniaturization. Also measurement of 3D coordinates is needed in small applications, where a specific parameter, like the diameter of a machine shaft, has to be determined [11]. Thereby the two edges of the shaft are projected into a world coordinate system, using the parameters of the camera model.

Applications for contactless measurement of 3D coordinates use mostly optical signals with CCD cameras or laser signals in Laser Scanning Systems [12]. Cameras have the advantage that they resemble the way of human vision [13], which makes it easy to implement algorithms for different scenario detection in an unknown environment. Also, the scanning results do not depend of the examined object surface properties, when using cameras. On the other side, cameras are not preferable for single coordinate measurements (e.g. distance), due to their large amount of data generation. Another disadvantage is their dependency from the condition and existence of visible light and from atmospheric effects. Laser scanning systems however are suited for accurate coordinate measurements, which they can perform from objects in long distances and independent of ambient light. They also have the advantage of a fast measuring speed and a simple optical arrangement among low cost [14]. On the other hand, it must be noted, that for laser scanning systems the measurement readings depend from the scanning surface and that post-processing is required, due to large and high resolution 3D data sets.

One application, where measurement of 3D coordinates is absolutely needed, can be found in the movement control of Autonomous and Mobile Robots (AMR). The environment of a robot is typically measured with CCD cameras and / or laser scanning systems. In paper [15] for example a robot is navigated using a „visual potential“, which is computed using a sequence-capturing of various images by a camera mounted on the robot. Paper [16] uses an automatic expert system for 3D terrain reconstruction, which captures his environment with two cameras in a stereoscopic way, similar to the human binocular vision. Laser scanning systems, as remote sensing technology, instead are known as Light Detection and Ranging (Lidar) systems, which are widely used in many areas, as well as in mobile robot navigation. Paper [17] for example uses an algorithm and terrestrial mobile Lidar data, to compute the left and right road edge of a route corridor. In paper [18], a mobile robot is equipped with a Lidar-system, which, using the time-of-flight principle, navigates in a cornfield.

However, other sensors and methods are also used to navigate mobile robots. Paper [19] for example uses infrared (IR) and ultrasonic sensors (US) for map building and object location of a mobile robot prototype. One ultrasonic rotary sensor is installed on the top and a ring of 16 infrared sensors are distributed in eight pairs around the perimeter of the robot. These IR sensors are based on the direct measurement of the IR light magnitude that is back-scattered from a surface placed in front of the sensor. The typical response time of these IR sensors for a distance measurement is about $2ms$. Distance measurement with this sensor can be realized from a few centimeters to $1m$, which represents one limitation of this approach. The range for coordinate measurements by triangulation can be far over $1m$. Paper [20] even experiments with a chaotic controlled mobile robot, which only uses an ultrasonic distance sensor for short-range measurement to avoid obstacle collision. The experimental results show applicability of chaotic systems to real autonomous mobile robots.

An optical 3D laser scanning system for navigation of autonomous mobile robots, called Technical Vision System (TVS), was developed at the Laboratory of Optoelectronics and Automated Measurement of the Autonomous University of Baja California [13]. This TVS consists mainly in a laser scanning system, which uses the Dynamic Triangulation Method, to obtain 3D coordinates of any object under observation. This developed autonomous robot navigation system has his main task in prevention of obstacle collision in an unknown environment. More work on the robot navigation system can be found in [21], [22], [23], [24], [25], [26], [27] and extensive preliminary research about the TVS can be found in [28], [29], [30], [31], [32], [33], [34], [35], [36], [37], [38], [39], [40] and [41]. Another application of the TVS was explored in the medical field, where it can be used to monitor scoliosis [42], [43] and [44]. Thereby 3D coordinates of the human spine are measured, in order to classify deformations using the Cobb Angle. More recent research about increasing the scanning speed of the TVS by use of combined variable steps can be found in [45]. Also a power spectrum centroid for measurement improvement got applied in paper [46].

All this applications use the same indicated TVS, which performs line-by-line laser scans using Stepping Motors to positioning the emitted laser. Stepping motors have a discontinuous behavior, due to their stepwise rotation of the motor shaft. Modern stepping motors in certain operating modes have step sizes less than one degree, but will always have unreachable angles in their field of motion (FOM). It is proposed the substitution of these stepping motors by Direct-Current Motors

(DC Motors), to eliminate Dead Zones and to perform a continuous scan in the TVS field-of-view (FOV). These motors will be controlled as Servomotors in closed and open-loop configuration. Thus, by use of stepping motors in the previous developed TVS, the FOV is discretized and its resolution depends on the distance of the examined scanning object. Targets, which have dimensions less than the FOV resolution in a certain distance, cannot be scanned or captured. These targets are located within the dead zones of the TVS and thereby not detectable by the same. Also previous work [45] has shown the possibility to optimize the laser scanning speed by variation of the scanning step angle, in dependency on the scenario to be scanned and the required quantity of information. Because of their physical construction, stepping motors always have a fixed step angle and thereby cannot be used to implement a variable step scanning method. In order to improve these serious disadvantages, the present work offers the substitution of the stepping motors by DC Motors and it derives additional theoretical aspects to be considered, which gets its solution along this work.

Thereby, present work is organized as follows. After introduction, the following chapter 2 presents basic concepts needed, to design, develop and realize the new successor TVS prototype. Chapter 3 gives the theoretical concepts, needed to model and analyze the stability of the proposed DC motors in position and speed control-loop. The next chapter 4 uses these theoretical concepts to define continuous models for the DC motor position and speed closed-loop control and derives the step response for both control loops. Following chapter 5 describes in detail the main concept needed, to control a DC motor using digital controllers. The predecessor prototype No.2 of the defined Technical Vision System and his successor prototype No.3 are explained in chapter 6. Next chapter 7 defines the main issues detected in the TVS prototype No.2 and gives new approaches to counter these issues. The practical implementation of DC motor position control is described in chapter 8 and the experimental realization and results are presented in chapter 9. An extensive experimental analysis of DC motor position control is given in chapter 10 and chapter 11 closes the work with some conclusions and perspectives for further research.

2 Basic Concepts

Basic concepts must be defined for design, development and realization of the proposed TVS prototype No.3. Thereby, present chapter describes the principal measurement method of triangulation, compares the static with dynamic triangulation and defines the transition from a discrete to a continuous laser scanner FOV. It also contains the description of electromechanical actuators, which are currently used in the presented TVS, represented by stepping, DC and servomotors. The advantages and disadvantages of each actuator are presented and shown that servomotors are best suited for the task of dead zone elimination in the TVS FOV. Finally, the used programming environments and hardware are briefly described, to implement and the required control tasks for the proposed servomotors.

2.1 Laser Scanning Methods

Optical laser scanning systems currently use three major methods to determine 3D coordinates: Measuring of elapsed time (Time-of-flight), Measuring of phasing and Triangulation. An overview of the advantages of these methods gives Table 2-1:

Table 2-1: Methods for 3D coordinate measurement

Method	Advantages	Disadvantages	Range
Time-of-flight	Short reaction time. No optical aperture angle.	Expensive for high resolution.	1m – some kilometers
Phasing	Less technical effort for high resolution.	Less measuring distance. Ambiguous for distance more than half wavelength.	Depends of the frequency
Triangulation	Cost-efficient and robust.	Depends of the surface.	1µm – 100m

Previous research [13], [21] – [46] has shown the advantage of the TVS, which use the triangulation method over the other two methods. Paper [21] explains the disadvantages of multisensory systems, of stereo vision systems and systems which use structured light methods. The TVS represents a low-cost and high-precision vision system with sufficient reliability as a main characteristic. The TVS is achieving the following functions, which are specified in paper [13]:

- Detection of objects and their classification
- 3D coordinates measurement of detected objects
- Determination of information about the scanned objects surfaces

2.1.1 Triangulation

Triangulation consists in division and measuring an area by triangles, which form a mesh and where angles and distances are calculated using trigonometric functions [27]. To measure 3D coordinates using triangulation, be considered a triangle in top view (Figure 2-1) and lateral view (Figure 2-2), where the distances d, d', p and q are unknown:

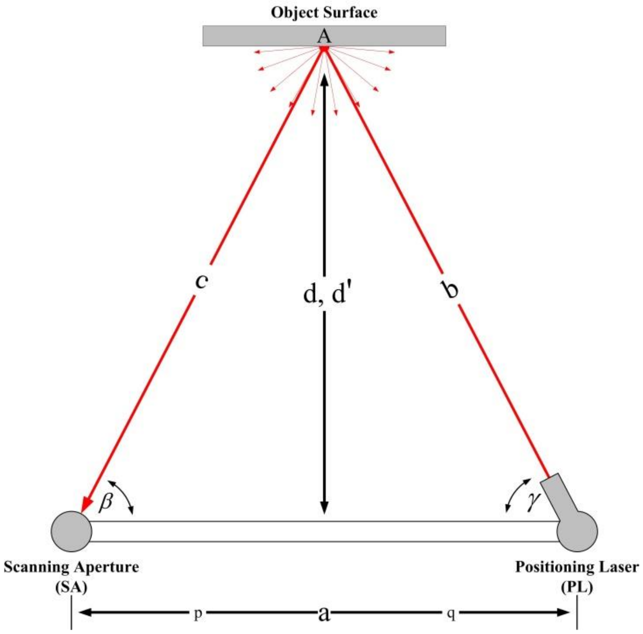

Figure 2-1: Triangle in top view

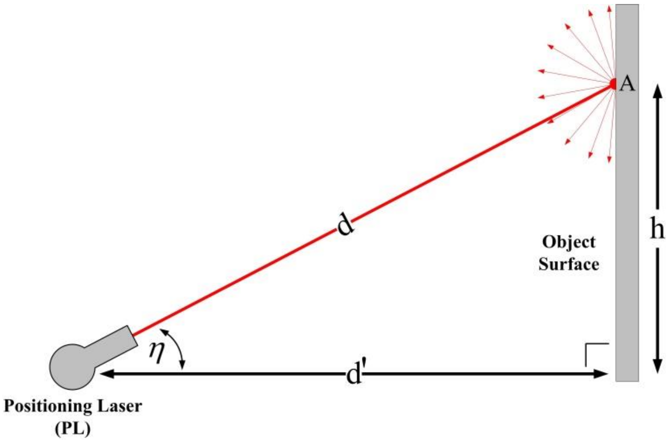

Figure 2-2: Triangle in lateral view

The distance a and the angles β and γ are known and by using the law of sines, the distance d, p and q can be determined: [27]

$$d = a \cdot \frac{\sin\beta \cdot \sin\gamma}{\sin(\beta + \gamma)} \tag{2-1}$$

$$p = \frac{d}{\tan\beta} = a \cdot \frac{\cos\beta \cdot \sin\gamma}{\sin(\beta + \gamma)} \tag{2-2}$$

$$q = \frac{d}{\tan\gamma} = a \cdot \frac{\sin\beta \cdot \cos\gamma}{\sin(\beta + \gamma)} \tag{2-3}$$

By extending the two-dimensional triangle from Figure 2-1 to the three-dimensional space, the third coordinate h can be determined as shown in Figure 2-2. The distance d is already known from (2-1). The angle η is now measured and thus determines the height:

$$h = d \cdot \sin\eta \tag{2-4}$$

Distance d' represents a projection of distance d on the top plane and is defined by:

$$d' = d \cdot \cos\eta \tag{2-5}$$

The point $A(q; d'; h)$ now represents a point in a three-dimensional Cartesian coordinate system.

Laser scanners, which use triangulation, typically consists of a transmitter and receiver unit. Thereby, Figure 2-1 also shows a scheme of laser triangulation, where the transmitter unit is indicated as the positioning laser (PL) and the receiver unit as the scanning aperture (SA). The stricken and reflected laser beam is marked by red color and all measured coordinates by black color.

2.1.2 Static vs. Dynamic Triangulation

The use of the triangulation method in laser scanning systems can be of Static or Dynamic characteristic [27]. Static characteristic is referred to an operation mode without moving the positioning laser or the scanning aperture, which results in a statically behavior of the triangulation. Figure 2-3 shows the basic principle of measurement, which represents the industry standard for contactless distance measurement sensors. A laser beam reflected on a surface is focused on an image sensor (CCD or CMOS sensor) by an optical lens.

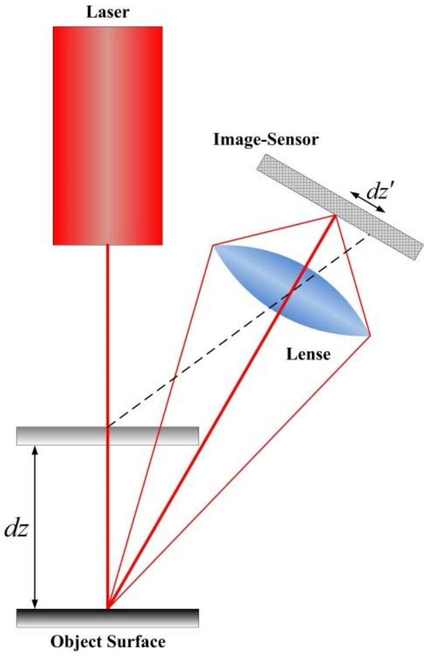

Figure 2-3: Triangulation

A distance change dz of the scanned surface produces a position change dz' of the received laser beam on the image sensor. Because of the static characteristic of this measuring method, the size of the image sensor limits the maximum possible range of the distance measurement. To increase the measuring range of the laser scanner field of view (FOV), the principle of Dynamic Triangulation was developed and which is depicted in Figure 2-4:

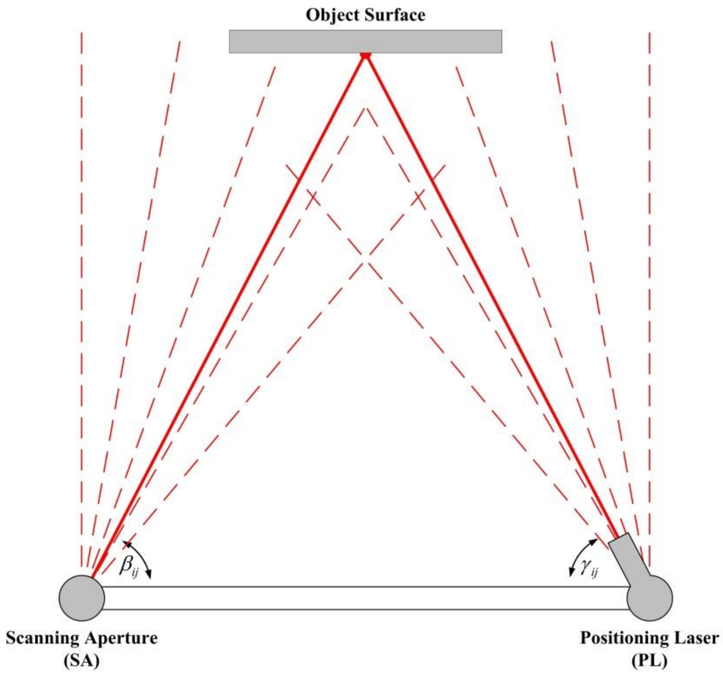

Figure 2-4: Dynamic Triangulation

The dynamic triangulation uses not-fixed transmitter γ_{ij} and receiver angles β_{ij}, to make the measurement range independent of the receiver image sensor size. The transmitter strikes the laser beam under the angle γ_{ij} to the object to be measured, the laser beam gets reflected (total or diffuse) on the object surface and received by the receiver unit under the angle β_{ij}. With the measured angles γ_{ij}, β_{ij} and the equations (2-3), (2-4) and (2-5), the three-dimensional coordinates of the examined object are determined.

2.1.3 Discrete vs. Continuous Field of View

The use of stepping motors for the positioning laser leads to a discrete FOV of the TVS, depicted in Figure 2-5. In the discrete FOV can exist scanning objects, that have dimensions smaller than the resolution of this field and which will not be detected by the TVS. Figure 2-5 also shows, how the resolution of the discrete FOV is increased, the farther is the scanning plane distance and two mutual excluding conditions, when using a discrete FOV: A) Narrow FOV with high resolution or B) Wide FOV with low resolution.

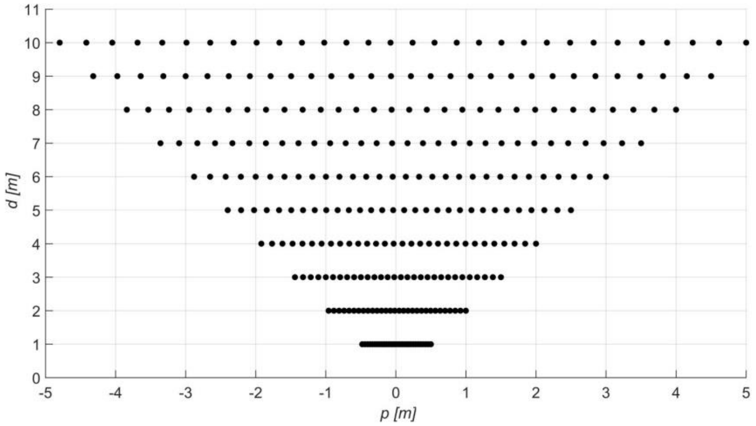

Figure 2-5: Discrete FOV

It must be noted, that by discretization of the scanner FOV, the continuous equations of triangulation get converted to equations using discrete values for the PL and SA angle. Distance a remains a constant value:

$$d_i = a \cdot \frac{\sin \beta_i \cdot \sin \gamma_i}{\sin(\beta_i + \gamma_i)} \tag{2-6}$$

$$q_i = a \cdot \frac{\sin \beta_i \cdot \cos \gamma_i}{\sin(\beta_i + \gamma_i)} \tag{2-7}$$

$$d_i' = d_i \cdot \cos \eta_i \tag{2-8}$$

$$h_i = d_i \cdot \sin \eta_i \tag{2-9}$$

The point $A_i(q_i; d_i'; h_i)$ now represents a discrete point in a three-dimensional Cartesian coordinate system.

Using equation (2-3), the horizontal distance between two adjacent points $A_1(q_1; d_1)$ and $A_2(q_2; d_2)$ can be defined by:

$$\Delta q = q_1 - q_2 \tag{2-10}$$

Supposing a constant distance d for both points, they are distinguished by a different PL angle γ:

$$\Delta q = \frac{d}{\tan \gamma_1} - \frac{d}{\tan \gamma_2} \tag{2-11}$$

Since $\gamma_2 = \gamma_1 + \Delta\gamma$, equation (2-11) can be rewritten:

$$\Delta q = d \cdot \frac{\cos(\gamma_1)}{\sin(\gamma_1)} - d \cdot \frac{\cos(\gamma_1 + \Delta\gamma)}{\sin(\gamma_1 + \Delta\gamma)} \qquad (\text{ 2-12 })$$

Using $\gamma_1 = \gamma$ and the trigonometric sum equations, formula (2-12) can be expressed as:

$$\Delta q = \frac{2d \cdot \sin(\Delta\gamma)}{\cos(\Delta\gamma) - \cos(2\gamma + \Delta\gamma)} \qquad (\text{ 2-13 })$$

Hence, the distance Δq between two adjacent points is a function of the PL angle γ and the PL angle increment $\Delta\gamma$. In the case of $\gamma = \frac{\pi}{2}$, equation (2-13) gets simplified to:

$$\Delta q = d \cdot \tan(\Delta\gamma) \qquad (\text{ 2-14 })$$

Since the $tan(x)$ for the interval $x \epsilon [0, \pi/2]$ represents a monotone increasing function, equation (2-14) shows the resolution decreasing of the discrete FOV, when the PL angle increment $\Delta\gamma$ or the scanning distance d is increasing. Also, equation (2-14) shows the transition from the discrete to a continuous FOV when using $\Delta\gamma = 0$, depicted in Figure 2-6:

$$\Delta q = d \cdot \tan(0) = 0 \qquad (\text{ 2-15 })$$

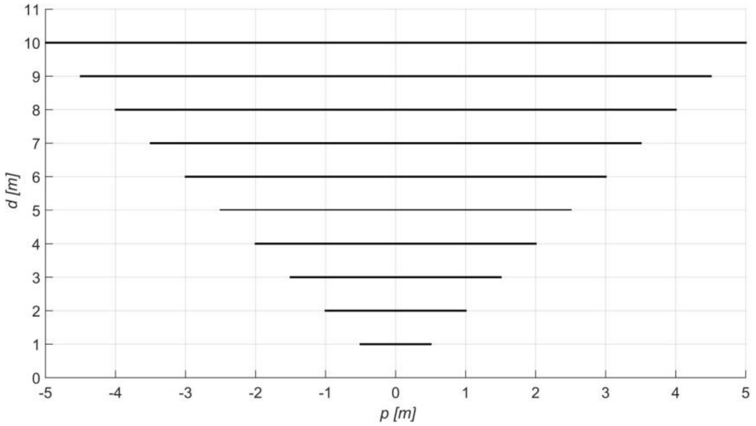

Figure 2-6: Continuous FOV

The continuous FOV, proposed and researched in [35], [37], [47] and [48] originates from the use of DC motors instead of stepping motors for the TVS positioning laser.

2.2 Electromechanical Actuators

Electromechanical actuators are drive elements, which convert electrical signals into mechanical movements or other physical variables. Electromechanical actuators are the counterpart to sensors in measurement and control and represent the active operators in a control system. A main group of electromechanical actuators are represented by electrical motors, of which the Stepping Motor, the DC Motor and the Servomotor are briefly explained in the following.

2.2.1 Stepping Motor

A Stepping Motor is a special type of a synchronous motor (Figure 2-7), with a cogged permanent magnet rotor (1) and particular stator poles (2), whose windings (3) are driven by periodic current pulses [49].

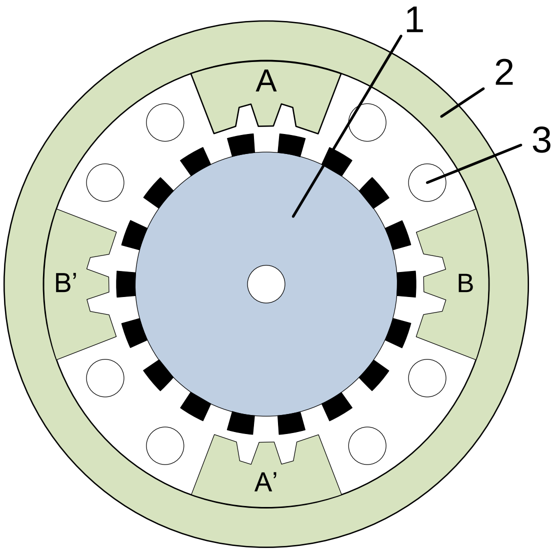

Figure 2-7: Technology schema of a stepping motor

An electronic circuit for stepping motors generates these pulses in the correct order to control the desired speed and direction. One pulse moves the stepping motor in one step-angle, which is a typical parameter of each motor. The pulse sequences generate a rotating magnetic field, which the rotor follows exactly, as long as the load torque is less than the rated torque $M_L < M_M$. Under this condition, the driving of a stepping motor is simpler than that of a servomotor and therefore no sensors for position feedback are required. Because of a discontinuous operation mode, the stepping motor is suitable as a switching mechanism (printer, quartz clock, etc.) and for positioning tasks. At the actual market exists an innumerable amount of different stepping motors, which are characterized by the parameters shown in Table 2-2.

Table 2-2: Typical parameters of stepping motors

Parameter	Symbol	Comment
Step Numbers	n	Usual 24 to 200 steps per revolution
Step Angle	α	Angle for one full step, $\alpha = \frac{360°}{n}$
Maximal Phase Current	$I_{\max}$	Which is allowed through one phase
Phase Resistance	R	Defines the phase current.
Phase Inductance	L	Defines the motor dynamic.
Detent Torque	M_D	Amount of torque necessary to rotate the motor one full step, when it is de-energized.
Holding Torque	M_H	Amount of torque that the motor can apply, within the rated current, without turning the motor shaft.

The stepping motor shaft positioning with 10 steps with $\alpha = 1.8°$ is shown in Figure 2-8, it can be clearly identified the discontinuous behavior:

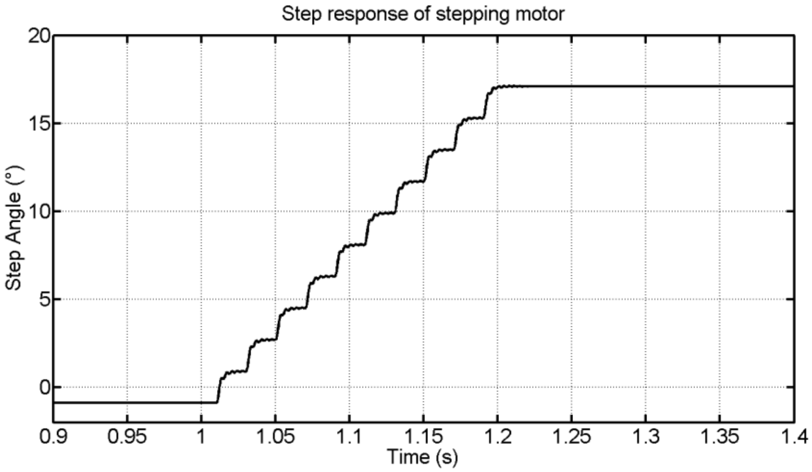

Figure 2-8: Step response of a stepping motor in open-loop control

Table 2-3 summarizes the most important advantages and disadvantages of stepping motors.

Table 2-3: Advantages and disadvantages of stepping motors

Advantages	Disadvantages
No need for position feedback, while $M_L < M_M$.	Stalling of motor, when $M_L > M_M$, loss of steps.
With modern digital electronic, position control is very easy.	Torque drop-off at high speed.
Availability in small sizes and with low cost.	Power consumption at halt.
	Torque control only in closed-loop available.
	Cannot reach any position in his FOM, due to their discontinuous behavior.

2.2.2 DC Motor

A Direct-Current Motor (Figure 2-9) is a machine, which is energized with direct current and mainly consists of the following parts [50]:

1	Main pole	4	Rotor winding (armature)
2	Stator winding	5	Carbon brush
3	Stator (yoke ring)	6	Commutator

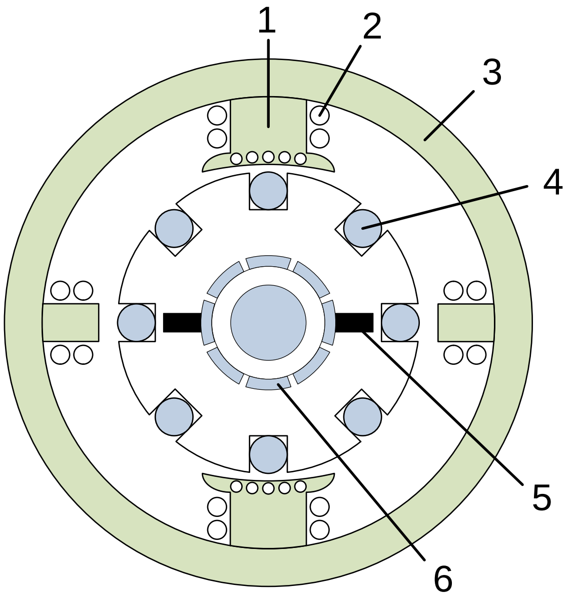

Figure 2-9: Technology scheme of a DC motor

The stator produces the direct magnetic field by the main poles and the stator windings. The stator can be made of permanent magnets in smaller machines (<30 kW). The ends of the main poles are designed to pole shoes. The rotating part of the machine consists of a shaft, which carries the grooved armature. The grooves sustain the rotor windings, which consist of separate individual coils and which are electrically connected to the commutator. When rotating the shaft, the commutator realizes the current reversal in the coils so, that a torque is produced on the shaft in actual rotating direction originated by the Lorentz Force. Current is delivered to the commutator over the carbon brushes, which are usually made of self-lubricating graphite. DC motors can be classified according to the connection between the stator and the rotor windings, summarized in Table 2-4:

Table 2-4: Types of DC motors

Connection Type	Application	Typical drive power
Permanent magnet motor	Battery-powered drives, Computer peripherals, Fine mechanics	$1\ W \ldots 12\ kW$
Series motor	Electric vehicles, Starter motor automobile	$100\ W \ldots 500\ kW$
Shunt motor	Conveying machinery, machine tools	$10\ kW \ldots 10\ MW$

Furthermore, the rotor of the DC motor can use an iron-cored or an ironless winding, as shown in Figure 2-10 and Figure 2-11. The ironless winding was first developed by the company Faulhaber in 1958 and patented in 1965 [51]. Ironless windings have the following advantages compared to conventional iron-cored windings [52]:

- Completely free rotation of rotor, without cogging torque
- High acceleration due to a lower moment of inertia
- Good characteristics at low speed and no iron losses

Figure 2-10: Iron-cored winding

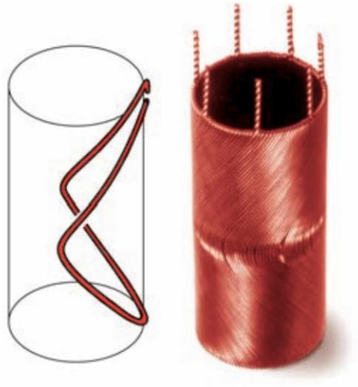

Figure 2-11: Ironless winding

The acceleration of a typical DC motor to $236\,rpm$ is shown in Figure 2-12, it can be clearly identified the continuous behavior.

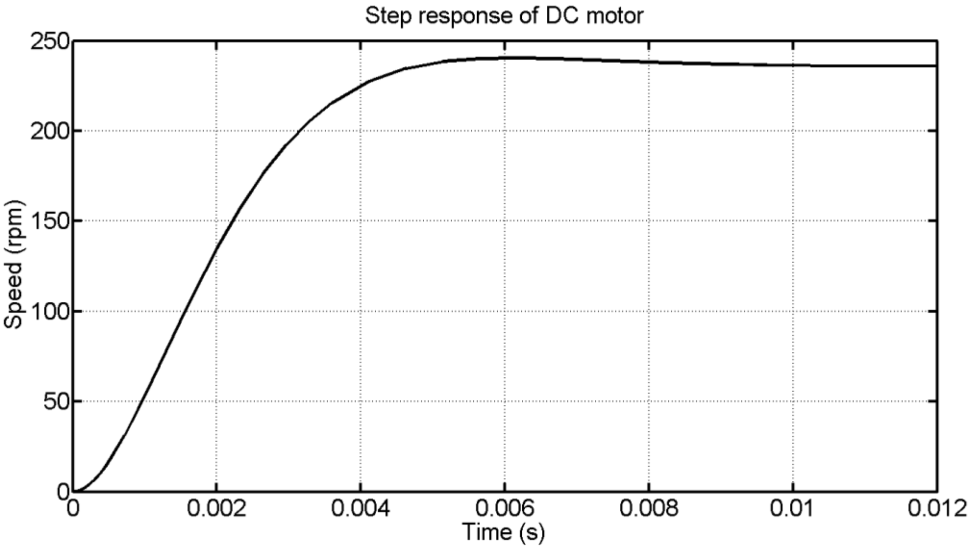

Figure 2-12: Step response of a DC motor in open-loop control

Table 2-5 summarizes the most important advantages and disadvantages of DC motors.

Table 2-5: Advantages and disadvantages of DC motors

Advantages	Disadvantages
Can theoretical reach any position, due to their continuous behavior.	Requires speed / position feedback by encoder for accurate speed / position control.
High output power relative to motor size.	Need for tuning of the closed-loop control.
High torque to inertia ratio.	Closed-loop control more complex.
Can be overloaded in current and torque for short periods.	Friction of the shaft in low cost motors prevents exact positioning.
Resonance and vibration free operation.	Brushes wear out limits life to $2000\ hrs$.

2.2.3 Servomotor

An electrical motor controlled in a closed-loop leads to the Servomotor, which has its original function as an auxiliary drive in the field of machine tools [53]. Like the term servomotor only refers to a Servosystem, where one or several actuators control a motor in a closed-loop, this motor can be any type of. Often are used DC motors in a cascade structure (Figure 2-13):

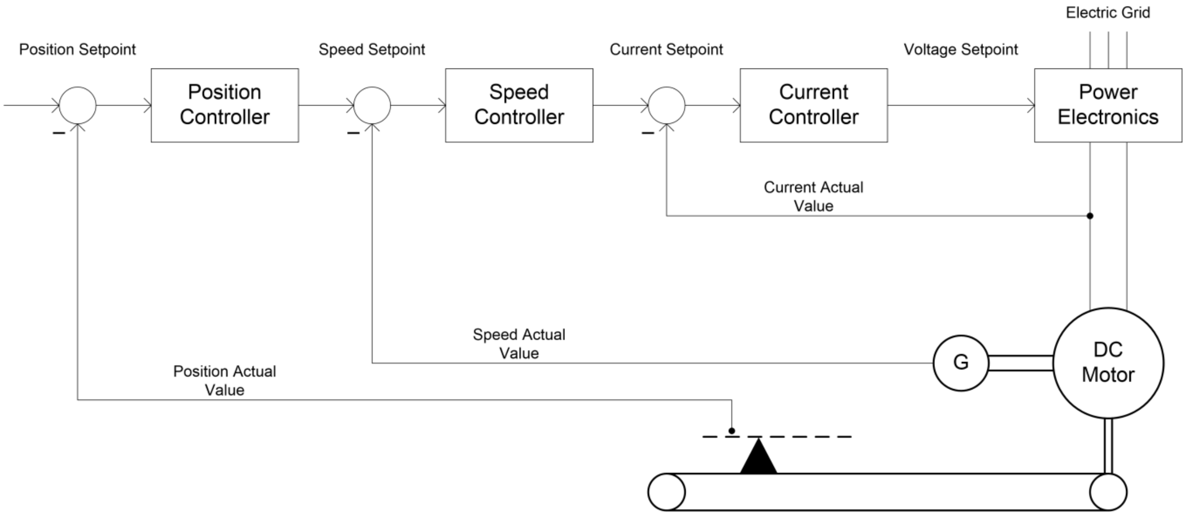

Figure 2-13: Typical cascade control of a servosystem.

Figure 2-13 shows the details of a servosystem in a cascade structure, where G represents the tachogenerator that can be a resolver, an incremental or an absolute encoder. Each higher-level controller calculates the setpoint for the lower-level control loop, which must be faster, than his higher-level control. The current controller determines the voltage setpoint, which is converted to the corresponding armature voltage of the motor terminals via the power electronics. The actual values of position, speed and current are detected by sensors and feed backed to their corresponding control loops.

Modern hobby servos, like the Futaba S3003 (Figure 2-14), are often used as actuators for radio control and small robots. Like stepping motors, they are mass produced and in a large amount of types. The most common type comes in a compact housing with an integrated potentiometer and electronic system to control the angle of the servo in a closed-loop. The potentiometer is connected with the output shaft and gives the actual angle of the servo to the electronic system. This system compares the actual value with the reference value, received from an input Pulse-Width-Modulation signal (PWM). With a difference between actual and reference value, the electronic system corrects the output shaft angle, until the difference turns zero. The PWM-signal is given by the operator and has commonly a frequency of $50Hz$ with a duty cycle between $5 - 10\%$. The electronic system of servos can be analog or digital. Digital servos have a higher angular resolution and the angular position is controlled more quickly and accurately than analog servos. On the other hand they have higher power consumption and are mostly more expensive than analog servos.

Figure 2-14: Hobby servo Futaba S3003

The step response of a typical hobby servo is shown in Figure 2-15. It can be clearly identified the continuous behavior.

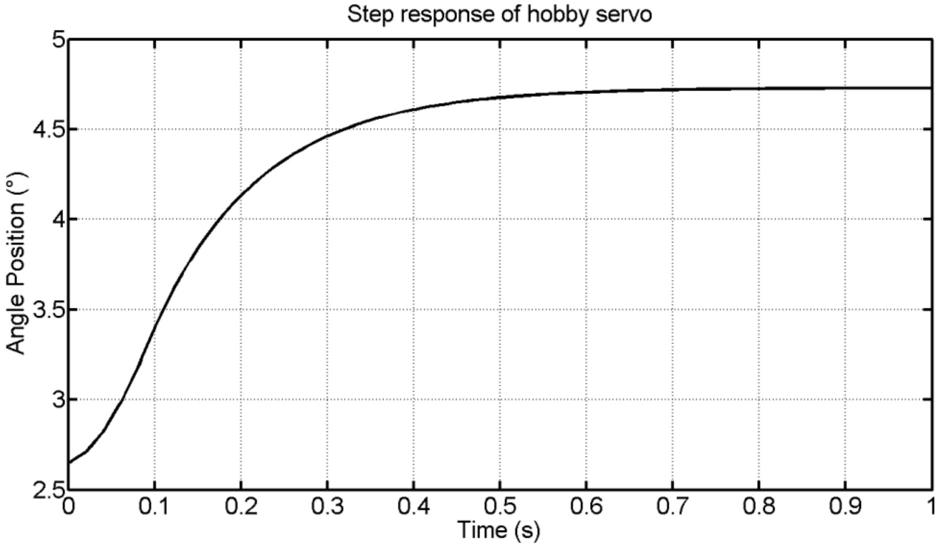

Figure 2-15: Step response of a hobby servomotor

Table 2-6 summarizes the most important advantages and disadvantages of servomotors.

Table 2-6: Advantages and disadvantages of servomotors

Advantages	Disadvantages
Lightweight and compact design.	Require more complex drive circuits and positional feedback for exact positioning.
Maintain their rated torque at high revolutions.	Often comes with gearbox and encoder, which increase the cost and the need of maintenance.

Can supply about twice their rated torque for short period (acceleration).	Resonate backwards and forwards at standstill.
Can theoretical reach any angle in his FOM.	
The positioning exactitude is limited only by the resolution of the encoder.	

Two typically nonlinear effects must be accepted when using low-cost servomotors: the breakaway and the cogging torque. The breakaway torque describes the moment which must be applied by the rotor at standstill, so that it starts to rotate. In Tribology, the breakaway torque is generally referred to as Static Friction, which was described first by the laws of Amonton and Coulomb laws [54]. Static friction is a highly nonlinear effect, which is currently state of the art of modern research and for which exists a lot of complex mathematical models [55]. The cogging torque is caused by the interaction between the permanent magnet of the stator and the coil windings of the rotor. The alignment of the rotor windings to the magnet poles of the stator, resulting in a "snapping" of the stator in only very specific angular positions.

2.3 Programming Environment

Programming environments are required, to implement the theoretically developed algorithms on hardware level. In order to develop the TVS software cost-effective, only open-source and free development environments are considered. Thus, the two main programming environments used for TVS software development are outlined in the following.

2.3.1 Arduino Platform

The Arduino platform describes a family of open-source single-board microcontrollers (Figure 2-16), which since its launch in 2005 has greatly facilitated the development of projects in many areas, not only engineering. The Arduino platform has a modular construction, which allows adding extension shields to expand the functionality and comes with a large software library. Table 2-7 presents the advantages and disadvantages of the Arduino platform.

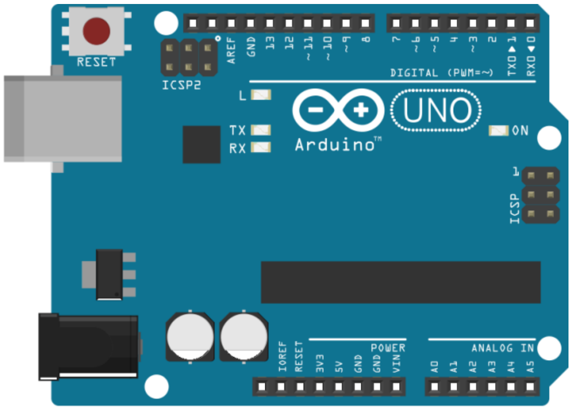

Figure 2-16: Arduino Uno R3

The most basic Arduino Uno has the following main specifications:

- 8-bit AVR RISC-based microcontroller from Atmel with 16 MHz clock speed
- USB Interface for programming and communication with PC
- Integrated timers and counters for time based operations
- Digital inputs / outputs and analog inputs for measuring and sending signals
- Outputs with pulse width modulation (PWM) to control external drivers and loads
- Interrupt inputs to respond to asynchronous external events immediately

Table 2-7: Advantages and disadvantages of the Arduino Platform

Advantages	Disadvantages
Open concept allows extension of Hard- and Software as required by the user.	The code produced by the libraries is slower than C or Assembler code.
No need of an ISP-programmer.	No industrial application, since no certifications are available.
Existence of innumerable Software examples and solutions.	The microcontroller hardware is only understood by programming in basic language.

2.3.2 C# Windows Forms

The programming language C# was developed by Microsoft within its .NET Framework initiative and first released in January 2002. It is the successor of the languages C / C++ and a multi-paradigm programming language for different operating systems like Windows, Mac OS X or UNIX. C# on Windows systems can be developed with the free Microsoft Visual C# Express integrated development environment. Furthermore, Windows Forms represents a programming tool to build graphical user interfaces (Figure 2-17) and is included in the Microsoft .NET-Framework.

It is used to communicate between user and the physical platform Arduino Uno. The user can send reference variables and commands to the Arduino and receive actual and status variables from it.

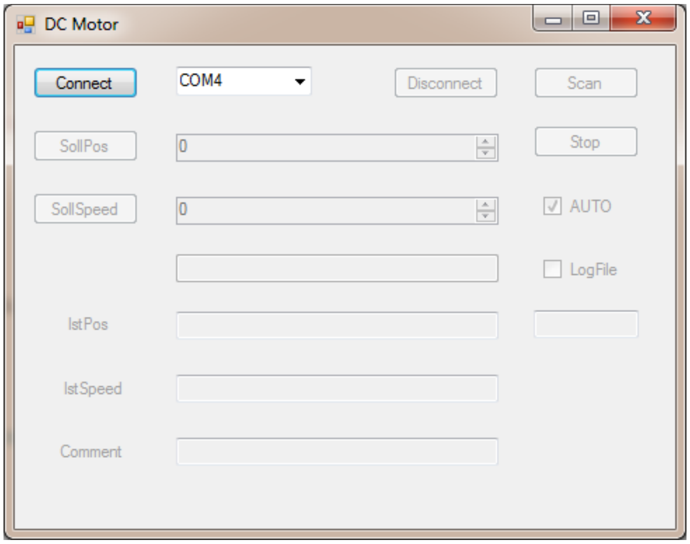

COM4

SollPos 0

SollSpeed 0

☑ AUTO

☐ LogFile

Figure 2-17: GUI for DC motor written in Microsoft Visual C#

3 Theoretical Concepts

The newly presented scanning principle shall use servomotors instead of stepping motors, to substitute the discrete laser scanner FOV by a continuous one. Present chapter provides fundamental theoretical concepts, which are required for modeling and stability analysis of the used servomotors in the next chapter 4. There, the modeling of the servomotors position and speed control is defined in detail. For stability analysis of these two control tasks, present chapter outlines the mathematical deduction of the Routh Criterion and the Routh Algorithm, which determines the denominator zeros of a linear transfer function (TF) $G(s) = \frac{N(s)}{D(s)}$ in the complex plane. This mathematical deduction requires the determination of the number of real zeros of a real polynomial $f(x)$ in a given interval $[a, b]$, which is explained by Sturm’s Theorem. Furthermore, a brief introduction about Fourier series and the Fourier transformation is given, which also will be required for following chapter 4 to describe mathematically digital square wave signals. More detailed information on the presented theoretical concepts can be found in a relevant literature about classical control theory [56], [57].

3.1 Sturm’s Theorem

Jacques Charles François Sturm published 1829 the Sturm's Theorem, which represents a mathematical method to determine the number of real zeros of a polynomial $f(x)$ with degree n in a given interval $[a, b]$. To form a Polynomial Chain, the following two initial polynomials are defined:

$$\begin{aligned} P_0(x) &= f(x) \\ P_1(x) &= f'(x) \end{aligned} \tag{3-1}$$

The following polynomials P_{k+2} with $k = 0,1, \dots, n$ of the chain are determined by using the Euclidean Algorithm for Polynomials (polynomial long division):

$$\begin{aligned} P_0 &= Q_1 \cdot P_1 - P_2 \\ P_1 &= Q_2 \cdot P_2 - P_3 \\ P_k &= Q_{k+1} \cdot P_{k+1} - P_{k+2} \\ P_n &= C \neq 0 \end{aligned} \tag{3-2}$$

By applying the Euclidean Algorithm, the degree of the polynomials P_k is decreasing monotonically. The polynomials P_{k+2} are formed by the remainder of the polynomial long division and the chain is continued until the last polynomial P_n arises as a constant not zero. By evaluating the polynomials $P_o, P_1, \dots, P_n$ at both boundaries of the given interval $[a, b]$ and counting the sign changes of the calculated values, the Number of Sign Changes $V(\tilde{x})$ for each boundary is determined. The number of sign changes $V(a)$ and $V(b)$ is used by Sturm's Theorem:

Theorem 1:

Be $f(x)$ a real polynomial with only simple zeros. The number of real zeros in the interval $[a, b]$ is equal to the difference $V(a) - V(b)$ [56].

Example 1:

It shall be determined the number of zeros of $f(x) = x^3 - 6x^2 + 11x - 6$ in the interval $[0,4]$. First are defined $P_0 = f(x) = x^3 - 6x^2 + 11x - 6$ and $P_1 = f'(x) = 3x^2 - 12x + 11$. Then it is formed the corresponding polynomial chain:

$$P_0 = \frac{1}{3}[(x-2)(3x^2 - 12x + 11) - (2x - 4)] = Q_1 \cdot P_1 - P_2$$

$$P_1 = \left(\frac{3}{2} \cdot x - 3\right)(2x - 4) - 1 = Q_2 \cdot P_2 - P_3$$

$P_3 = 1$ represents a constant, the polynomial chain finishes here. Now the signs of these polynomials are evaluated at the interval boundaries:

	P_0	P_1	P_2	P_3	$V(\tilde{x})$
$a = 0$	$-$	$+$	$-$	$+$	3
$b = 4$	$+$	$+$	$+$	$+$	0

The difference $V(a) - V(b) = 3$, indeed $f(x) = x^3 - 6x^2 + 11x - 6 = (x-1)(x-2)(x-3)$ has 3 real zeros.

3.2 Routh Criterion and Algorithm

The stability of a linear transfer element $G(s) = \frac{N(s)}{D(s)}$ can be determined by the zeros of the denominator polynomial, also called characteristic polynomial:

$$D(s) = 0 \tag{3-3}$$

As widely known from linear control theory [56], this transfer element is stable, if all zeros of the characteristic polynomial have a negative real part. Since the characteristic polynomial usually is of higher degree, the analytic determination of the zeros turns out to be a complex task. As a result of the Galois Theory, it has been shown that for polynomials of fifth degree or more, no analytical solution for determination of the zeros is present. However, for determination of the transfer element stability, only the real part signs of the denominator zeros are essential. The Routh Criterion gives a conclusion about the location of polynomials zeros in the complex plane without explicit solving the polynomials. The Routh Criterion represents an algebraic criterion, which uses only the denominator polynomial coefficients for the Routh Algorithm. The Routh Algorithm gives a practical and simple way to determine the number of zeros with positive real part of the characteristic polynomial $D(s)$. Both the Routh Criterion and Algorithm were presented in 1877 by Edward John Routh with his article “Treatise on the Stability of a Given State of Motion”.

3.2.1 Routh Criterion

Be $f(s) = a_n s^n + a_{n-1} s^{n-1} + \cdots + a_1 s + a_0$ an arbitrary polynomial of the complex variable $s = \sigma + j\omega$, with real coefficients and degree n, which has k zeros with positive real part. Using the Fundamental Theorem of Algebra, this polynomial can be converted into its linear factors form:

$$f(s) = a_n \prod_{i=1}^{n} (s - s_i) \tag{3-4}$$

and exponential form:

$$f(s) = |f(s)| \cdot \exp\left(j \cdot \sum_{i=1}^{n} \operatorname{arc}(s - s_i) \right) \tag{3-5}$$

, whereat:

$$\operatorname{arc}(f(s)) = j \cdot \sum_{i=1}^{n} \operatorname{arc}(s - s_i) \tag{3-6}$$

Equation (3-5) can be proofed using the well-known equation for multiplying two complex numbers z_1 and z_2 in their exponential form:

$$z_1 z_2 = |z_1||z_2| \exp\big(j(\operatorname{arc} z_1 + \operatorname{arc} z_2)\big) \tag{3-7}$$

By integrating the polynomial $f(s)$ along the imaginary axis $s = j\omega$, the following relationship for the increment of the polynomial argument $d \operatorname{arc} f(s)$ can be derived [56]:

$$\begin{aligned}\int_{s=-j\infty}^{j\infty} d \operatorname{arc} f(s) = \int_{\omega=-\infty}^{\infty} d \operatorname{arc} f(j\omega) = \sum_{i=1}^{n} \int_{\omega=-\infty}^{\infty} d \operatorname{arc}(j\omega - s_i) \\ = \pi\big((n-k) - k\big) = \pi(n - 2k)\end{aligned} \tag{3-8}$$

Equation (3-8) shows, that the increment of the polynomial argument depends only from the difference between the zeros with negative and the zeros with positive real part. Zeros with negative real part add $+\pi$ and zeros with positive real part add $-\pi$ to the increment of the polynomial argument $d \operatorname{arc} f(s)$. Routh separated the polynomial along the imaginary axis $f(j\omega)$ in a real and imaginary part [56]:

$$\begin{aligned} f(j\omega) &= a_n(j\omega)^n + a_{n-1}(j\omega)^{n-1} + \cdots + a_1(j\omega) + a_0 \\ &= j^n(a_n\omega^n - a_{n-2}\omega^{n-2} + a_{n-4}\omega^{n-4} - \cdots) \\ &\qquad - j^{n+1}(a_{n-1}\omega^{n-1} - a_{n-3}\omega^{n-3} + a_{n-5}\omega^{n-5} - \cdots) \\ &= j^n f_1(\omega) - j^{n+1} f_2(\omega) \\ &= j^n[f_1(\omega) - j f_2(\omega)] \end{aligned} \tag{3-9}$$

With this decomposition, the integral of (3-8) can be simplified as follows [56]:

$$\begin{aligned}\pi(n-2k) &= \int_{\omega=-\infty}^{\infty} d\,\mathrm{arc}\, f(j\omega) \\ &= \int_{\omega=-\infty}^{\infty} d\,\mathrm{arc}\big(f_1(\omega) - jf_2(\omega)\big) \\ &= -\int_{\omega=-\infty}^{\infty} d\ \arctan\frac{f_2(\omega)}{f_1(\omega)} \\ &= \lim_{\omega\to-\infty} \arctan\left(\frac{f_2(\omega)}{f_1(\omega)}\right) - \lim_{\omega\to\infty} \arctan\left(\frac{f_2(\omega)}{f_1(\omega)}\right) \qquad (3\text{-}10)\end{aligned}$$

Thus, through evaluation of integral (3-10), the number of zeros with positive real part k can be concluded. It must be noted, that the function $\frac{f_2(\omega)}{f_1(\omega)}$ represents a strictly proper function, due to $\deg f_1(\omega) > \deg f_2(\omega)$. It can be formed a polynomial chain for the function $\frac{f_2(\omega)}{f_1(\omega)}$, using the polynomial long division. For this division to be applied, $f_1(\omega)$ must represent the dividend and $f_2(\omega)$ the divisor:

$$\begin{aligned} f_1(\omega) &= q_1(\omega)\cdot f_2(\omega) - f_3(\omega) \\ f_2(\omega) &= q_2(\omega)\cdot f_3(\omega) - f_4(\omega) \\ f_3(\omega) &= q_3(\omega)\cdot f_4(\omega) - f_5(\omega) \\ &\vdots \\ f_{n+1}(\omega) &= C \neq 0 \qquad (3\text{-}11)\end{aligned}$$

Example 2:

It shall be analyzed the following polynomial $f(s) = s^3 + s^2 + 4s + 16$. First, this polynomial shall be separated in real and imaginary part for $s = j\omega$ using equation (3-9):

$$\begin{aligned} f(j\omega) &= (j\omega)^3 + (j\omega)^2 + 4(j\omega) + 16 \\ &= j^3(\omega^3 - 4\omega) - j^4(\omega^2 - 16) \\ &= j^3[(\omega^3 - 4\omega) - j(\omega^2 - 16)]\end{aligned}$$

Hence, $f_1(\omega) = \omega^3 - 4\omega$ and $f_2(\omega) = \omega^2 - 16$. Then it is formed the corresponding polynomial chain for the strictly proper function $\frac{f_2(\omega)}{f_1(\omega)}$:

$$\begin{aligned} f_1(\omega) &= \omega(\omega^2 - 16) - (-12\omega) = q_1(\omega)f_2(\omega) - f_3(\omega) \\ f_2(\omega) &= -\frac{1}{12}\omega(-12\omega) - 16 = q_2(\omega)f_3(\omega) - f_4(\omega)\end{aligned}$$

$f_4(\omega) = 16$ represents a constant, the polynomial chain finishes here. Now the signs of these polynomials are evaluated for certain values $\tilde{\omega} \in \mathbb{R}$ and neighborhood $\varepsilon \ll \tilde{\omega}$:

$\tilde{\omega}$	$f_1(\omega)$	$f_2(\omega)$	$f_3(\omega)$	$f_4(\omega)$	$V(\tilde{\omega})$
$-2-\varepsilon$	-	-	+	+	1
-2	0	-	+	+	
$-2+\varepsilon$	+	-	+	+	2
$0-\varepsilon$	+	-	+	+	2
0	0	-	0	+	
$0+\varepsilon$	-	-	-	+	1
$2-\varepsilon$	-	-	-	+	1
2	0	-	-	+	
$2+\varepsilon$	+	-	-	+	2

It must be noted, that the function $\frac{f_2(\omega)}{f_1(\omega)}$ has discontinuities where $f_1(\tilde{\omega}) = 0$, which can change from $"-\infty"$ to $"+\infty"$ (positive change) or from $"+\infty"$ to $"-\infty"$ (negative change). The number of sign changes $V(\tilde{\omega})$ can only be increased or decreased at these discontinuities. The product of the signs of the two functions $f_1(\omega)$ and $f_2(\omega)$ before $(\tilde{\omega} - \varepsilon)$ and after the discontinuity $(\tilde{\omega} + \varepsilon)$ determines the sign change direction. When the discontinuity represents a negative change, then $V(\tilde{\omega})$ is increased and counting the number of changes gives $V_{-\infty}$. When the discontinuity represents a positive change, then $V(\tilde{\omega})$ is decreased and counting the number of changes gives $V_{+\infty}$. For the current example $V(\tilde{\omega})$ is increased twice, hence $V_{-\infty} = 2$ and $V(\tilde{\omega})$ is decreased once, hence $V_{+\infty} = 1$.

The value $(n - 2k)$ can also be determined by the difference of $V_{+\infty}$ and $V_{-\infty}$, which can also be found as the Cauchy Index [58]:

$$V_{+\infty} - V_{-\infty} = n - 2k \qquad (3\text{-}12)$$

Since the degree of $f_1(\omega)$ is equal to $f(j\omega)$, the sum of the positive $V_{+\infty}$ and negative changes $V_{-\infty}$ gives:

$$V_{+\infty} + V_{-\infty} = n \qquad (3\text{-}13)$$

Equation (3-12) now can be solved for k and using current example, gives:

$$k = \frac{n - (V_{+\infty} - V_{-\infty})}{2} = \frac{3 - (-1)}{2} = 2 \qquad (\,3\text{-}14\,)$$

Hence, the polynomial $f(s) = s^3 + s^2 + 4s + 16$ has two zeros with positive and one zero with negative real part. Indeed, the zeros are $s_1 = 0.6475 + 2.5598j$, $s_2 = 0.6475 - 2.5598j$ and $s_3 = -2.2949$.

3.2.2 Routh Algorithm

To derive the Routh Algorithm, the polynomial chain for $f_1(\omega)$ and $f_2(\omega)$ shall be formed. First, equation (3-9) defines $f_1(\omega)$ and $f_2(\omega)$:

$$\begin{aligned} f_1(\omega) &= a_n\omega^n - a_{n-2}\omega^{n-2} + a_{n-4}\omega^{n-4} - \cdots \\ f_2(\omega) &= a_{n-1}\omega^{n-1} - a_{n-3}\omega^{n-3} + a_{n-5}\omega^{n-5} - \cdots \end{aligned}$$

Second, the polynomial long division for $\frac{f_1(\omega)}{f_2(\omega)}$ is applied:

$$\begin{array}{|l l l l|} \hline \qquad\qquad f_1(\omega) & \div & f_2(\omega) = & \dfrac{a_n}{a_{n-1}}\omega \ldots \\ \quad -\left(a_n\omega^n + \dfrac{a_n a_{n-3}}{a_{n-1}}\omega^{n-2} - \dfrac{a_n a_{n-5}}{a_{n-1}}\omega^{n-4} - \cdots\right) & & & \\ \cline{1-1} = -\left(a_{n-2} - \dfrac{a_n a_{n-3}}{a_{n-1}}\right)\omega^{n-2} + \left(a_{n-4} - \dfrac{a_n a_{n-5}}{a_{n-1}}\right)\omega^{n-4} - \cdots & & & \\ = -f_3(\omega) & & & \\ \hline \end{array}$$

The polynomial long division results:

$$\frac{f_1}{f_2} = \frac{a_n}{a_{n-1}}\omega - \frac{f_3}{f_2}$$

Solving for $f_3(\omega)$ gives:

$$f_3(\omega) = \frac{a_n}{a_{n-1}}\omega \cdot f_2(\omega) - f_1(\omega)$$

$$
\begin{aligned}
&= \left(a_{n-2} - \frac{a_n a_{n-3}}{a_{n-1}}\right)\omega^{n-2} - \left(a_{n-4} - \frac{a_n a_{n-5}}{a_{n-1}}\right)\omega^{n-4} + \cdots \\
&= b_{n-2}\omega^{n-2} - b_{n-4}\omega^{n-4} + \cdots
\end{aligned}
$$

The polynomial long division will be repeated now for $f_2(\omega)$ and $f_3(\omega)$. Like division $\frac{f_2(\omega)}{f_3(\omega)}$ represents the same division like $\frac{f_1(\omega)}{f_2(\omega)}$ reduced by one degree for power and indices, it can directly be concluded for the polynomial division:

$$\frac{f_2}{f_3} = \frac{a_{n-1}}{b_{n-2}}\omega - \frac{f_4}{f_3}$$

Solving for $f_4(\omega)$ gives:

$$
\begin{aligned}
f_4(\omega) &= \frac{a_{n-1}}{b_{n-2}}\omega \cdot f_3(\omega) - f_2(\omega) \\
&= \left(a_{n-3} - \frac{a_{n-1} b_{n-4}}{b_{n-2}}\right)\omega^{n-3} - \left(a_{n-5} - \frac{a_{n-1} b_{n-6}}{b_{n-2}}\right)\omega^{n-5} + \cdots \\
&= c_{n-3}\omega^{n-3} - c_{n-5}\omega^{n-5} + \cdots
\end{aligned}
$$

Continuing the polynomial chain until:

$$f_{n+1} = a_0$$

In summary, the Routh Calculation Scheme can be presented, which is widely found in most literature of linear control theory [56], [57]:

$$
\begin{array}{c|ccccc}
\omega^{n}: & a_n & a_{n-2} & a_{n-4} & a_{n-6} & \cdots \\
\omega^{n-1}: & a_{n-1} & a_{n-3} & a_{n-5} & \cdots & \\
\hline
\omega^{n-2}: & b_{n-2} & b_{n-4} & b_{n-6} & \cdots & \\
\omega^{n-3}: & c_{n-3} & c_{n-5} & \cdots & & \\
\omega^{n-4}: & d_{n-4} & d_{n-6} & \cdots & & \\
\omega^{n-5}: & e_{n-5} & \cdots & & & \\
\vdots & \vdots & & & & \\
\omega^{0}: & a_0 & & & &
\end{array}
$$

The first two rows are the coefficients of the polynomial to be examined $f(s)$. From the third row, the coefficients are calculated recursively using the following equations:

$$\begin{aligned}
b_{n-k} &= a_{n-k} - \frac{a_n}{a_{n-1}} a_{n-(k+1)} \\
c_{n-k} &= a_{n-k} - \frac{a_{n-1}}{b_{n-2}} b_{n-(k+1)} \\
d_{n-k} &= b_{n-k} - \frac{b_{n-2}}{c_{n-3}} c_{n-(k+1)} \\
e_{n-k} &= c_{n-k} - \frac{c_{n-3}}{d_{n-4}} d_{n-(k+1)}
\end{aligned}$$

Example 3:

Using example 2, it is formed the Routh Calculation Scheme for the polynomial $f(s) = s^3 + s^2 + 4s + 16$:

ω^3:	1	4
ω^2:	1	16
ω^1:	-12	0
ω^0:	16	

The calculated values are also the coefficients of the polynomial chain according to Sturm´s Theorem. Subtracting equation (3-13) from (3-12) results:

$$V_{-\infty} = k \qquad (3\text{-}15)$$

That is, the zeros with positive real part arises solely from the number of negative changes $V_{-\infty}$ of the sign changes $V(\widetilde{\omega})$ at discontinuities of the division $\frac{f_2(\omega)}{f_1(\omega)}$. It can be shown, that the number of changes $V_{-\infty}$ results from the sign changes of the first column coefficients in the Routh Calculation Scheme [56]:

$$V_{-\infty} = V(a_n, a_{n-1}, b_{n-2}, c_{n-3}, d_{n-4}, \cdots) \qquad (3\text{-}16)$$

Thereby, the number of zeros k with positive real part can be concluded by the number of sign changes $V_{-\infty}$ in the first column of the Routh Calculation Scheme. The case $k = 0$ represents the Routh Criterion for stability of a linear transfer element $G(s) = \frac{N(s)}{D(s)}$:

Theorem 2:

A linear transfer element $G(s) = \frac{N(s)}{D(s)}$ is stable, if after application of the Routh Calculation Scheme for the denominator polynomial D (s), all the coefficients of the first column have the same sign.

Finally, it shall be mentioned a sign condition for the coefficients of the denominator polynomial $D(s)$, which is often referred to as Stodola-Condition [56]:

Theorem 3:

A linear transfer element $G(s) = \frac{N(s)}{D(s)}$ is unstable, if the denominator polynomial $D(s)$ has one coefficient with different sign or a vanishing coefficient.

3.3 Fourier Series

Form calculus it is known, that every piecewise continuous and periodic function $f(t)$ with period $T = \frac{2\pi}{\omega}$ can be decomposed into harmonic functions (Fourier Analysis) or be composed from it (Fourier Synthesis) using:

$$f(t) = \frac{a_0}{2} + \sum_{n=1}^{\infty}(a_n \cos(n\omega t) + b_n \sin(n\omega t)) \tag{3-17}$$

By summation of infinite elements of sine and cosine functions, the Fourier Series converges for all t to the periodic function $f(t)$. Equation (3-17) describes the discrete frequency spectrum of the periodic function $f(t)$. The DC part $\frac{a_0}{2}$ represents the mean value over one function period:

$$a_0 = \frac{2}{T}\int_0^T f(t)\,dt \tag{3-18}$$

For $n = 1,2,3, \ldots$, the coefficients a_n and b_n represents the amplitudes of the n-th Harmonic f_n and are defined by:

$$a_n = \frac{2}{T}\int_0^T f(t)\cos(n\omega t)\,dt \tag{3-19}$$

$$b_n = \frac{2}{T}\int_0^T f(t)\sin(n\omega t)\,dt \tag{3-20}$$

These amplitudes of the harmonics decrease with increasing frequency, so that the Fourier series converges to $f(t)$. In practical applications, it is usually sufficient to consider only a finite number of harmonics (partial sum). For signals with a low slew rate (for example a triangular wave), the Fourier series converges faster than for signals with a large slew rate. For commonly used periodic functions exist correspondence tables with computed coefficients.

3.4 Fourier Transformation

The transition from the Fourier series to the Fourier Transformation is used to describe non-periodic and double-sided limited signals. By forming the limit value $T \to \infty$ of the periodic time function $f(t)$ and assuming, that $f(t)$ is absolutely integrable:

$$\int_{-\infty}^{\infty} |f(t)|\,dt < \infty \tag{3-21}$$

, the Fourier transformation of $f(t)$ is specified by following definition:

$$F(j\omega) = \int_{-\infty}^{\infty} f(t)e^{-j\omega t}\,dt \tag{3-22}$$

The Fourier transformation is used to convert a time function $f(t)$ into her continuous frequency spectrum $F(j\omega)$ defined in the complex frequency domain $j\omega$. The Inverse Fourier Transformation allows the conversion of the frequency function $F(j\omega)$ into the time domain:

$$f(t) = \frac{1}{2\pi}\int_{-\infty}^{\infty} F(j\omega)e^{j\omega t}\,d\omega \tag{3-23}$$

Correspondence tables exist for commonly used time functions.

4 DC Motor Continuous Model

DC motors used as servomotors shall be used for the new TVS prototype No.3. To analyze the stability of the closed-loop position and speed control and to optimize the controller parameters, present chapter will define a continuous and linear model for DC motor position and speed control and derive the step response for both control loops, using the Routh Criterion and Routh Algorithm, defined in previous chapter. The linear models of position and speed control are expressed as transfer functions in the frequency domain. Furthermore, the frequency response of the DC motor transfer function and of the DC motor output signal shall be derived, in order to compare the lowest cutoff frequency of both frequency responses. Thereby shall be proved that, due to the second-order low-pass filter behavior, the DC motor filters all harmonics of the PWM signal of the armature voltage $u_A(t)$. Present chapter describes the general transfer function of a DC motor, in detail the continuous model for position and speed control and the frequency response of the DC motor and DC motor output.

4.1 Transfer Function

In the following, a model for the electrical and mechanical part of a DC motor used as servomotor (Figure 2-13) is derived. For the sake of simplicity, the cascade structure of the servomotor is replaced by single-loops for position and speed control. Figure 4-1 shows the equivalent circuit diagram for a DC motor with permanent magnets, which can be found in most literature [49], [59], [60], [61] and [62], under neglecting nonlinear effects, such as breakaway and cogging torque and neglecting the back electromotive force (back-emf). Thereby $u_A(t)$ represents the DC motor armature input voltage, $i_A(t)$ the armature current, L_A the armature inductance, R_A the armature resistance, $\omega_o(t)$ the actual angular speed and $M(t)$ the produced motor torque. It represents the electrical part of the DC motor.

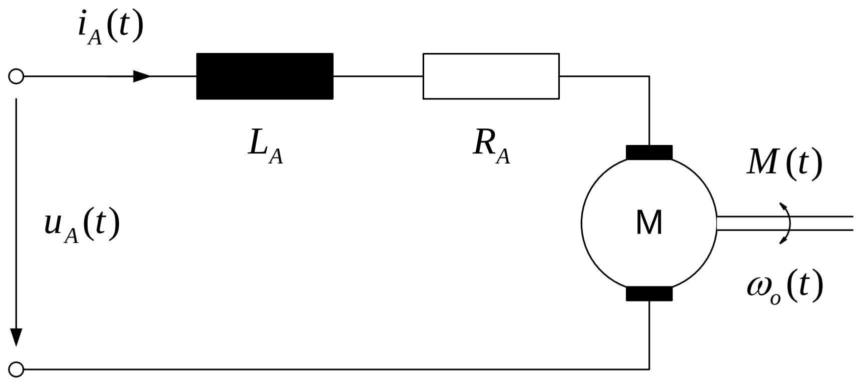

Figure 4-1: Equivalent circuit of a DC motor

Applying the Kirchhoff law for meshes and transforming the differential equation into the frequency domain by Laplace-Transformation with initial values zero, it can be derived the transfer functions $G(s)$ of the linear transfer elements:

1. Because of the delayed magnetization of the rotor windings, a first-order delay element describes the behavior of the motor current $i_A(t)$, when applied the armature input voltage $u_A(t)$:

$$G_E(s) = \frac{I_A(s)}{U_A(s)} = \frac{1}{R_A + s \cdot L_A} = \frac{K_E}{1 + s \cdot T_E}$$

, with $K_E = \frac{1}{R_A}$ the armature gain and $T_E = \frac{L_A}{R_A}$ the electrical time constant.

2. A proportional element describes the relation between motor current and motor torque:

$$G_T(s) = \frac{M(s)}{I_A(s)} = K_T$$

The linear behavior between the armature input voltage of the DC motor and the produced motor torque is now described by a chain structure:

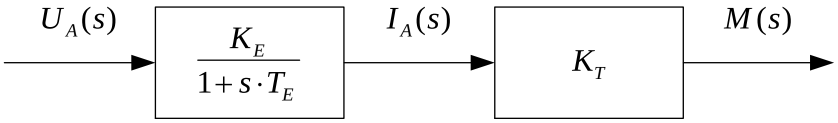

Figure 4-2: Chain structure of the electrical part of a DC motor

The mechanical part of the DC motor describes the following torque equation:

$$J \cdot \frac{d\omega_o(t)}{dt} = M(t) - M_f(t) \tag{4-1}$$

Thereby J represents the total moment of inertia, $\omega_o(t)$ the actual angular speed and $M_f(t)$ the friction torque. Because for relatively small velocities, the friction torque depends linear on the actual angular speed $M_f = r \cdot \omega_o$ with damping r, this torque equation can be rewritten as:

$$M(t) = J \cdot \dot{\omega}_o + r \cdot \omega_o \tag{4-2}$$

and then be transformed into the frequency domain:

$$G_M(s) = \frac{\Omega_o(s)}{M(s)} = \frac{1}{r + s \cdot J} = \frac{1/r}{1 + s \cdot T_M} \tag{4-3}$$

, with $T_M = \frac{J}{r}$ the mechanical time constant. Now with the torque equation (4-3), the chain structure of the electrical part shown in Figure 4-2 will be extended to the complete chain structure of the DC motor:

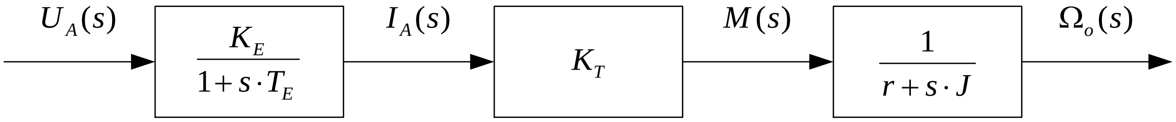

Figure 4-3: Controlled system

, and the complete system transfer function of the DC motor is represented by:

$$G_S(s) = \frac{\Omega_o(s)}{U_A(s)} = \frac{K_E K_T}{(1 + s \cdot T_E)(r + s \cdot J)} = \frac{K_E K_T r^{-1}}{(1 + sT_E)(1 + sT_M)} \tag{4-4}$$

4.2 Position Control

4.2.1 Closed-Loop Model

To optimize the position-control of the servomotor, the DC motor (Figure 4-3) shall be controlled in a closed-loop using a P-controller, shown in Figure 4-4:

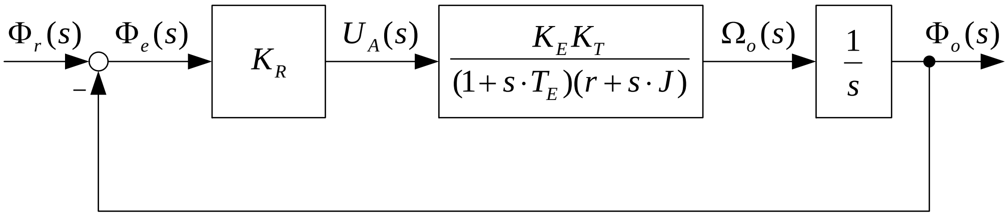

Figure 4-4: Closed-loop position control model of a DC motor

It must be noted, that for position control of the DC motor, an integral part of the controller would be useless, since this would generate an armature voltage U_A in the case of an angular position error zero $\Phi_e = 0$ and thereby the motor would not stop at the reference angular position Φ_r. The actual angular position Φ_o results by integrating the actual angular speed Ω_0. This actual angular gets rested from the reference angular position Φ_r and results in the angular position error Φ_e:

$$\Phi_e = \Phi_r - \Phi_o \tag{4-5}$$

The gain of the P-controller is the amplification factor of positioning algorithm K_R. The open-loop transfer function of this control loop is defined by the product of the controller TF with the controlled system TF:

$$G_O(s) = G_R(s) \cdot G_S(s) = \frac{K_R K_E K_T}{s(1 + s \cdot T_E)(r + s \cdot J)} \tag{4-6}$$

The closed-loop TF of the position control then can be calculated using $G(s) = \frac{G_O}{1+G_O}$:

$$G(s) = \frac{K_R K_E K_T}{K_R K_E K_T + sr + s^2(J + rT_E) + s^3 T_E J} = \frac{N(s)}{D(s)} \tag{4-7}$$

4.2.2 Stability

It shall be analyzed the stability of the given closed-loop speed control model (Figure 4-4) and transfer function $G(s)$ (4-7), depending on the controller parameter K_R. As described in section 3.2, all zeros of the denominator polynomial:

$$D(s) = K_R K_E K_T + sr + s^2(J + rT_E) + s^3 T_E J = 0 \tag{4-8}$$

must have a negative real part. Using the Routh Algorithm and the Routh Criterion, the stability of the transfer function $G(s)$ shall be determined. The Routh Algorithm gets applied for the denominator polynomial:

Table 4-1: Routh Algorithm for D(s)

	$T_E J$	r
	$J + rT_E$	$K_R K_E K_T$
I:	$r(J + rT_E) - K_R K_E K_T T_E J = f(K_R)$	
II:	$K_R K_E K_T \cdot f(K_R)$	

According to the Routh Criterion, all expressions in the first column must have the same sign, so that the analyzed transfer function $G(s)$ is stable. As it can be observed from the first two lines, since the controller parameter K_R is positive and real, that all expressions must also be positive. This condition can be used, to determine a condition for K_R. The function obtained in line I must be positive too:

$$r(J + rT_E) - K_R K_E K_T T_E J > 0 \tag{4-9}$$

Solving equation (4-9) for K_R results in:

$$K_R < \frac{r(J + rT_E)}{K_E K_T T_E J} = \overline{K}_R \tag{4-10}$$

When condition (4-10) is complied, the function $f(K_R)$ will be positive. Because K_R is positive and real, the expression in line II of Table 4-1 is positive too:

$$K_R K_E K_T \cdot f(K_R) > 0 \qquad (4\text{-}11)$$

Finally that means, to guaranty stability of the given closed-loop position control model (Figure 4-4), K_R has to be within the range:

$$0 < K_R < \overline{K}_R \qquad (4\text{-}12)$$

4.2.3 Step response

The step response of the closed-loop position control shall be made as fast as possible without overshoot. As well-known, the step response depends on the roots of the denominator polynomial $D(s)$ of (4-8). The degree of this denominator polynomial is three ($n = 3$) and four cases of the roots can be distinguished:

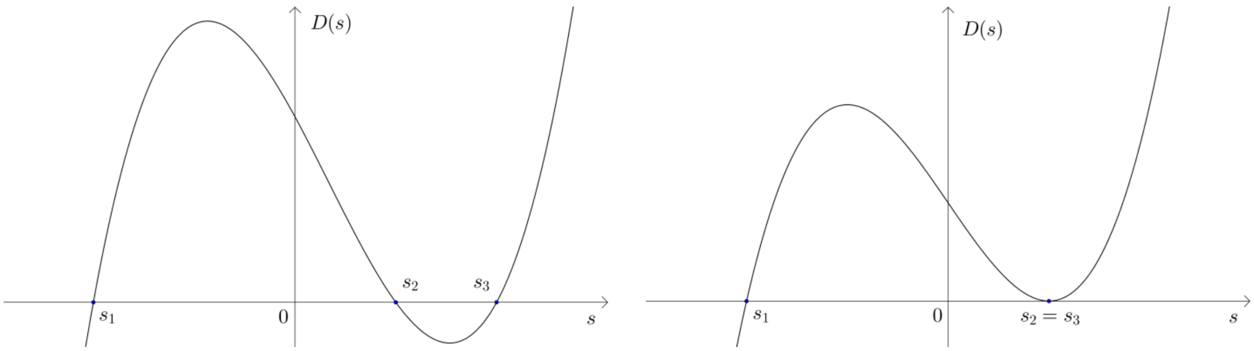

a) Case 1 **b) Case 2**

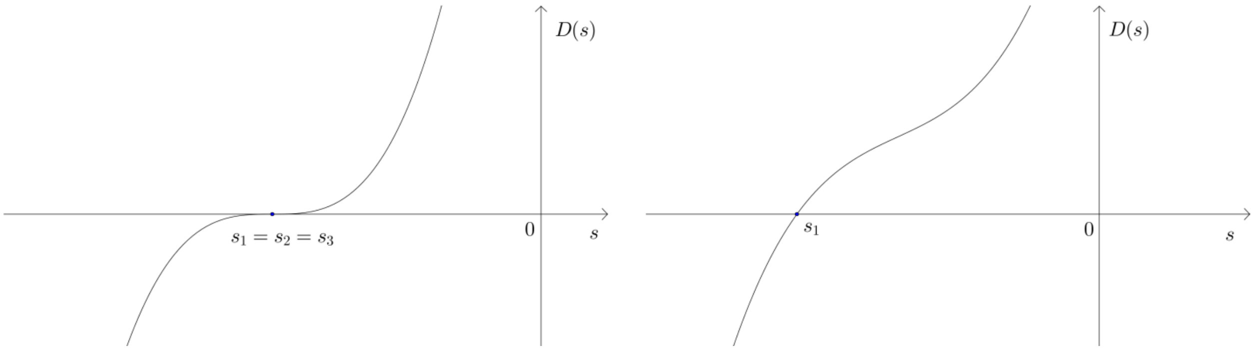

c) Case 3 **d) Case 4**

Figure 4-5: Four cases of polynomial roots

Extrema s_e per definition are points of the polynomial, where $D'(s_e) = 0$. Inflection points s_f per definition are points of the polynomial, where $D''(s_f) = 0$. If an extrema is also an inflection point, it is called a saddle point s_s and thereby applies $D'(s_s) = D''(s_s) = 0$. Using the slope of the denominator polynomial in the inflection point $D'(s_f)$ leads to sufficient and necessary conditions for the four cases, which are summarized in Table 4-2. Thereby, this table shows the possible cases for negative, zero or positive slope $D'(s_f)$ in the inflection point. As for positive slope $D'(s_f) > 0$ only one case is possible, this condition represents the sufficient condition for case 4. Zero slope $D'(s_f) = 0$ represents the necessary condition for case 3 and 4 and negative slope $D'(s_f) < 0$ the necessary condition for case 1, 2 and 4.

Table 4-2: Classification of the four root cases

Case	Roots	$D'(s_f) < 0$	$D'(s_f) = 0$	$D'(s_f) > 0$
1	3 real and all are different	X	-	-
2	3 real and two are equal	X	-	-
3	3 real and all are equal	-	X	-
4	1 real and 2 complex conjugate	X	X	X

As well as in a second-order system, the rise time of the servomotor step response in position-control decreases from case 1 to case 4. In order to obtain the fastest servomotor step response without overshoot, the highest possible case shall be pursued. Case 4 has to be avoided, since it produces oscillations in the step response. Without loss of generality, the denominator polynomial $D(s)$ (4-8) can be represented as a third-degree polynomial:

$$D(s) = a \cdot s^3 + b \cdot s^2 + c \cdot s + d \qquad (4\text{-}13)$$

, which has positive coefficients, due to positive system parameters. Because of the free tunable controller parameter K_R, the coefficient d is a function of this parameter:

$$d = f(K_R) \qquad (4\text{-}14)$$

Since the coefficient d is the constant term in the polynomial, the curve of $D(s)$ can only be moved vertically. Thereby, for example, case 1 can be converted to case 2. By forming the derivatives up to order n, a curve analysis can be made:

$$D'(s) = 3a \cdot s^2 + 2b \cdot s + c \tag{4-15}$$

$$D''(s) = 6a \cdot s + 2b \tag{4-16}$$

$$D'''(s) = 6a > 0 \tag{4-17}$$

Thus, that the third derivative is always positive, the curvature of $D(s)$ goes from right to left, like illustrated in Figure 4-5a to d. To determine the inflection point s_f, the second derivate has to be zero $D''(s_f) = 0$. Thereby results the inflection point:

$$s_f = -\frac{b}{3a} < 0 \tag{4-18}$$

Thus, the inflection point s_f is lying on the negative s-axis. The inflection point s_f is being used now in the first derivative to determine the slope of the polynomial in this point:

$$D'(s_f) = 3a \cdot s_f^2 + 2b \cdot s_f + c = c - \frac{b^2}{3a} \tag{4-19}$$

Because of the difference in expression (4-19), the slope in the inflection point $D'(s_f)$ can be negative, zero or positive, which leads to the following three distinctions:

4.2.3.1 Slope negative

If $D'(s_f) < 0$, generally case 1 is presented with $D(s)$ containing 3 real and different roots. The step response of the position-controlled servomotor (4-8) can be accelerated by vertically shifting curve $D(s)$ with the parameter d, so that case 1 gets converted to case 2. The parameter d can be calculated, by calculating the absolute value of polynomial $D(s)$ at his minimum. In this way, the polynomial has a tangential point to the s-axis, which leads to two equal roots in this point. Now the minimum of $D(s)$ has to be calculated and therefore the first derivative (4-15) has to be zero. The resulting second-order equation has to be solved for the variable s, which leads to two extrema:

$$s_{1,2} = \frac{-2b \pm \sqrt{4b^2 - 12ac}}{6a} \tag{4-20}$$

The expression under the square root must be positive, as two real extreme points exist (see Figure 4-5). Substituting these two extreme points in the second derivative leads to the distinction between maximum or minimum:

$$\begin{aligned} D''(s_{1,2}) &= 6a \cdot s_{1,2} + 2b \\ &= \pm\sqrt{4b^2 - 12ac} \end{aligned} \tag{4-21}$$

The second derivative is positive for a minimum, hence s_1 is the minimum:

$$s_1 = \frac{-2b + \sqrt{4b^2 - 12ac}}{6a} \tag{4-22}$$

Substituting s_1 in the polynomial and equating to zero $D(s_1) = 0$, gives the value for parameter d then:

$$d = -a \cdot s_1^3 - b \cdot s_1^2 - c \cdot s_1 \tag{4-23}$$

4.2.3.2 Slope zero

If $D'(s_f) = D''(s_f) = 0$, the inflection point represents a saddle point $s_f = s_s$ and using K_R, case 3 can be achieved. Thereby, the polynomial in this saddle point has to be zero $D(s_s) = 0$. Thus gives the value for parameter d then:

$$d = \frac{bc}{3a} - \frac{2b^3}{27a^2} \tag{4-24}$$

With the criterion (4-24) a value for K_R can be found, which in this case guaranties the fastest step response of the closed-loop position control. However, this case will be very improbably, due to parameter variations of the closed-loop, which makes $D'(s_f)$ not exact zero.

4.2.3.3 Slope positive

If $D'(s_f) > 0$, the polynomial $D(s)$ has always one real and two complex conjugate roots (case 4). Because of complex conjugate roots, the step response of the closed-loop position control is overshooting. With parameter d, the rise time and the overshoot of the step response can now be influenced in the following manner:

Table 4-3: Influence parameter d in case 4

Parameter d	Rise time	Overshoot
increasing	decreasing	increasing
decreasing	increasing	decreasing

4.2.4 Simulation Results

The theoretically results of section 4.2.2 and 4.2.3 shall be validated exemplary for the DC motor Maxon Motor RE-max29, using the system parameters from Table 13-1 (Appendix). First, the controller parameter K_R range shall be determined. Using equation (4-10) the value for $\overline{K}_R$ is calculated:

$$\overline{K}_R \approx 2103 \tag{4-25}$$

Assuming that the parameters would differ around its nominal values with a barrier of maximal 10%. Then $\overline{K}_R$ would only decrease, when the nominator of (4-10) will decrease and the denominator will increase. Thus leads to a minimum value of $\overline{K}_R$, which represents the worst case:

$$\overline{K}_{R_{min}} = \frac{0.9 \cdot r(0.9 \cdot J + 0.9^2 \cdot rT_E)}{1.1^4 \cdot K_E K_T T_E J} \approx 1161 \tag{4-26}$$

Similarly, a maximum value of $\overline{K}_R$ can be determined:

$$\overline{K}_{R_{max}} = \frac{1.1 \cdot r(1.1 \cdot J + 1.1^2 \cdot rT_E)}{0.9^4 \cdot K_E K_T T_E J} \approx 3856 \tag{4-27}$$

Like equation (4-26) shows the worst case, the upper limit of $\overline{K}_R$ would only decrease $\approx 20\%$ from its nominal value (4-25). For practical reasons, K_R will not exceed this value, hence the stability of the closed-loop position control model is ensured, even under large parameter variations of the controlled system. Second, the step response of the closed-loop position control (Figure 4-4) shall be optimized with the aim, to be as fast as possible without overshooting. Using the system parameters from Table 13-1, the polynomial $D(s)$ coefficients (4-8) can be calculated:

$$a = T_E \cdot J \qquad b = J + r \cdot T_E \qquad c = r \tag{4-28}$$

By equation (4-19) the slope in the inflection point s_f then is calculated:

$$D'(s_f) = c - \frac{b^2}{3a} \approx -0.0073 \tag{4-29}$$

Hence, for small values of K_R, case 1 is presented and the denominator polynomial $D(s)$ has three real and different roots. By equation (4-23) a value for the coefficient d (and thus also for K_R) shall be calculated so, that case 1 gets converted to case 2. Equation (4-22) gives the value for the minimum of the denominator polynomial:

$$s_1 = \frac{-2b + \sqrt{4b^2 - 12ac}}{6a} \approx -114.4096 \tag{4-30}$$

Now, the value for K_R can be calculated:

$$K_R = \frac{d}{K_E K_T} \approx 9.5624 \tag{4-31}$$

This optimal value is confirmed by simulating the step response of the closed-loop position control (Figure 4-4) for different amplification factors K_R of the P-controller, depicted in Figure 4-6. It can clearly be observed, that the value (4-31) is the optimal value for a fast step response time without overshooting:

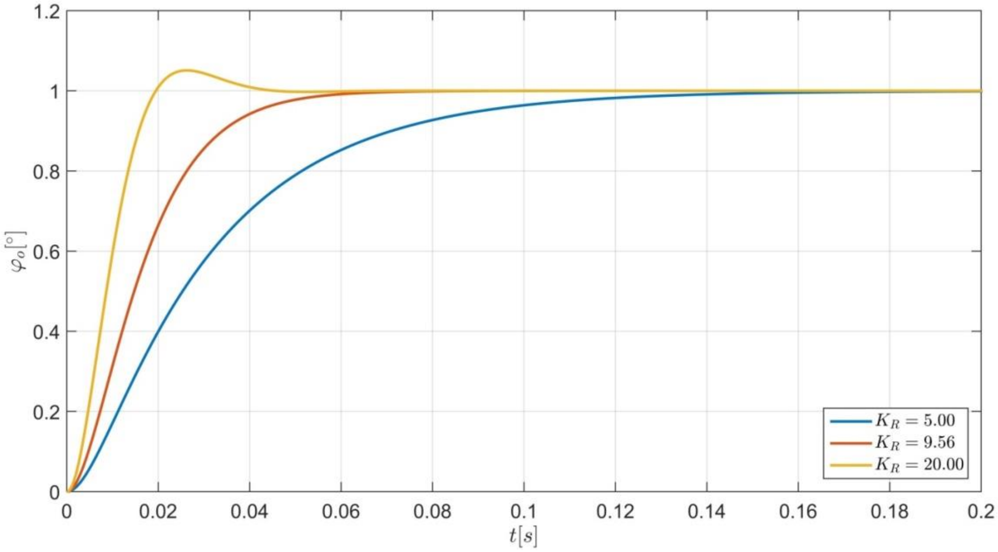

Figure 4-6: Maxon Motor RE-max29 closed-loop position-control

4.3 Speed Control

4.3.1 Closed-Loop Model

To optimize the speed-control of the servomotor, the DC motor (Figure 4-3) shall be controlled in a closed-loop using a PI-controller, depicted in Figure 4-7.

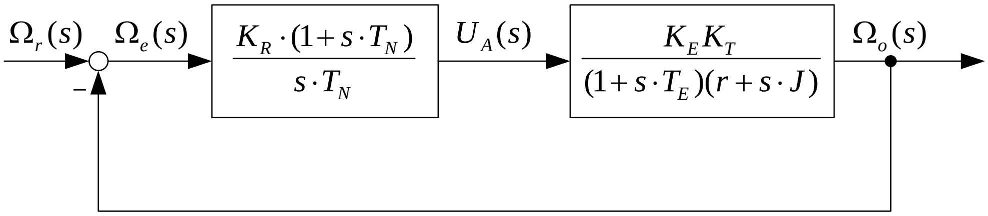

Figure 4-7: Closed-loop speed control model of a DC motor

It must be noted, that the integral part of the controller is needed to produce a continuous armature voltage U_A, when the angular speed error turns zero $\Omega_e = 0$. The actual angular speed Ω_o gets rested from the reference angular speed Ω_r and results in the angular speed error Ω_e:

$$\Omega_e = \Omega_r - \Omega_o \qquad (4\text{-}32)$$

The gain of the PI-controller is K_R and the reset time T_N. The open-loop transfer function of this control loop is defined by the product of the controller TF with the controlled system TF (4-4):

$$G_O(s) = G_R(s) \cdot G_S(s) = \frac{K_R \cdot (1 + s \cdot T_N)}{s \cdot T_N} \cdot \frac{K_E K_T}{(1 + s \cdot T_E)(r + s \cdot J)} \qquad (4\text{-}33)$$

The closed-loop TF of the speed control then can be calculated using $G(s) = \frac{G_O}{1+G_O}$:

$$G(s) = \frac{K_R K_E K_T \cdot (1 + sT_N)}{K_R K_E K_T + s(rT_N + K_R K_E K_T T_N) + s^2 T_N (J + rT_E) + s^3 (T_N T_E J)} = \frac{N(s)}{D(s)} \qquad (4\text{-}34)$$

4.3.2 Stability

It shall be analyzed the stability of the given closed-loop speed control model (Figure 4-7) and transfer function $G(s)$ (4-34), depending on the controller parameters K_R and T_N. As described in section 3.2, all zeros of the denominator polynomial:

$$D(s) = s^3(T_N T_E J) + s^2 T_N(J + rT_E) + s(rT_N + K_R K_E K_T T_N) + K_R K_E K_T \qquad (4\text{-}35)$$

must have a negative real part. Using the Routh Algorithm and the Routh Criterion, the stability of the transfer function $G(s)$ shall be determined. The Routh Algorithm gets applied for the denominator polynomial:

Table 4-4: Routh Algorithm for D(s)

	$T_N T_E J$	$T_N(r + K_R K_E K_T)$
	$T_N(J + rT_E)$	$K_R K_E K_T$
I:	$T_N^2(J + rT_E)(r + K_R K_E K_T) - K_R K_E K_T T_N T_E J = f(K_R, T_N)$	
II:	$K_R K_E K_T \cdot f(K_R, T_N)$	

According to the Routh Criterion, all expressions in the first column must have the same sign, so that the analyzed transfer function $G(s)$ is stable. As it can be seen from the first two lines, since the controller parameters K_R and T_N are positive and real, all expressions must be positive too. This condition can be used, to determine a condition for T_N. The function obtained in line I has to be positive:

$$T_N^2(J + rT_E)(r + K_R K_E K_T) - K_R K_E K_T T_N T_E J > 0 \qquad (4\text{-}36)$$

Solve the equation for T_N results in:

$$T_N > \frac{K_R K_E K_T T_E J}{(J + rT_E)(r + K_R K_E K_T)} \qquad (4\text{-}37)$$

Using L’Hoptial’s rule the upper limit of (4-37) can be determined:

$$\lim_{K_R \to \infty} \frac{K_R \cdot K_E K_T T_E J}{(J + rT_E)(r + K_R \cdot K_E K_T)} = \lim_{K_R \to \infty} \frac{K_E K_T T_E J}{(J + rT_E) K_E K_T} = \frac{T_E J}{J + rT_E} \tag{4-38}$$

When expression (4-37) is complied, the function $f(K_R, T_N)$ will be positive. Because K_R is positive and real, the expression in line II is positive too:

$$K_R K_E K_T \cdot f(K_R, T_N) > 0 \tag{4-39}$$

Finally that means, to guaranty stability of the given closed-loop speed control model (Figure 4-7), any positive value for K_R can be defined and with this a value for T_N using expression (4-37) be determined.

4.3.3 Step Response

The step response of the closed-loop speed control shall be made as fast as possible. Therefore, first shall be used the method of pole-zero-compensation [57]. This method uses the zeros of the controller to compensate “slow” poles of the controlled system and thereby reduce the step response rise time of the closed-loop. Slow poles of the controlled system means higher time constants in the denominator of the transfer function. The open-loop TF of the speed control (4-33) can be rewritten using (4-3):

$$G_O(s) = \frac{K_R \cdot (1 + s \cdot T_N)}{s \cdot T_N} \cdot \frac{K_E K_T r^{-1}}{(1 + s \cdot T_A)(1 + s \cdot T_M)} \tag{4-40}$$

Typically the mechanical part of a DC motor is slower than the electrical, so the following compensation will be made:

$$T_N = T_M = \frac{J}{r} \tag{4-41}$$

To guaranty stability of the closed-loop speed control, it shall be checked if T_N is greater, than the upper limit of (4-38):

$$\begin{gathered} \frac{J}{r} > \frac{T_E J}{J + rT_E} \\ J + rT_E > rT_E \end{gathered} \tag{4-42}$$

Because all system parameters are positive and real, equation (4-42) is true, hence the closed-loop speed control is stable. With $K = K_R K_E K_T r^{-1}$ the open-loop TF of the speed control (4-33) now is simplified to:

$$G_O(s) = \frac{K}{sT_N(1 + sT_E)} \tag{4-43}$$

The closed-loop TF of the speed control (4-34) is also simplified to:

$$G(s) = \frac{N(s)}{D(s)} = \frac{K}{K + sT_N + s^2 T_N T_E} = \frac{1}{1 + s \cdot \frac{T_N}{K} + s^2 \cdot \frac{T_N T_E}{K}} \tag{4-44}$$

The closed-loop TF now represents the normalized form of a second-order system:

$$G(s) = \frac{1}{1 + s \cdot 2D/\omega_0 + s^2 \cdot 1/\omega_0^2} \tag{4-45}$$

ω_0 represents the characteristic angular frequency and D the damping of the system. By comparing the coefficients of (4-44) and (4-45), the values of ω_0 and D can be determined:

$$\omega_0 = \sqrt{\frac{K}{T_N T_E}} \tag{4-46}$$

$$D = 0.5\sqrt{\frac{T_N}{K T_E}} \tag{4-47}$$

To comply the condition, that the step response of the closed-loop speed control shall be as fast as possible, the damping D must be equal 1. This corresponds to the second case of the homogeneous differential equation solution (critically damped). From this, the value of K_R can be calculated:

$$K_R = \frac{J}{4 K_E K_T T_E} \tag{4-48}$$

If this value increases, the system begins to oscillate (underdamped solution). If this value decreases, the step response will be slower (overdamped solution) than the critically damped step response.

4.3.4 Simulation Results

The theoretically results of section 4.3.2 and 4.3.3 shall be validated exemplary for the DC motor Maxon Motor A-max16, using the system parameters from Table 13-1 (Appendix). Since the value for K_R can be chosen free, it shall be calculated the upper limit of expression (4-37) using (4-38):

$$\frac{T_E J}{J + rT_E} = 3.629 \cdot 10^{-5} \tag{4-49}$$

This value is approximately zero, so from a practical standpoint T_N can have any real value greater than zero, to guaranty stability of the given closed-loop speed control model (Figure 4-7). To obtain the fast as possible without overshooting step response of Figure 4-7, equation (4-48) is substituted in (4-46):

$$\omega_0 = \frac{1}{2T_E} \tag{4-50}$$

Using the closed-loop TF of speed control (4-45), the characteristic angular frequency value (4-50) and the damping $D = 1$, the optimized speed control step response $\omega_o(t)$ to an unit step $\omega_r(t) = \sigma(t)$ can be derived [57]:

$$\omega_o(t) = 1 - \exp\left(-\frac{t}{2T_E}\right)\left(1 + \frac{t}{2T_E}\right) \tag{4-51}$$

This step response now depends only of the electrical time constant T_E. The optimized step response for the Maxon Motor A-max16 is shown in Figure 4-8.

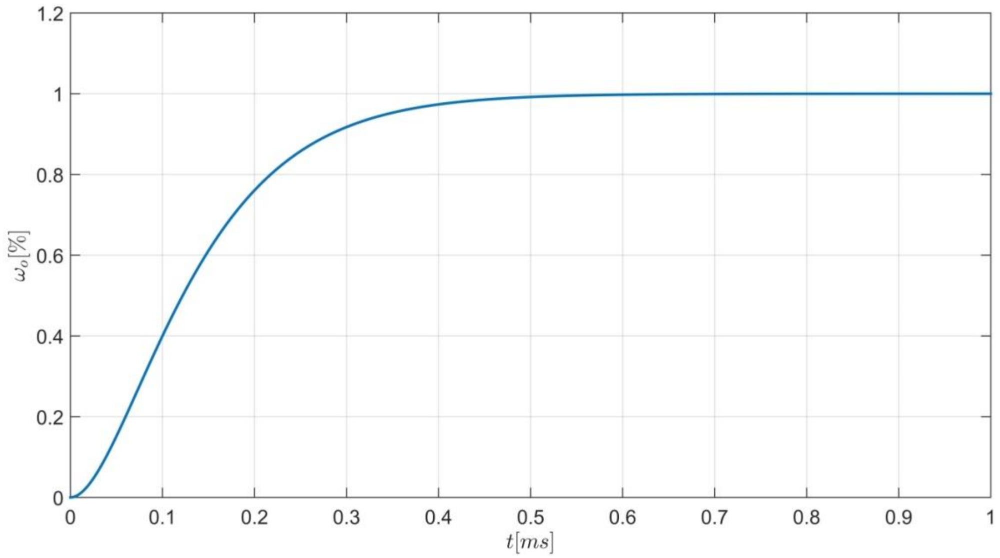

Figure 4-8: Maxon Motor A-max16 closed-loop speed-control

With compensation (4-41) and the value (4-48), the fastest step response of the servomotor without overshoot is achieved. It can be seen from Figure 4-8, that this motor reaches the reference speed in approximately $0.6ms$.

4.4 Frequency Response

4.4.1 Servomotor

The DC motor transfer function (4-4) represents a second-order transfer element or second-order low-pass filter, which can be expressed in the general form, using $T_1 = T_E$, $T_2 = T_M$ and $K_1 = \frac{K_E K_T}{r}$:

$$G_S(s) = \frac{K_1}{(1 + s \cdot T_1)(1 + s \cdot T_2)} \qquad (4\text{-}52)$$

Using $\tau_1 = T_1 T_2$ and $\tau_2 = T_1 + T_2$, the amplitude of the frequency response is given by:

$$|G_S(j\omega)| = \frac{K_1}{\sqrt{(1 - \omega^2 \tau_1)^2 + (\omega \tau_2)^2}} \qquad (4\text{-}53)$$

The cutoff angular frequency ω_c for the DC motor transfer function is defined by the following condition:

$$|G_S(j\omega_c)| \overset{!}{=} \frac{K_1}{\sqrt{2}} \qquad (\ 4\text{-}54\ )$$

Equating (4-53) and (4-54) yields the following fourth-degree polynomial for ω_c:

$$\omega_c^4\tau_1^2 + \omega_c^2(\tau_2^2 - 2\tau_1) - 1 = 0 \qquad (\ 4\text{-}55\ )$$

, which contains the following two zeros for ω_c^2:

$$\omega_c^2 = \frac{-(T_1^2 + T_2^2) \pm \sqrt{T_1^4 + T_2^4 + 6(T_1T_2)^2}}{2(T_1T_2)^2} \qquad (\ 4\text{-}56\ )$$

Since real frequencies are represented by positive values, only the first solution is considered. By the same reason, the cutoff frequency f_c for the DC motor now is determined by:

$$f_c = \frac{\omega_c}{2\pi} \qquad (\ 4\text{-}57\ )$$

Using exemplary the DC motor Maxon RE-max29 (Table 13-1), equation (4-57) gives the cutoff frequency:

$$f_c \approx 36.5776\ Hz \qquad (\ 4\text{-}58\ )$$

, which can be confirmed by sketching the Bode Plot of the DC motor transfer function $G_S(s)$.

4.4.2 Servomotor Output

The applied armature input voltage $u_A(t)$ to the DC motor is a PWM signal. To determine the continuous frequency spectrum of the PWM signal, a single rectangular pulse with pulse duration τ is considered and transformed using Laplace. This single rectangular pulse is mathematically defined and described in following section 5.5. Following equation for the rectangular pulse is defined there:

$$U_A(s) = \frac{\tau}{1 + 0.5\tau s} \tag{4-59}$$

Using $T_1 = T_E$, $T_2 = T_M$ and $K_2 = \frac{K_E K_T \tau}{r}$, the actual angular speed $\Omega_o(s)$ as output of the DC motor is expressed as:

$$\Omega_o(s) = G_S(s) \cdot U_A(s) = \frac{K_2}{(1 + s \cdot T_1)(1 + s \cdot T_2)} \cdot \frac{1}{(1 + 0.5\tau s)} \tag{4-60}$$

Using $\tau_1 = \frac{\tau}{2} T_1 T_2$, $\tau_2 = \frac{\tau}{2}(T_1 + T_2) + T_1 T_2$ and $\tau_3 = \frac{\tau}{2} + T_1 + T_2$, the amplitude of the frequency response is given by:

$$|\Omega_o(j\omega)| = \frac{K_2}{\sqrt{(1 - \omega^2 \tau_2)^2 + \omega^2 (\tau_3 - \omega^2 \tau_1)^2}} \tag{4-61}$$

The cutoff angular frequency ω_c of the DC motor actual angular speed is defined by the following condition:

$$|\Omega_0(j\omega_c)| \overset{!}{=} \frac{K_2}{\sqrt{2}} \tag{4-62}$$

Equating (4-61) and (4-62) yields the following sixth-degree polynomial for ω_c:

$$\omega_c^6 \tau_1^2 + \omega_c^4 (\tau_2^2 - 2\tau_1 \tau_3) + \omega_c^2 (\tau_3^2 - 2\tau_2) - 1 = 0 \tag{4-63}$$

The analytic determination of the zeros of (4-63) turns out to be a complex task, since the polynomial is of sixth-degree. Therefore, using approximations, the polynomial coefficients shall be simplified. Since in practice, a small PWM period T_{PWM} is used and the electrical time constant of a DC motor is always much smaller than the mechanical one, the following two conditions can be defined:

$$\tau = dT_{PWM} \ll T_2 \tag{4-64}$$

$$T_1 \ll T_2 \tag{4-65}$$

Using these conditions for equation (4-63), approximated values for the polynomial coefficients shall be derived:

$$\tau_1^2 = \left(\frac{\tau}{2} T_1 T_2\right)^2 \approx 0 \qquad (4\text{-}66)$$

$$\tau_2^2 - 2\tau_1\tau_3 = \frac{\tau^2}{4}(T_1^2 + T_2^2) + (T_1T_2)^2 \approx \frac{\tau^2}{4} T_2^2 + (T_1T_2)^2 \qquad (4\text{-}67)$$

$$\tau_3^2 - 2\tau_2 = \frac{\tau^2}{4} + T_1^2 + T_2^2 \approx T_2^2 \qquad (4\text{-}68)$$

Using the approximation (4-66) and that (4-67) ≪ (4-68) , the polynomial (4-63) is reduced to:

$$\omega_c^2 T_2^2 - 1 = 0 \qquad (4\text{-}69)$$

, which gives the cutoff frequency f_c for the DC motor actual angular speed:

$$f_c = \frac{1}{2\pi \cdot T_2} \qquad (4\text{-}70)$$

Using the DC motor Maxon RE-max29 (Table 13-1), equation (4-70) gives the cutoff frequency:

$$f_c \approx 36.5904\, Hz \qquad (4\text{-}71)$$

Because of equality of the cutoff frequency of the DC motor (4-58) and the DC motor actual angular speed (4-71), it is shown, that all frequency components of the PWM signal above the cutoff frequency f_c are blocked. That is, by complying condition (4-64), the second-order low-pass filter behavior of the DC motor ensures, that all harmonics of the PWM signal are filtered and that the DC motor armature voltage $u_A(t)$ is approximated using only the PWM DC value:

$$u_A(t) \approx u_N d = u_N y \qquad (4\text{-}72)$$

Where the applied armature voltage depends proportionally to the PWM duty cycle and thus to the controller output variable $y(t)$. For a duty cycle $d = 1$, condition (4-64) can be rewritten

$$f_{PWM} \gg \frac{1}{T_2} \tag{4-73}$$

Besides the minimal value for the PWM frequency defined by (4-73), it must be considered, that a higher PWM frequency results in more switching and thereby power losses in the motor inductances. Thus, motor heating is increased, which reduces the overall lifetime of itself. A PWM frequency lower than $\frac{1}{T_2}$ is manifested by vibrations of the DC motor caused by the PWM signal harmonics.

It must be noted, that the resolution of the controller output variable y defines the resolution of the armature voltage u_A. That is, the higher the resolution of y, the finer the armature voltage u_A can be adjusted. The next chapter 5 shows, that the controller output variable resolution TOP and the PWM frequency f_{PWM} are two mutual excluding conditions. A good and practical compromise between these two conditions is found by experimentation (chapter 9).

5 Digital Control Design for faster Positioning of DC Motor

To realize the theoretical method for continuous triangulation, the proposed DC motors are digitally controlled, using a digital controller, motor driver, digital-analog (D/A, DAC) and analog-digital converter (A/D, ADC), as depicted in Figure 5-1. Here, k represents discrete time points of the continuous time t.

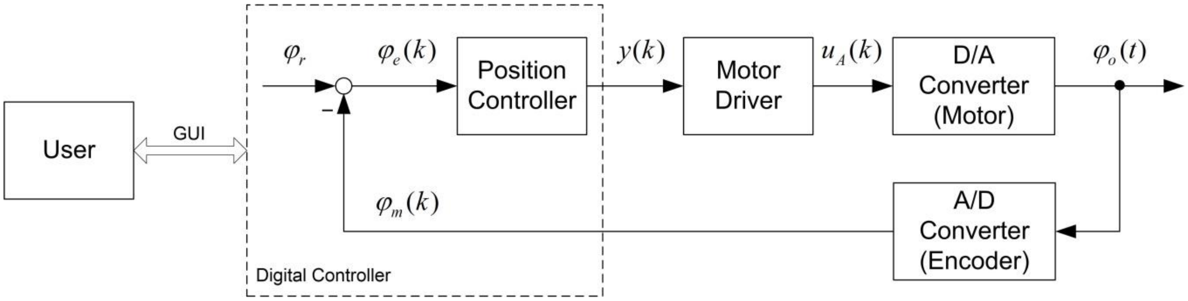

Figure 5-1: Digital sampling loop

The digital controller is implemented using a Microcontroller, which receives a constant reference value φ_r, calculates the current error $\varphi_e(k)$ and uses an algorithm to calculate the current controller output variable $y(k)$. Since digital controllers only have two signal levels as output signals, the discrete amplitudes of the output variable $y(k)$ must be represented using a Pulse-Width-Modulated signal (PWM). In order to generate the required power for the DC motor, the output variable $y(k)$ must be amplified to the DC motor armature voltage $u_A(k)$ using the motor driver, which is realized by an electronic H-Bridge. The DAC is represented by the same DC motor, which due to his second-order low-pass filter behavior converts the discrete values of the DC motor armature voltage $u_A(k)$ into continuous values of the actual angular position $\varphi_o(t)$. The continuous values of $\varphi_o(t)$ again are converted into a pulse sequence by the ADC, which is represented by the Incremental Encoder. Counting the pulses of this sequence, the digital controller than determines the measured angular position $\varphi_m(k)$ and measured angular speed $\omega_m(k)$. Present chapter describes in detail the main concepts of digital controller, the needed microcontroller timer, PWM signals, H-Bridge and Incremental Encoder of the used DC Motor.

5.1 Digital Controller

In modern control technology, mostly digital controllers are being used, since they have significant advantages over analog controllers. Thereby, Table 5-1 compares advantages and disadvantages of analog vs. digital controller.

Table 5-1: Analog vs. Digital Controller

	Analog	**Digital**
Advantages	No inherent bandwidth limitations, due to continuously operating principle. Controller can build up robust, since no algorithm is used, which can break down.	Flexibility of algorithm implementation, easy to modify and to develop. Less sensitive to component drift due to temperature influence. Possibility to backup controller algorithm. Usage of memory to store signals. Possibility to integrate intelligence, like adaptive filtering, error detection, diagnostic routines, signal generation, etc.
Disadvantages	Parameters of controller are temperature dependent, thereby changing system properties (e.g. changing amplification factors, time constants, etc.). Complicate to modify, testing alternatives is laborious. No possibilities to backup system easily.	Inherent bandwidth limitations, due to discontinuously operating principle. Can crash due to internal conflict states. By discretization of input and output variables, an inevitable systematic error is added to the values.

5.2 Sampling Loop

The transition from an analog to a digital controller is accomplished by the implementation of the control algorithm using a microcontroller, which constitutes a Sample and Hold-element $H(s)$ (S&H). The S&H-element is described mathematically in the complex variable domain s by a zero-order holding element, with T_S representing the sampling period and $f_S = \frac{1}{T_S}$ the sampling rate:

$$H(s) = \frac{1}{s} \cdot (1 - e^{-sT_S}) \qquad (5\text{-}1)$$

, and in the time domain t described by the sum of two unit step functions:

$$h(t) = \mathcal{L}^{-1}\{H(s)\} = \sigma(t) - \sigma(t - T_S) \qquad (5\text{-}2)$$

The sum of two unit step function gives a rectangular pulse with pulse length equal the sampling period T_S, depicted in Figure 5-2:

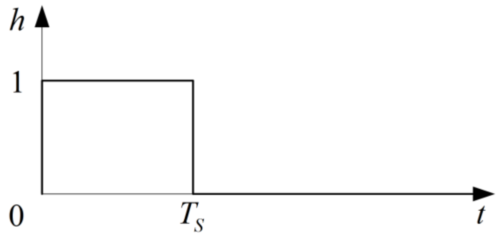

Figure 5-2: Sample and Hold Element

Using the S&H-element, a continuous time signal $y = f(t)$ is sampled at equidistant time points $t_k = k \cdot T_S$, with $k \in \mathbb{N}$ and $t \in \mathbb{R}$. The time-discretized signal is depicted in Figure 5-3:

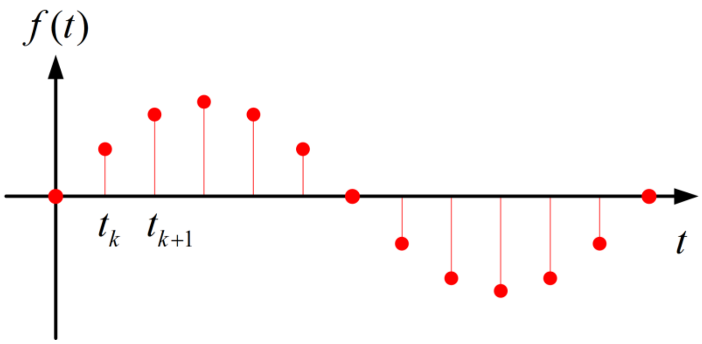

Figure 5-3: Time discretization

Sampling replaces the continuous time signal $y = f(t)$ by a Sequence of Values $\{f[k]\} = \{f[0], f[1], f[2], \dots\}$, which due to the limited storage of a digital controller only consists of a set of discrete values. The amplitude-quantized signal is depicted in Figure 5-4:

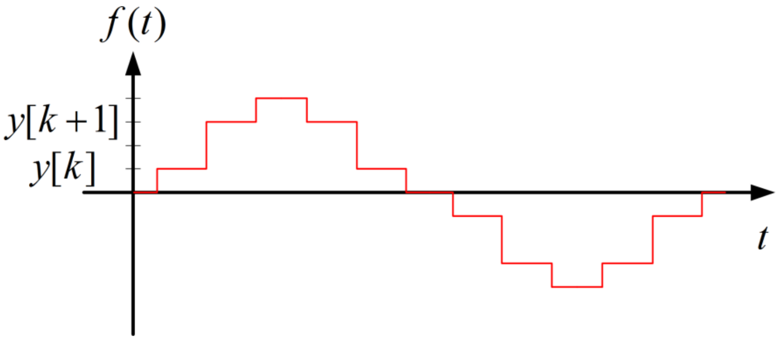

Figure 5-4: Amplitude quantization

Signals discretized in time and quantized in amplitude are called digital signals used by digital controllers, which are stored as floating-point (float) or fixed-point (integer) numbers. Table 5-2 shows the range of float- and integer-numbers used by Atmel´s AVR microcontrollers.

Table 5-2: Float and integer range in Atmel's AVR

	Precision	Min	Max	Smallest Number
Float	8	-3.4028235E+38	3.4028235E+38	0.0000001
Integer	10	-2147483648	2147483647	1

Comparing these ranges, it can be seen that float-numbers have 8 digits and integer-numbers 10 digits of precision. This higher resolution of integer-numbers presents one advantage over float-numbers, besides other negative effects of floating-point arithmetic, like round-off error, loss of significance, invalidity of associative and distributive property, etc. So, the digital control algorithm may comprise a more analog behavior, the higher is the resolution of the internal variables. The latter refers to the smallest representable number, which can be expressed by the used datatype and is shown in the last column of Table 5-2. Because of the limited number of presentable digits, every stored float-number can be converted to an integer-number by multiplying with the corresponding ten-power, which is called fixed-point arithmetic, for example:

$$0.123 \cdot 10^3 = 123 \tag{5-3}$$

5.3 Microcontroller Timer

5.3.1 16-bit Timer1

The positioning algorithm is implemented in the microcontroller (Arduino Uno) using Timer1 for PWM generation and calling the positioning algorithm with the sampling period T_S, using a timer overflow interrupt (TOV). To produce a PWM signal with a defined resolution and frequency, Timer1 is programmed in Fast PWM Mode, which is depicted in Figure 5-5.

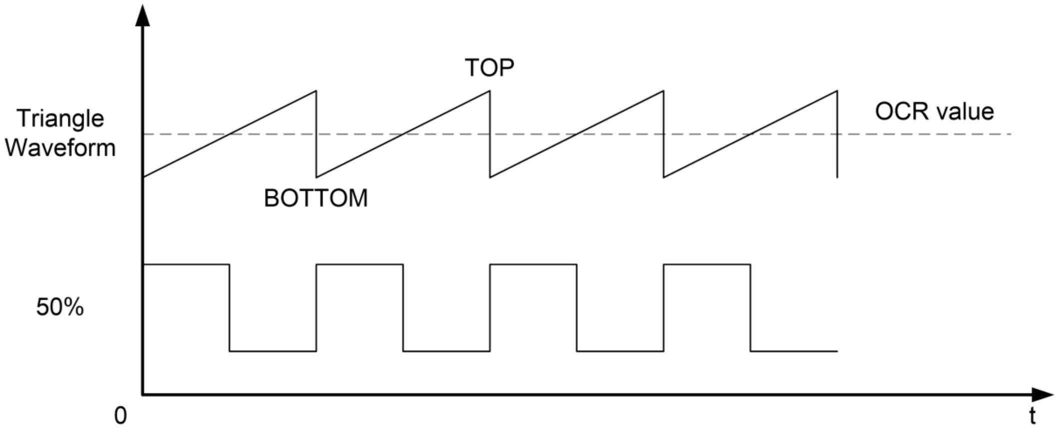

Figure 5-5: Timer1 PWM generation in Fast PWM Mode

Using the CPU clock rate f_{CPU} of the microcontroller, the counter of Timer1 is counting from BOTTOM (zero value) to a defined TOP value and constantly compared to a defined OCR value. The output logical level on a specific microcontroller pin is set using following conditions:

$$\begin{array}{c}\text{Counter} < \text{OCR value} \Rightarrow \text{HIGH} \\ \text{Counter} > \text{OCR value} \Rightarrow \text{LOW}\end{array} \qquad (\ 5\text{-}4\ )$$

Atmel´s AVR microcontrollers contain two PWM pins (or PWM channels) for each timer, so a positive and negative rotation of the DC motor can be generated using the H-bridge. So, with the TOP value the PWM frequency f_{PWM} is defined and with the OCR and TOP value the duty cycle (5-9):

$$d = \frac{\tau}{T_{PWM}} = \frac{OCR}{TOP} \qquad (\ 5\text{-}5\ )$$

The resolution of this duty cycle is also defined by the TOP value. Because Timer1 represents a 16-bit timer, the TOP value must comply following condition:

$$\text{TOP} \leq 65535 \tag{5-6}$$

and depends mutual with f_{PWM} on the CPU clock rate f_{CPU} of the microcontroller:

$$f_{CPU} = TOP \cdot f_{PWM} \tag{5-7}$$

That is, with higher duty cycle resolution, the PWM frequency is decreasing and vice versa with lower duty cycle resolution, the PWM frequency is increasing. Here, two mutual excluding conditions are presented: A) High duty cycle resolution or B) High PWM frequency. To realize a quasi-continuous control, these two conditions both must be as high as possible, because analogue controllers do not possess a sampling period and the resolution of the output signals is infinity.

The timer overflow interrupt (TOV) is used, to call and execute the positioning algorithm with a fixed sampling period $T_S \geq T_{PWM} = \frac{1}{f_{PWM}}$. This also ensures that the controller output variable $y(t)$ does not change more quickly, as the duty cycle of the PWM signal. The opposite would violate the Principle of Causality.

5.3.2 8-bit Timer2

Timer2 is used to trigger the microcontroller serial communication on equidistant points and is therefore programmed in Clear Timer on Compare Match (CTC) Mode. Like Timer1, the counter of Timer2 also is counting from BOTTOM (zero value) to a defined TOP value (Figure 5-5), using the CPU clock rate f_{CPU} of the microcontroller and generates a timer compare match interrupt (COMPA) to trigger the serial communication. Like the serial communication is a very time-consuming process and the microcontroller shall use primary CPU time for position control of the DC motor, the execution period of the serial communication is chosen with $T_{serial} = 500ms$. This period is far greater, than the positioning time of the DC motor, see experimental results.

5.4 Microcontroller USART

The Universal Synchronous and Asynchronous serial Receiver and Transmitter (USART) represents a serial communication device, using a protocol operating with 0V and 5V. The Transmitter consists of a Write Buffer, a Transmit Shift Register, a Parity Generator and control logic to configure different serial frames. The Receiver includes a Receive Shift Register, a Parity Checker, control logic and a two level receive buffer. The USART transmits serial data over the TX pin and receive data on the RX pin. It sends a serial frame, which represents a character of data bits with start and stop bits used to synchronize the frame. The USART uses the following possible frame formats:

- 1 start bit
- 5 to 9 data bits
- Even, odd or none parity bit
- 1 or 2 stop bits.

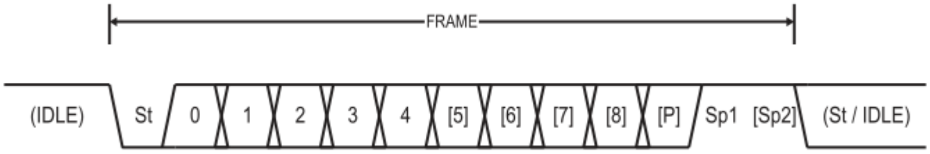

Figure 5-6: Serial frame formats

The order of this possible frame formats is shown in Figure 5-6 and explained in Table 5-3.

Table 5-3: Serial frame bits

Symbol	Description
St	Start bit, always low.
(n)	Data bits (0 to 8).
P	Parity bit. Can be odd or even.
Sp	Stop bit, always high.
IDLE	No transfer on the communication line. An IDLE line must be high.

To communicate between two devices, they have to use the same Transfer Rate in bits per second, called baud rate. Atmel's microcontrollers use a register to configure the baud rate (UBRRn), USART Baud Rate Register. The following expression is used to determinate that register value considering the baud rate $BAUD$ and system oscillator clock frequency f_{CPU}:

$$\frac{f_{CPU}}{16 \cdot Baud} - 1 \tag{5-8}$$

To use USART practically, the USART has to be initialized, the baud rate been set, the frame format and TX and RX enabled. Most usual values also used by the Arduino Uno are: 1 start bit, 8 data bits, no parity and 1 stop bit.

The USART share the same register to send and receive data. To transmit, the data register should be empty and the program has to wait until the UDRE (USART Data Register Empty) flag is set, then the data is loaded in the shift register and transmitted to the TX pin. To receive data, the USART verifies if there is unread data buffered in the data register. In that case, the data is stored in another register, the data register is cleared again and prepared to receive or transmit more data.

Receiving and transmitting serial data can be performed in two different modes: Polling Mode and Interrupt Mode. In polling mode, the microcontroller checks continuously or every certain time period the status of a specific flag. When the flag is set, the microcontroller performs the programed action to receive or transmit serial data. The polling mode is the simplest way to interact with external devices, but it consumes program execution time from the microcontroller. More suitable is the interrupt mode, which uses interrupt requests given to the microcontroller, when receiving or transmitting serial data. These requests interrupt the actual program execution and start a subroutine, specified by the interrupt, as response to the interrupt. Using interrupts make the communication happens at the same instant the data is ready to be transmitted or available in the buffer to be read.

5.5 Pulse-width Modulation

Because the used microcontroller does not possess an analog output, the obtained controller output variable $y(t)$ is converted to the armature voltage u_A using a pulse-width modulated signal (PWM), which varies the ratio between on time (τ) and a fixed period ($T_{PWM} = \frac{1}{f_{PWM}}$) of a Square Wave Signal, called duty cycle d. Here, the obtained controller output variable $y(t)$ corresponds to the duty cycle:

$$d = \frac{\tau}{T_{PWM}} = y \tag{5-9}$$

and Figure 5-7 shows pulse series with a duty cycle of $d = 25,\ 50$ and 75%, where H represents a high and L a low logic level:

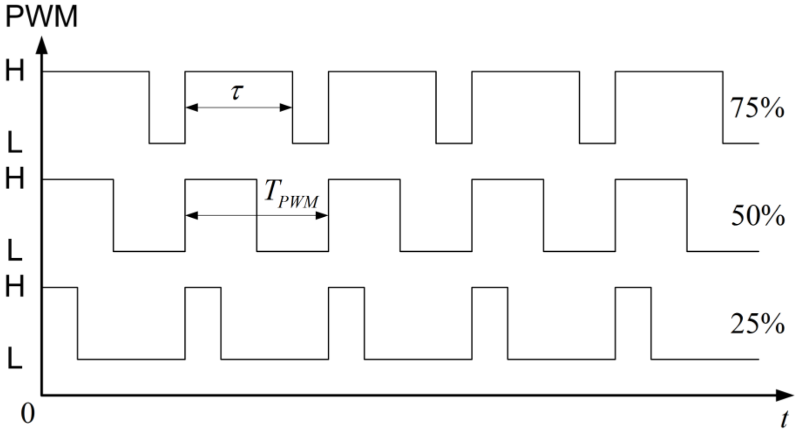

Figure 5-7: Pulse-width modulated signal

With this PWM signal, an H-bridge is controlled, which generally consists of four MOSFET's and drives the DC motor using its nominal voltage u_N. Thereby, the high level H represents the PWM amplitude A with value u_N Volt and the low level L represents the PWM ground with value 0 Volt. By applying of Fourier Series, the PWM square wave can be described mathematically by an infinite function series of sine and cosine functions:

$$f(t) = Ad + \frac{2A}{\pi}\left[\sin(\pi d)\cos(\omega t) + \frac{\sin(2\pi d)}{2}\cos(2\omega t) + \frac{\sin(3\pi d)}{3}\cos(3\omega t) + \cdots\right] \tag{5-10}$$

Here, the amplitude $A = u_N$ and the angular frequency ω corresponds to the PWM angular frequency $\omega_{PWM} = 2\pi f_{PWM}$ and thereby:

$$f(t) = u_N d + \frac{2u_N}{\pi}\sum\nolimits_{n=1}^{\infty} \frac{\sin(n\pi d)}{n} \cos(n\omega_{PWM} t) \tag{5-11}$$

So, the DC value of the PWM signal is described by $u_N d$ and the frequency of the nth harmonics by nf_{PWM}.

By forming the limit value of $T_{PWM} \to \infty$, the periodic PWM signal is converted into an aperiodic rectangular pulse (known from section 5.2) with pulse duration τ:

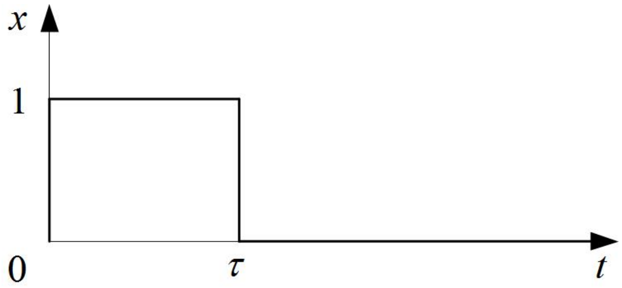

Figure 5-8: Aperiodic PWM Signal

The Laplace Transform $F(s)$ of the rectangular pulse is given by:

$$F(s) = \frac{1}{s}(1 - e^{-\tau s}) \tag{5-12}$$

Using the First-order Padé Approximation, equation (5-12) can be represented as follows:

$$F(s) \approx \frac{1}{s}\left(1 - \frac{1 - 0.5\tau s}{1 + 0.5\tau s}\right) = \frac{\tau}{1 + 0.5\tau s} \tag{5-13}$$

5.6 H-Bridge

An H-Bridge, also called four-quadrant chopper, typically consists of four semiconductor circuits using MOSFET transistors, which can convert a DC into an AC voltage with variable-frequency and variable pulse width. H-bridges are mostly used for power inverters, as motor controller and for other power electronic applications. For the application as motor controller, Figure 5-9 shows a schematic of the H-bridge, containing four transistors T1-T4, four flyback diodes D1-D4 and the controlled DC motor:

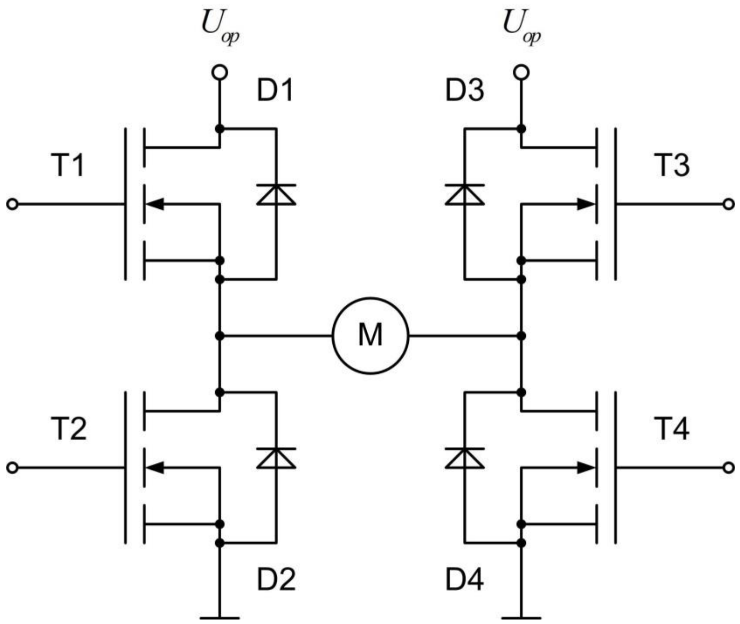

Figure 5-9: H-Bridge Schematic

Depending on the switching states of the four transistors, generally 3 operating modes of the H-Bridge can be defined: Motor-, Generator- and Freewheel-Mode. Table 5-4 summarizes the operating modes, where 0 means switched off and 1 switched on:

Table 5-4: Operating modes of an H-Bridge

Mode	T1	T2	T3	T4	Comment
Freewheel	0	0	0	0	Free Rotation
Motor	1	0	0	1	Accelerate Clockwise
Motor	0	1	1	0	Accelerate Counterclockwise
Generator	0	1	0	1	Braking Clockwise
Generator	1	0	1	0	Braking Counterclockwise

Short	1	1	0	0	Forbidden State
Short	0	0	1	1	Forbidden State
Short	1	1	1	1	Forbidden State

In Motor-Mode, the DC motor consumes electrical and converts it to mechanical power. For DC motor constant speed, a constant signal is applied to T1 and T4. For DC motor variable speed, a PWM signal is applied to T1 and T4 is switched on. The motor inductance is magnetized during the switch-on phase of T1 and the motor is accelerated. In the switch-off phase of T1, the motor winding induces a voltage and the current continues to flow through D2, which decreases the magnetization of the motor inductance. If the current decreases to zero during demagnetization, this is referred to intermittent operation, otherwise to not- intermittent operation of the DC motor. For the opposite rotation direction of the DC motor, a PWM signal is applied to T2 and T3 is switched on.

The Generator-Mode is used to brake the DC motor actively in both directions. For this, the DC motor is short-circuited via ground or via the operating voltage U_{op}. Thereby, the current generated by the motor is only limited by the resistive losses and the mechanical power is converted completely into heat. In Freewheel-Mode, the DC motor is neither accelerated nor braked. It is used to allow the motor to coast until standstill. The Short-Mode represents a forbidden operating state of the H-Bridge, which must be avoided under all circumstances, as otherwise the operating voltage is short-circuited to ground.

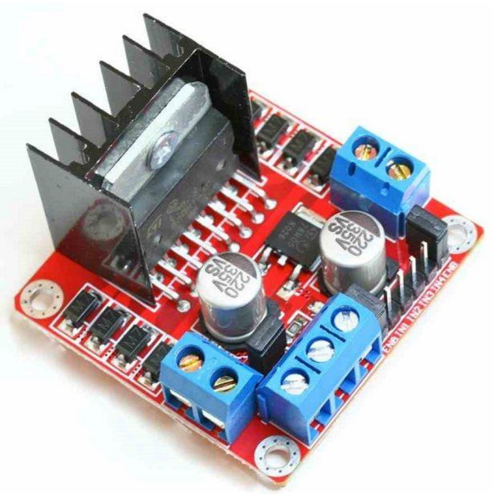

Figure 5-10: L298N Driver Module

H-Bridges can be built from discrete components or used as an integrated circuit (IC), where the L298 is one of the most commonly used. The L298 IC contains two independent H-Bridges, is capable of supporting current up to $2A$, is controlled using standard TTL logic and drives inductive loads like stepping and DC motors. To further simplify the general use of the L298 IC, the L298N Driver Module is used, to control the DC motors of the new TVS prototype No.3 (Figure 5-10). By use of PCB header connectors and terminal blocks, the connection of supply voltage and DC motor cables is very simplified. The L298N module can drive DC motors using a nominal voltage between 5 and $35V$ and using an onboard $5V$ regulator allows sourcing of external devices. Using jumpers, different functions of the module can be preset. More information of general use and application of the L298 IC and the L298N driver module can be found widely in online sources.

5.7 Incremental Encoder

Incremental encoders deliver phase shifted square-wave pulses on two channels A and B, to measure the precise actual angular position and speed of the motor. The used incremental encoder MR Type ML from Maxon Motors provides 1000 pulses on each channel and per revolution ($1000ppr$) of the motor and contains in addition an index channel I, which provides $1ppr$. Figure 5-11 shows the pulse sequence of channel A and B, when turning clockwise (CW). When turning counterclockwise (CCW), the pulse sequence of channel A and B are interchanged.

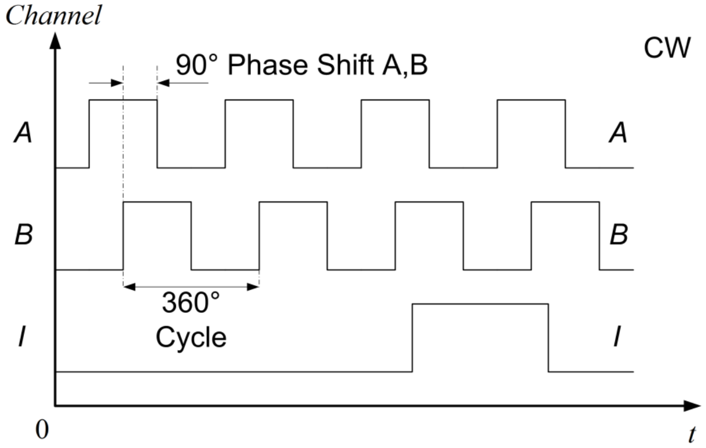

Figure 5-11: Incremental encoder with index channel

The resolution of the actual angular position of the motor is limited by these pulses. To increase the resolution, the incremental encoder is considered as a State Machine with 4 states, which sequence is defined by the revolution direction (Figure 5-12). H thereby represents a high and L a low logic level.

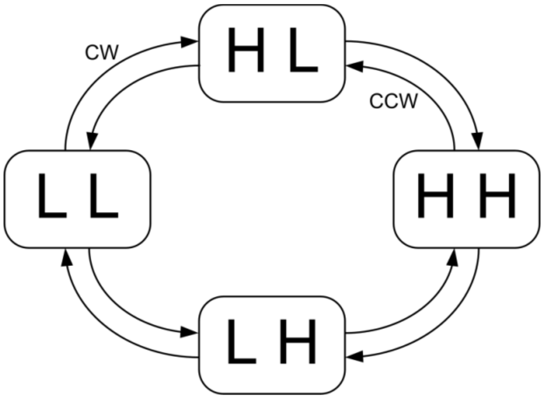

Figure 5-12: Incremental encoder state machine

By detecting the actual state of channel A after a state change (rising or falling edge) and comparing it to the last state of channel B, it can be determined a CCW rotation, if this two states are equal. Otherwise, if these two states are not equal, a CW rotation is determined. By detecting the rising and falling edge of channel A, the resolution of $1000ppr$ is doubled. By applying this procedure vice versa for channel B, it can be doubled again the resolution to a maximum resolution of $4000ppr$. The maximum resolution now is defined by $\frac{360°}{4000} = 0.09°$, which defines the maximum possible angular position resolution of the used incremental encoder.

6 Technical Vision System

The Technical Vision System (TVS) predecessor prototype No.2 was developed at the Laboratory of Optoelectronics and Automated Measurement of the UABC. The TVS consists mainly in a laser scanning system, which uses dynamic triangulation, to obtain 3D coordinates of any examined object. Although the TVS has replaced the disadvantages of camera light sensors by use of a single-sensor detector, it still operates with stepping motors. As novel approach, the present work proposes the substitution of these stepping motors by servomotors, to eliminate the disadvantage of a discrete FOV and replace it with a continuous behavior of scanning element. By replacing the measurement principle of a discrete FOV with a continuous one, the discretization of the FOV for 3D coordinate measurement is no longer a physical limitation. Thereby applications become possible, which were previously limited by the fixed step size or by the distance to the examined object. The technical realization of this substitution will be the TVS successor prototype No.3, described in this chapter. Therefore, firstly technical details and functionality of the prototype No.2 are described for the two principle mechanical parts, represented by the Positioning Laser and the Scanning Aperture. In the second part of the chapter, the new TVS successor prototype No.3 containing the new Positioning Laser and Scanning Aperture will be introduced.

6.1 Prototype No.2

The TVS prototype No.2 is composed of two principle mechanical parts: the Positioning Laser (PL) and the Scanning Aperture (SA) [43], which can be seen in the technological scheme in Figure 6-1:

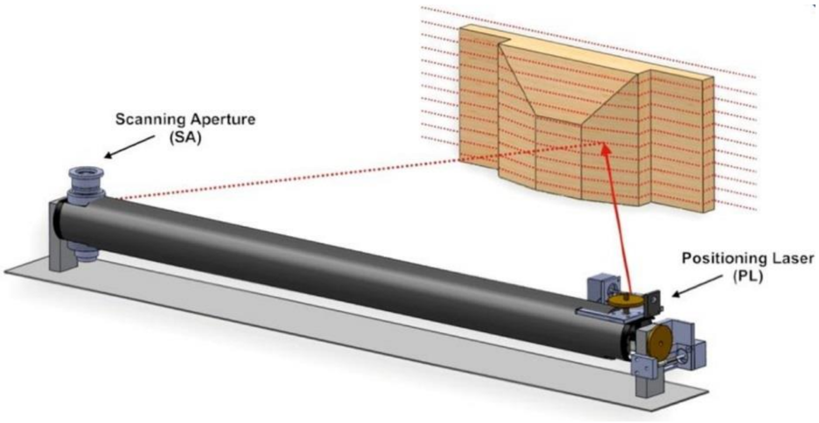

Figure 6-1: Technical Vision System (TVS) prototype No.2 [43]

The TVS varies the PL angle γ using stepping motors model 42BYGH404-R and the SA angle β using a DC motor in open-loop configuration.

6.1.1 Positioning Laser

The Positioning Laser, depicted in Figure 6-2, basically consists of two 45° staggered mirrors, a red laser (635 nm, 20 mW) and two stepping motors, to position the laser beam in the FOV. Figure 6-2a shows the system view (physical representation) of the two stepping motors with their respective transmissions (worm gears). The upper stepping motor (I in Figure 6-2a) is responsible for the laser beam horizontal positioning by rotating one 45° staggered mirror over a transmission. Figure 6-2b shows a schematic view of the two staggered mirrors, including the optical path of the laser beam. Coming from the laser source, the beam gets redirected by the first mirror (I in Figure 6-2b) upwards to the second mirror (II in Figure 6-2b), which in turn deflects the laser beam forward into the TVS field of view. The lower stepping motor (II in Figure 6-2a) is responsible for the laser vertical positioning, by rotating the entire TVS around its horizontal axis over a transmission.

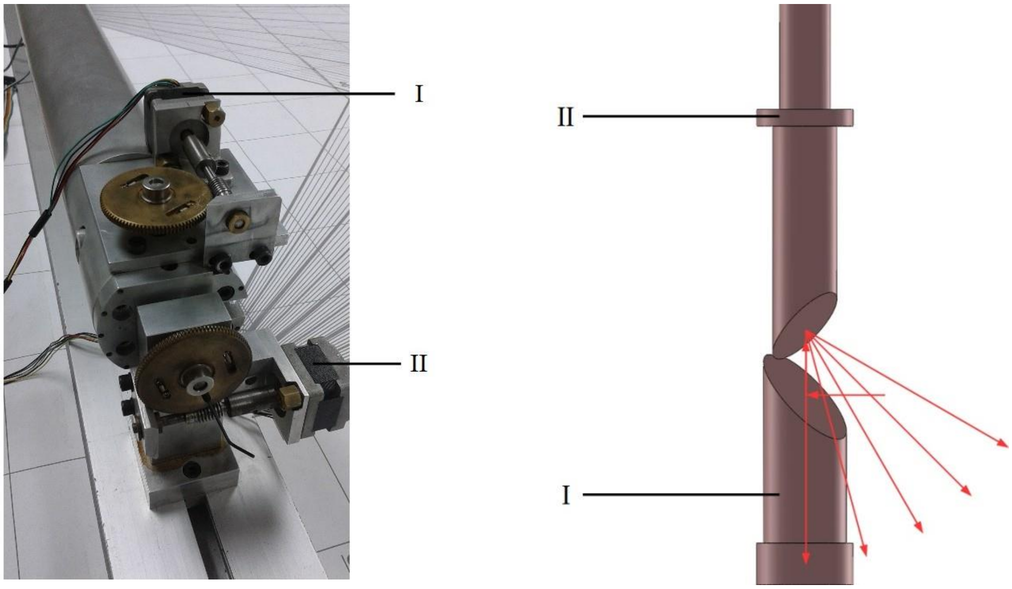

a) System View **b) Schematic View**

Figure 6-2: Positioning Laser (PL) [43]

The stepping motors are driven in "Full Step" mode, where they need 200 steps per complete revolution, which defines the horizontal laser position resolution without transmission:

$$\Delta\varphi_o = \frac{360°}{200} = 1.8° \tag{6-1}$$

The transmission of every stepping motor decreases the angular speed and increases the positioning resolution with a gear ratio of 96:1. By using this transmission, the laser position resolution now is defined:

$$\Delta\varphi_o = \frac{360°}{200 \cdot 96} = 0.01875° \tag{6-2}$$

6.1.2 Scanning Aperture

The reflected laser beam from the examined object is received by the Scanning Aperture (Figure 6-3), which basically consists of a 45° staggered mirror, two biconvex lenses, a zero sensor and a stop sensor. The mirror is rotated by a DC motor and redirects the reflected laser beam from the observed object towards the lenses, which concentrate them for the stop sensor (high speed phototransistor). When the received laser beam is located in the orthogonal plane of the 45° staggered mirror, the stop sensor receives the maximum amplitude of the laser beam and converts it to an electrical pulse. The zero sensor produces a reference signal each full revolution and starts two counters to accumulate pulses. The first counter accumulates pulses from a standard reference f_P between two consecutive zero sensor pulses, which defines the pulse number for $N_{2\pi}$ in each full revolution. The standard reference signal represents a pulse train with fixed period $T_P = \frac{1}{f_P}$ and is generated by a microcontroller.

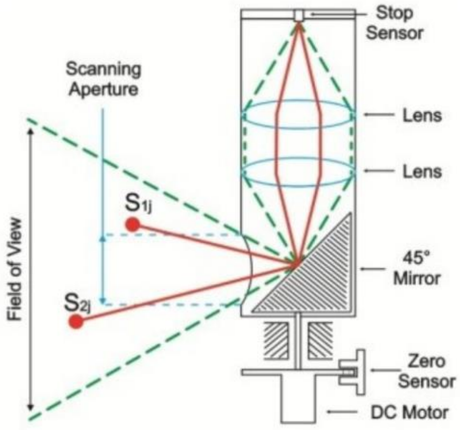

Figure 6-3: Scanning Aperture (SA) [43]

The second counter accumulates pulses of the same standard reference between the zero sensor pulse and the stop sensor pulse, which defines the pulse number for N_A in each revolution. Hence, N_A represents the received beam angle encoded in the pulse number of this variable. The received laser beam angle then is calculated using following equation:

$$\beta = 2\pi \cdot \frac{N_A}{N_{2\pi}} \qquad (6\text{-}3)$$

Figure 6-4 depicts the standard reference signal f_P, the zero sensor signal $f_{2\pi}$, the period for one revolution $T_{2\pi}$, the full revolution pulse number $N_{2\pi}$, the time phase shift T_A and the SA angle pulse number N_A:

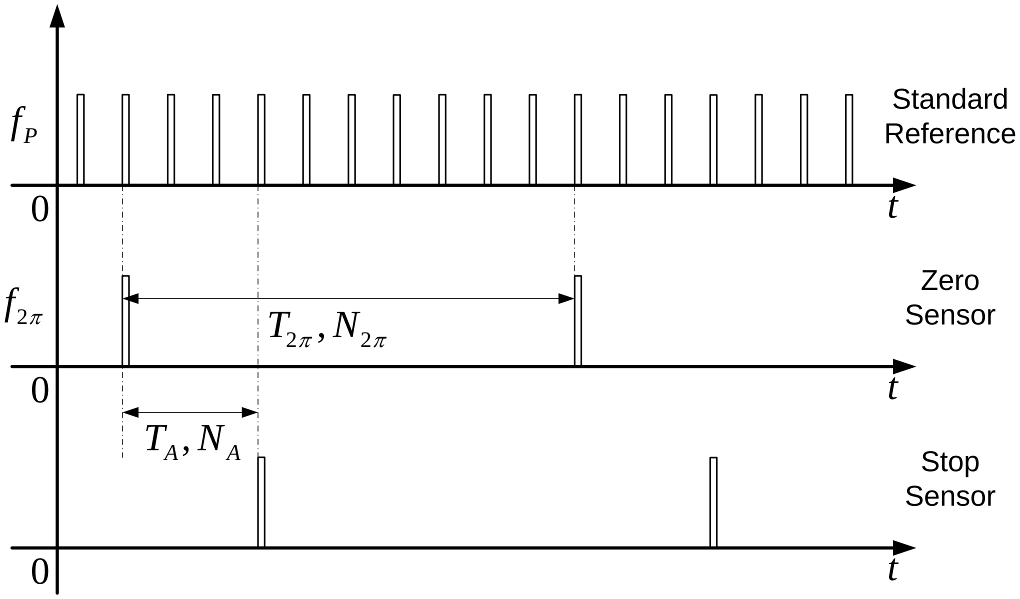

Figure 6-4: Scanning Aperture Signals

6.2 Prototype No.3

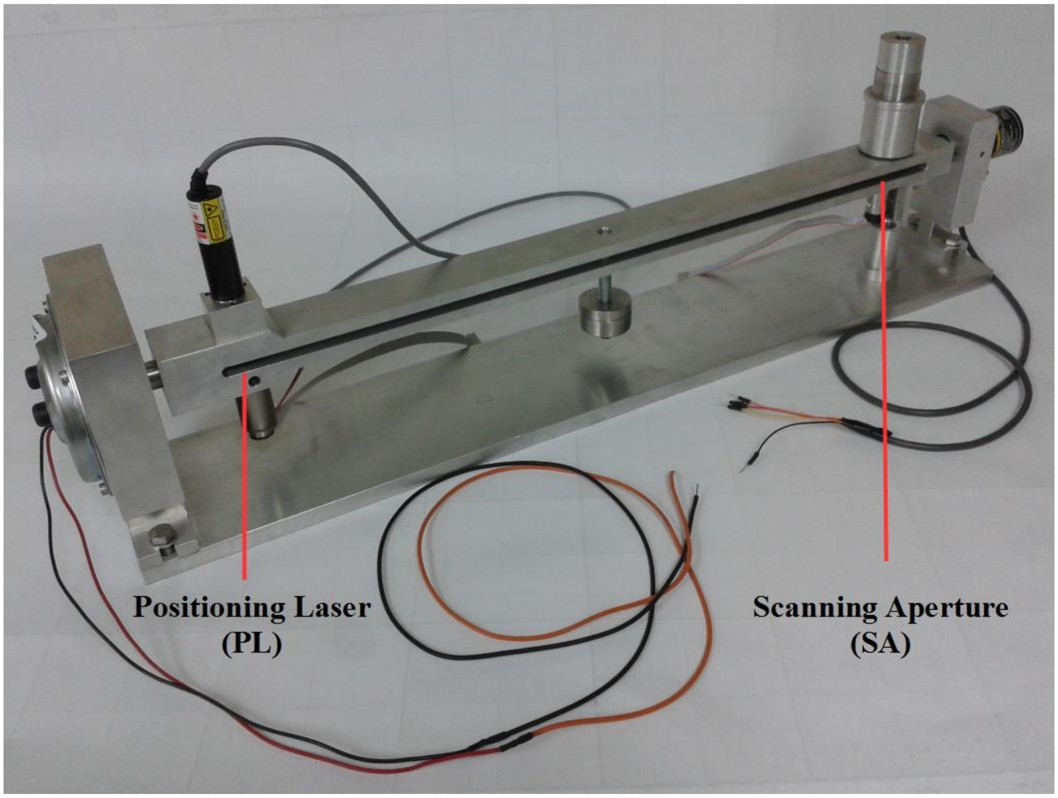

Figure 6-5: Technical Vision System (TVS) No.3

Figure 6-5 depicts the TVS successor prototype No.3, containing the new Positioning Laser (PL) and Scanning Aperture (SA), which comprises the following advantages compared with the TVS prototype No.2:

- Using servomotors instead of stepping motors, to substitute the discrete FOV by a continuous one and thereby elimination of dead zones in the TVS FOV.
- Using servomotors directly without gear, to increase speed and accuracy of the 3D coordinate measurement.
- Minimization of the PL relative positioning error by simplification of mechanical design and optimized control.
- By lowering the TVS mechanical degree of complexity, possible causes of systematic errors are eliminated.
- Opening the possibility for implementation of new scanning algorithms, e.g. variable step scanning methods [45].

6.2.1 Positioning Laser

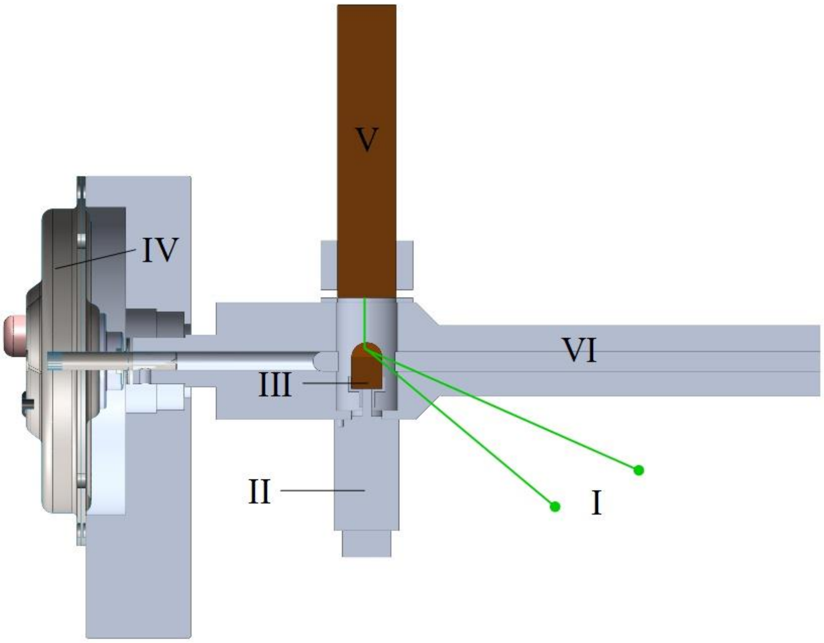

Figure 6-6: Positioning Laser (PL)

The new design of the positioning laser is depicted in Figure 6-6, which shows the optical path of the transmitted laser beam (I), the DC motor Maxon RE-max29 (II), a 45° staggered mirror (III), the pancake motor Printed Motor Works GPM9 (IV), a laser diode module Coherent StingRay-514 (V) and the TVS main rod (VI). Compared to the design of the PL prototype No.2 (Figure 6-2) first it can be seen, that due to elimination of all transmission parts, a high simplification of the positioning laser is achieved. Systematic errors produced by face clearance in every transmission are eliminated and the PL angle γ (Figure 2-1) corresponds directly to the actual angular position φ_o of the DC motor (II).

Also, because the TVS is rotated around his horizontal axis without using a transmission, a motor with high torque and flat dimensions is needed. These two conditions are fulfilled by a pancake motor. Also here, the PL angle η (Figure 2-2) corresponds directly to the actual angular position φ_o of the pancake motor (IV). It must be noted, that now any PL angle η, which not corresponds to the TVS balanced state in the earth gravitational field, has to be controlled in closed-loop configuration, since the advantage of a self-locking worm gear is not used anymore. Since the pancake motor constantly has to generate a holding torque, this can lead to higher energy consumption.

Furthermore, it can be seen that this design requires only one 45° staggered mirror to redirect the laser beam in the TVS field of view, due to the vertical installation of the laser source (V). This decreases the systematic error produced by manufacturing tolerances and non-alignment of the staggered mirror and reduces the overall cost of the optical components. The laser source contains a 10mW laser diode with 514nm wavelength. The system parameters of the DC motor Maxon RE-max29, the pancake motor Printed Motor Works GPM9 and the DC motor Maxon DCX22S are summarized in Table 13-1 (Appendix). The DC motor DCX22S represents the proposed successor model for the currently used DC motor Maxon RE-max29.

6.2.2 Scanning Aperture

The new design of the scanning aperture is depicted in Figure 6-7, which shows the optical path of the received laser beam (I), the DC motor Maxon A-max16 (II), a 45° staggered mirror (III), two biconvex lenses (IV), an optical filter (V) and a high-speed photodiode (VI).

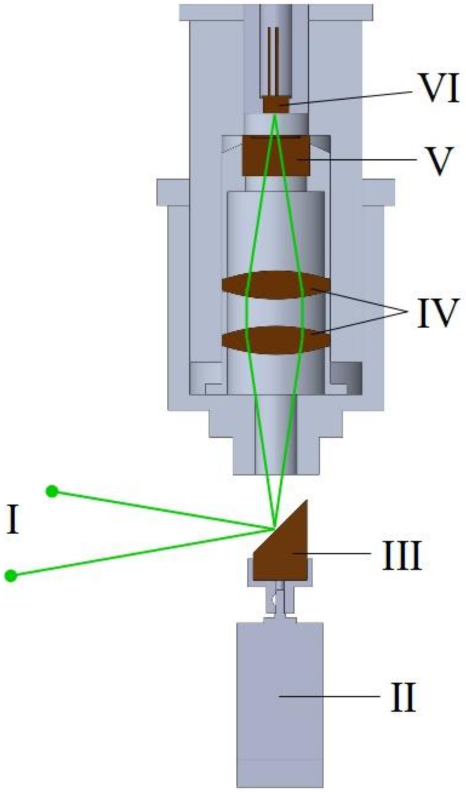

Figure 6-7: Scanning Aperture (SA)

Like the DC motor has an integrated quadrature encoder with index channel, there is no need for the zero sensor anymore. The optical filter thereby has a center wavelength of 515nm, full width-half wavelength of 10nm and a transmission of 45%. The center wavelength of the filter corresponds to the laser diode module wavelength. The photodiode is used with a transimpedance amplifier, to convert the small photocurrent of the diode to a higher voltage, which thereby is measured using the ADC of the microcontroller. The Maxon A-max16 is digitally controlled by a microcontroller (Arduino Uno), which by use of a PI-algorithm controls the actual rotating speed of the 45° mirror. The system parameters of the proposed Maxon A-max16 and the 45° mirror are summarized in Table 13-1 (Appendix).

7 Continuous TVS Design and Functioning Principle

The implementation of servomotors instead of stepping motors in the new TVS prototype No.3 pursues two principal objectives:

1. Dead zone elimination in the TVS FOV and thereby substitution of a discrete FOV with a continuous one.
2. Reducing the TVS PL relative angular error and reducing the PL step response rising time.

By implementing these two objectives in the new prototype No.3, the overall system shall be accelerated and the accuracy of laser positioning be increased. To accomplish these two objectives, it is proposed the use of servomotors, which contains DC motors with encoder and without gear, controlled by a microcontroller (Arduino Uno) in closed-loop configuration, as depicted in Figure 5-1 and novel theoretical formalism to provide its functioning.

7.1 Positioning Laser

By using worm gears in the TVS prototype No.2, a first major disadvantage is detected and defined. The existence of Backlash in every mechanical transmission (Figure 7-1) results always in a positioning error of the TVS positioning laser.

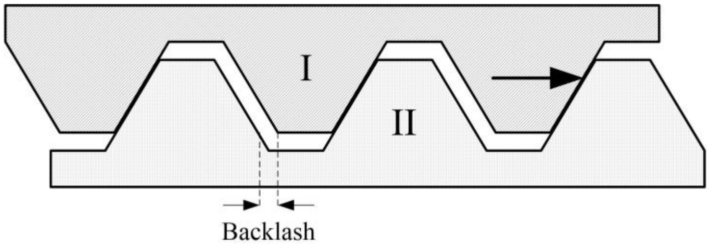

Figure 7-1: Worm gear backlash

When the worm screw (I) turns in one direction, the thread front flank is pressing against one face of the worm wheel (II) thread. Between the worm screw rear flank and the other face of the worm wheel exists a small clearance, which upon reversal of rotation causes a backlash of the worm gear. Thus, the worm gear backlash produces a deadband behavior of the actual angular position of the TVS positioning laser. To eliminate this major disadvantage, for the TVS successor prototype No.3 it is proposed to eliminate every transmission and mount the 45° staggered mirror (III, Figure 6-6) directly on the servomotor shaft (II, Figure 6-6).

A second major disadvantage is detected, when using transmission: High resolution and fast positioning of the TVS PL are two mutually exclusive conditions. This problem limits the dynamic triangulation method whether it is more accurate or fast, but both conditions cannot be complied simultaneously [35]. By avoiding transmissions in the TVS successor prototype No.3, this second major disadvantage is also eliminated.

Another major disadvantage detected for the positioning laser in the TVS prototype No.2 is represented by the use of stepping motors to position the laser. As can be seen in Figure 2-8, stepping motors have a discontinuous behavior, due to their stepwise rotation and thereby the positioning laser can only be positioned in discrete points. Thus, as depicted in Figure 2-5, the TVS FOV is discretized and its resolution depends on the distance of the examined object. Only advantage of this discrete behavior is that the positioning error is zero in these discrete points. Besides, that by using stepping motors the positioning laser can never reach any desired position in the TVS FOV, stepping motors produce oscillations in every step, which increase the step response rising time.

It must be noted, that the positioning resolution of servomotors is limited only by physical constraints. In low-cost servomotors, the breakaway and cogging torque prevent a constant and linear rotation of the motor shaft under low speed. Because of these two moments, a minimum armature voltage must be applied to avoid the motor from stopping, and hence the motor shaft will always be positioned with an error, which represents a residual error not zero. To reduce this positioning error, high-cost servomotors with less breakaway and without cogging torque must be used [35]. Therefore, different suppliers of servomotors were compared and it was given the priority to Maxon Motors for the two reasons of greater choices in motors with different accessories and major availability of products. Maxon Motors are using an ironless winding for their rotors, which do not possess a cogging torque and also use high-quality ball bearings, which reduce the breakaway torque. These motors can be operated constant and linear even at low rotational speeds. Therefore the shaft of these high-cost servomotors can be positioned more accurately and with higher resolution, than the shaft of low-cost servomotors [35].

Therefore, for the positioning laser of the new TVS prototype No.3, high-quality servomotors from Maxon Motor with encoder and without gear shall be used.

7.2 Scanning Aperture

The SA electronic of the TVS prototype No.2 uses the signals defined in Figure 6-4, to determine the SA angle β using equation (6-3). The open-loop control of the DC motor of the scanning aperture results in a non-constant actual angular speed ω_o and thereby in different measurements β_{ij} for the same angles of incidence, which represents the major issue for the SA prototype No.2. The non-constant actual angular speed $\omega_o(t)$ of the DC motor results a zero sensor frequency $f_{2\pi}$ dependence on time:

$$f_{2\pi}(t) = \frac{2\pi}{\omega_o(t)} \tag{7-1}$$

The SA angle error shall be analyzed. Therefore, the instantaneous value of the zero sensor frequency is defined using a mean $\bar{f}_{2\pi}$ and error value $\epsilon_{2\pi}$:

$$f_{2\pi} = \bar{f}_{2\pi} + \epsilon_{2\pi} \tag{7-2}$$

This error value $\epsilon_{2\pi}$ can also be negative and its statistical behavior must be determined experimentally. The standard reference frequency is constant and the pulse number $N_{2\pi}$ is given by:

$$N_{2\pi} = \frac{f_P}{f_{2\pi}} = \frac{f_P}{\bar{f}_{2\pi} + \epsilon_{2\pi}} \tag{7-3}$$

Equation (7-3) shows, how the error value $\epsilon_{2\pi}$ affects the pulse number $N_{2\pi}$. The pulse number N_A is calculated using the time phase shift T_A, which is also time-dependent, and the standard frequency f_P:

$$N_A = f_P \cdot T_A(t) \tag{7-4}$$

Equation (7-3) and (7-4) shows, that due to the non-constant speed of the DC motor, the number of $N_{2\pi}$ and N_A varies every revolution. Inserting both equations in (6-3) results:

$$\beta = 2\pi \cdot f_P \cdot T_A(t) \cdot \frac{\bar{f}_{2\pi} + \epsilon_{2\pi}}{f_P} = 2\pi T_A(t) \cdot \left(\bar{f}_{2\pi} + \epsilon_{2\pi}\right) = 4\pi^2 \cdot \frac{T_A(t)}{\omega_o(t)} \tag{7-5}$$

Equation (7-5) shows, that the SA angle β depends on the time-dependent phase shift $T_A(t)$ and on the non-constant actual angular speed $\omega_o(t)$, which produces different measurement results for a same SA angle. To eliminate this major issue, the new prototype No.3 shall contain a closed-loop speed control for the SA DC motor, to stabilize the DC motor actual angular speed ω_o and to minimize the measurement errors defined by equation (7-5).

8 Algorithm of DC Motor Control for Continuous Positioning

For the new TVS prototypes No.3 the control algorithms for position control of servomotors must be implemented using digital controller. The correct and practically implementation of these algorithms requires considering the following conditions:

1) Equidistant execution of the control algorithm using microcontroller timers

A digital controller has a fixed CPU clock rate though, but a variable program execution time, due to asynchronous events, conditional statements, branches, etc. In order to ensure the condition of an equidistant execution of the control algorithm, microcontroller timers must be used, which represent the sample and hold element $H(s)$ and guarantee an execution of the algorithm using the sampling period T_S.

2) Discretization of input and output values

Digital controller constitutes a Sample and Hold-behavior (S&H), which discretize the time and quantize the amplitude of a continuous time signal $f(t)$. By discretization of input and output variables, an inevitable systematic error is added to the values of these variables. Section 5.2 describes the S&H-element.

3) Normalization of input and output variables

By normalizing the input and output variables of the digital controller the value range is scaled to a range between $[0 - 100\%]$. Normalization is necessary to represent the input and output variables regardless of their physical measuring unit, thus they are made dimensionless. The dimensionless values of the input variables are used for the control algorithm to calculate the manipulated variable, which is related to the range of the output variable then. Thereby, the calculated control variable is returned to the measuring unit of the output variable.

4) Calculations using floating-point or fixed-point numbers

Because of the limited storage of a digital controller, all internal variables must be stored with a limited resolution. The internal variables of a digital controller are stored and calculated either as fixed-point or floating-point values. Both number formats have their own advantages and disadvantages. Floating-point numbers have a higher precision, higher dynamic range and are more general purpose, than fixed-point numbers. Fixed-point numbers, in turn, have advantages in calculation speed and memory requirements, as shown in section 5.2.

5) Resolution of internal variables

The resolution of the internal variables is directly related to the precision they store a given value and depends directly on the number of bits of the used datatype. Hence, an internal variable can store a value more precise, the higher is this number of bits.

6) Clamping of the controller output variable $y(t)$

When calculating the control algorithm, values outside the permitted normal range of the output variables can be arise. Because of real physical constrains, like maximum DC motor armature voltage u_A, the controller output variable $y(t)$ must be clamped to the range of $[0 - 100\%]$. This guarantees that the output variable does not exceed its technically maximum possible values.

Present chapter describes in detail the practical implementation of the position control algorithm for the DC motors, used by the new TVS prototype No.3.

8.1 Actual Angular Position Measuring

Like it is used the Maxon Motor RE-max29 with encoder MR Type ML, without using a transmission, the actual counted pulses ρ_o (counts) from the encoder in quadcount mode represent directly the actual angular position φ_o (degree) and can be converted vice versa by relation:

$$\frac{\varphi_o}{360°} = \frac{\rho_o}{4000} \tag{8-1}$$

An analysis of the measurement error ϵ for the actual angular position is given in section 8.2.2. This section gives a measurement error of $\epsilon \leq 0.09°$, which represents a major improvement, when compared to the horizontal laser position resolution without transmission of the TVS prototype No.2 (6-1).

8.2 Closed-Loop Algorithm

In order to realize the proposed position control practically, the Maxon Motor RE-max29 with encoder is connected with a microcontroller (Arduino Uno) and L298N driver module in closed-loop (CL), depicted in Figure 8-1. The position controller is realized by the Arduino, which also contains the comparator.

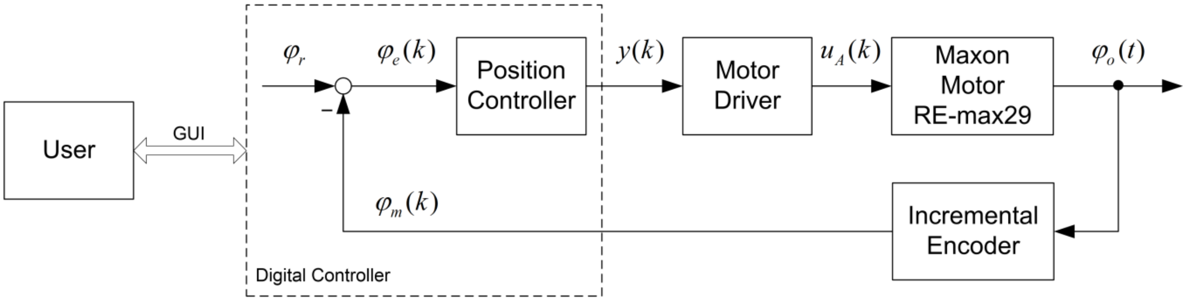

Figure 8-1: Closed-loop position control

Thereby, φ_r represents the reference angular position from the user, $\varphi_e(k)$ the absolute angular error, $y(k)$ the controller output variable, $u_A(k)$ the motor armature voltage generated by the motor driver, $\varphi_o(k)$ the actual angular position and $\varphi_m(k)$ the measured angular position of the motor shaft. Thereby, k represents discrete time points of the continuous time t. The positioning algorithm is part of the position controller block.

8.2.1 Controller Output Variable

The absolute angular error φ_e is calculated by the difference between the reference angular position φ_r and the measured angular position φ_m:

$$\varphi_e = \varphi_r - \varphi_m \tag{8-2}$$

To normalize this absolute error to percentage, this value is related to the reference angular position φ_r and thereby converted to the relative angular error φ_e':

$$\varphi_e' = 100 \cdot \frac{\varphi_r - \varphi_m}{\varphi_r} \tag{8-3}$$

Like the determination of the actual angular position φ_o has an integral characteristic (accumulating the encoder pulses), only a P-controller (K_R) is needed to control the actual angular position of the motor shaft (Figure 4-4). Thus, the controller output variable $y(t)$ is calculated by:

$$y = K_R \cdot 100 \cdot \frac{\varphi_r - \varphi_m}{\varphi_r} = y_{\varphi_r} \tag{8-4}$$

By multiplying the internal variables φ_e' and K_R (represented as float-numbers) with a certain ten-power and storing them as integer-numbers, the significant figures of the stored value is defined. It must be noted that the significant digits of both internal variable φ_e' and K_R are added up by equation (8-4) and therefore may not exceed the maximal possible digits of precision, defined in Table 5-2 (10 digits).

To improve the step response of the controlled Maxon Motor RE-max29, the absolute angular error φ_e can be related to the maximum positioning angle of $360°$:

$$y = K_R \cdot 100 \cdot \frac{\varphi_r - \varphi_m}{360°} = y_{360} \tag{8-5}$$

Thus, the initial armature voltage / motor speed u_A will be higher, the greater is the initial absolute angular error $\varphi_e(0)$. This prevents unstable oscillatory step responses, when the initial absolute error is too small. For both equations (8-4) and (8-5) apply the conditions, that $K_R > 0$ and $\varphi_r \geq \varphi_m$. Both controller output variables are considered as functions of the measured angular position φ_m, that is $y_{\varphi_r} = y_{360} = f(\varphi_m)$. Because of real physical constrains, like maximum motor armature voltage u_A, the controller output variable must be clamped to the range of $[0 - 100\%]$:

$$y = \max(0, \min(y, 100)) \tag{8-6}$$

The analyze the influence of the parameters K_R and φ_r to the growth of the controller output functions $y_{\varphi_r} = f(\varphi_m)$ and $y_{360} = f(\varphi_m)$, the zeros, the slope, the intersection with ordinate axis and the intersection with the 100%-line shall be calculated. The zeros are calculated by:

$$y_{\varphi_r} = K_R \cdot 100 \cdot \frac{\varphi_r - \varphi_m}{\varphi_r} = 0 \qquad y_{360} = K_R \cdot 100 \cdot \frac{\varphi_r - \varphi_m}{360°} = 0 \tag{8-7}$$

Both of these functions possess the same zero:

$$\varphi_{m,0} = \varphi_r \tag{8-8}$$

The slope results by differentiation:

$$\frac{dy_{\varphi_r}}{d\varphi_m} = -\frac{100K_P}{\varphi_r} \qquad \frac{dy_{360}}{d\varphi_m} = -\frac{100K_P}{360°} \tag{8-9}$$

That means, that the slope of the y_{φ_r} function depends on K_R and φ_r and the slope of the y_{360} function only on K_R. The intersection with the ordinate axis is calculated by:

$$y_{\varphi_r}(0) = 100K_R \qquad y_{360}(0) = \frac{100}{360°} \cdot K_R\varphi_r \tag{8-10}$$

The intersection with the 100%-line is calculated by:

$$\begin{aligned} y_{\varphi_r} &= K_R \cdot 100 \cdot \frac{\varphi_r - \varphi_m}{\varphi_r} = 100 & y_{360} &= K_R \cdot 100 \cdot \frac{\varphi_r - \varphi_m}{360°} = 100 \\ \varphi_{m,100} &= \varphi_r \left[\frac{K_R - 1}{K_R}\right] & \varphi_{m,100} &= \varphi_r - \frac{360°}{K_R} \end{aligned} \tag{8-11}$$

In order that $\varphi_{m,100} > 0$ and thereby $y_{\varphi_r}(0) > 100$ or $y_{360}(0) > 100$, for the first function must $K_R > 1$ and for the second function must $K_R > \frac{360°}{\varphi_r}$.

Figure 8-2 shows a graphical sketch of both controller output functions $y_{\varphi_r} = f(\varphi_m)$ and $y_{360} = f(\varphi_m)$. For both functions it shows two cases, when $y(0) > 100$ and when $y(0) < 100$. Both controller output variables are not greater than 100%, because they are clamped to the range of $[0 - 100\%]$ (8-6). Both functions have the same zero (8-8), different slopes (8-9), different intersection with the ordinate axis (8-10) and different intersection with the 100%-line.

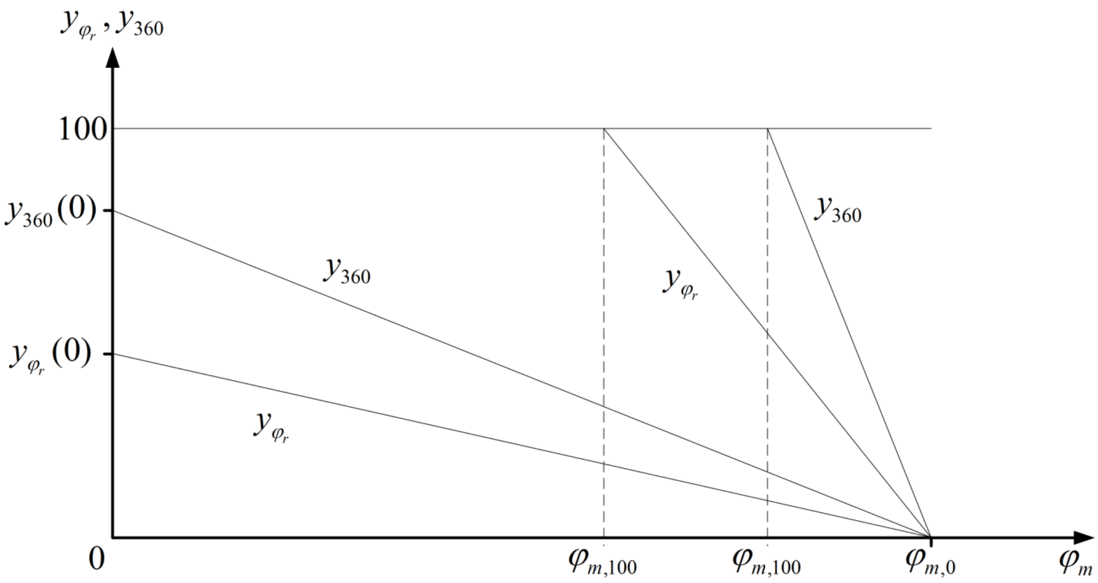

Figure 8-2: Graph of controller output functions

8.2.2 Error analysis

When calculating the controller output variables, an absolute measurement error ϵ is considered, which is defined by the difference between the actual angular position φ_o and the measured angular position φ_m:

$$\epsilon = \varphi_o - \varphi_m \tag{8-12}$$

This error originates from the actual angular position measuring by counting the encoder output pulses, represented by ρ_o (counts). Hereby exists an uncertainty of one pulse $\Delta = 1$, due to the discrete values of the counted output pulses, which are represented by integer numbers:

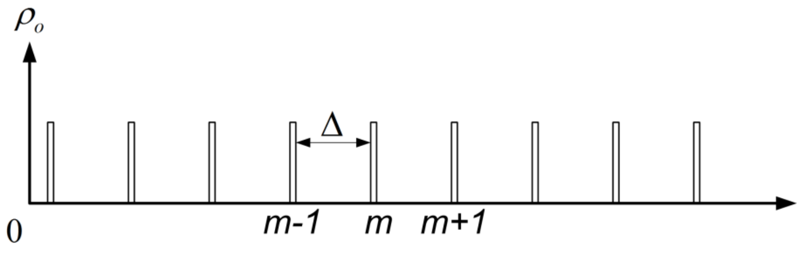

Figure 8-3: Output pulses of incremental encoder

Using equation (8-1) this one pulse represents 0.09° and thus, the error ϵ is limited by the following range:

$$0 \leq \epsilon \leq 0.09° \tag{8-13}$$

To define the influence of this error to the controller output variables, equation (8-12) is inserted in the controller output functions (8-4) and (8-5):

$$y_{\varphi_r} = K_R \cdot 100 \cdot \frac{\varphi_r - \varphi_m}{\varphi_r} = 100K_R \left[\frac{\varphi_r - \varphi_o}{\varphi_r} + \frac{\epsilon}{\varphi_r}\right] = 100K_R\left[y'_{\varphi_r} + \epsilon'_{\varphi_r}\right] \tag{8-14}$$

$$y_{360} = K_R \cdot 100 \cdot \frac{\varphi_r - \varphi_m}{360°} = 100K_R \left[\frac{\varphi_r - \varphi_o}{360°} + \frac{\epsilon}{360°}\right] = 100K_R[y'_{360} + \epsilon'_{360}] \tag{8-15}$$

Thereby y'_{φ_r} and y'_{360} represent the relative controller output variables and ϵ'_{φ_r} and ϵ'_{360} the relative measurement errors of the controller output functions. It can be seen, that ϵ'_{φ_r} depends of the reference angular position φ_r, while ϵ'_{360} has a fixed value of $\frac{1}{4000}$. Because of (8-14) and (8-15), the relative measurement error ϵ' is producing an armature error voltage, independent if the relative controller output variable y' is zero or not. This means, that the amplification factor K_R must be chosen so small, that this error voltage is small enough so that the static friction force prevents rotation of the DC motor.

Equations (8-14) and (8-15) also define the range of the controller output functions y_{φ_r} and y_{360}. The resolution of the internal variables K_R, y', ϵ' and the controller output variable y is defined by the used datatype for storing.

8.3 Open-Loop Algorithm

The open-loop (OL) position control, depicted in Figure 8-4, is derived from the closed-loop model (Figure 8-1). The measured angular position of the motor shaft $\varphi_m(k)$ from the incremental encoder is not fed back to the controller and therefore is no need for a comparator anymore:

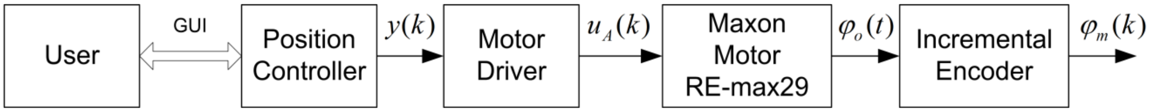

Figure 8-4: Open-loop position control

Again, k represents discrete time points of the continuous time t. Because of the no-feedback characteristic of the open-loop position control, two control algorithms 1 and 2 are developed, implemented and tested.

8.3.1 Algorithm 1

Algorithm 1 is based on a theoretical approach, using the DC motor physical constants, which define the transition of motor shaft positioning and final states according to the supplied voltage and current:

- Speed constant K_v describes the revolutions per minute per volt $\frac{rpm}{V}$.
- Mechanical time constant T_M represents the time for the motor to reach 63.2% of its nominal angular speed.

For the open-loop position controlled Maxon Motor RE-max29 the speed constant is $K_v = 56.8\ \frac{rpm}{V}$ and the mechanical time constant $T_M = 4.35\ ms.$ Using the speed constant to calculate degrees per volt seconds gives:

$$56.8\ \frac{rpm}{V} \cdot \frac{360°}{60s} = 340.8 \frac{°}{Vs} \tag{8-16}$$

Calculating the amount of time the motor uses to rotate 1°, when applying an armature voltage $u_A = 6V$, gives:

$$\frac{1000}{340.8\ \frac{°}{Vs} \cdot 6V} = 0.489 \frac{ms}{°} \tag{8-17}$$

Equation (8-17) shows theoretical, that when applying the armature voltage $u_A = 6V$ for the time of $\approx 0.5ms$, the DC motor shaft will position with 1° angular position. When executing the OL algorithm, this amount of time is guaranteed by use of microcontroller timer with a defined sampling rate f_S and a defined constant PWM duty cycle d_{const}. That is, d_{const} defines the average armature voltage $\bar{u}_A$ applied to the DC motor and T_S the duration of this $\bar{u}_A$.

8.3.2 Algorithm 2

The Algorithm 2 represents an empirical algorithm, to optimize the positioning task using a triangle profile of the DC motor armature voltage u_A. The averaged armature voltage $\bar{u}_A$ produced by the PWM signal is increased and decreased between 0 and 2V. Thereby, the variable PWM duty cycle d_{var} is increased lineal from 0% - 17% and afterwards decreased lineal to 0%. Thus, the DC motor shaft is driven to the final angular position $\varphi_\infty = \varphi_o(t \to \infty)$, which corresponds to a feed forward control.

The reference angle φ_r from the user is divided by an empirical constant K_{emp}, to get the maximum iteration number of the algorithm at given voltage:

$$i_{max} = \frac{\varphi_r}{K_{emp}} \qquad (8\text{-}18)$$

To calculate the increasing variable duty cycle d_{var}, following equation is applied, using a resolution of PWM signal K_{PWM}:

$$d_{var} = \frac{i}{i_{max}} \cdot K_{PWM} \qquad (8\text{-}19)$$

, and vice versa for the decreasing variable duty cycle d_{var}, following equation is applied:

$$d_{var} = \frac{i_{max} - i}{i_{max}} \cdot K_{PWM} \qquad (8\text{-}20)$$

9 Experimentation Realization and Results

Experimentations have been realized to control the DC motor actual angular position φ_o of Maxon Motor RE-max29, the experimental setup is depicted in Figure 9-1:

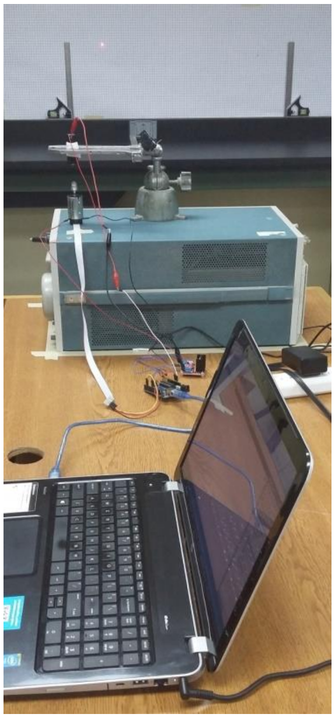

Figure 9-1: Experimental Setup

Present chapter describes in detail the experimental conditions and realization of the DC motor position control in closed- and open-loop configuration. Experimental results get summarized and compared in tables.

9.1 Closed-Loop Algorithm

The realized experimentations to control the DC motor actual angular position φ_o uses the following experimental parameters, measured values and constants (Table 9-1).

Table 9-1: Experimental parameters, constants and measured values

	Symbol	Description	Unit / Value
Parameters	φ_r	Reference angular position	deg
	K_R	Amplification factor of positioning algorithm	-
Constants	ppr	Pulses per revolution of encoder (quadcount)	4000
	f_{PWM}	Frequency of PWM signal	980 Hz 1000 Hz
	K_{ref}	Reference value for relative position error calculation	φ_r ppr
Measured values	φ_m	Measured angular position	deg
	t_{rise}	Step response rising time	ms
	φ'_e	Relative angular error	%
	$\bar{t}_{rise}$	Step response rising time average	ms
	$\bar{\varphi}'_e$	Relative angular error average	%

The reference angular position φ_r represents the user command and input of the closed-loop position control for the microcontroller. K_R represents the amplification factor of the positioning algorithm used in equation (8-4) and (8-5). The maximal resolution used from the Maxon Motor incremental encoder MR Type ML is constant with $ppr = 4000$. The PWM frequency f_{PWM} depends, if using the Arduino function analogwrite() with a fixed PWM frequency of 980Hz or the microcontroller Timer1 directly. The reference value K_{ref} defines, whether φ_r or ppr is used to calculate the relative angular error φ'_e, using the known equation from (8-3):

$$\varphi'_e = 100 \cdot \frac{\varphi_r - \varphi_m}{K_{ref}} \tag{9-1}$$

The measured angular position φ_m represents the measured motor shaft angle after application of the positioning algorithm. t_{rise} represents the measured step response rising time for this. Using 5 measurements, the average for the relative angular error and step response rising time is computed and represented by $\bar{\varphi}_e'$ and $\bar{t}_{rise}$. So, 6 experimental factors (Table 9-2) and arrangements of these factors in 15 tests (Table 9-3) are defined, to analyze the influence of every experimental factor.

Table 9-2: Defined experimental factors

Factor	Name	Description	1	2	3
A	-	Positioning algorithm data type	Float	Integer	-
B	-	Timer1 Mode of Operation	CTC	Fast PWM	-
C	f_S	Sampling rate of positioning algorithm	100Hz	200Hz	500Hz
D	K_{ref}	Reference value for relative position error calculation	φ_r	ppr	-
E	$digit$	Resolution of Integer positioning algorithm	-	3 digits (1000)	-
F	K_{PWM}	Resolution of PWM signal	255	16000	-

Factor B and F depends each other, since no PWM signal is produced, when using Timer1 in CTC mode. Instead it is used the Arduino function analogwrite(), to generate the PWM signal, which has a duty cycle resolution of 255. When using Timer1 in Fast PWM mode, the PWM frequency is defined by the TOP value of (5-7), which defines the overflow frequency of Timer1. With $f_{CPU} = 16MHz$ microcontroller clock speed and $f_{PWM} = 1KHz$ PWM frequency, equation (5-7) gives a duty cycle resolution of:

$$TOP = \frac{16MHz}{1kHz} = 16000 \tag{9-2}$$

With the used PWM frequency of $f_{PWM} = 1KHz$ and the used duty cycle resolution of $TOP = 16000$, a good and practicable balance between these two mutual excluding conditions described by (5-7) is found.

Varying the parameters K_R and φ_r from Table 9-1, 5 measurements for the relative angular error average $\bar{\varphi}_e'$ and the step response rising time average $\bar{t}_{rise}$ are recorded (using experimental setup depicted in Figure 9-1) and collected in Table 13-2 and Table 13-3 (Appendix). For every test, two different amplification factors K_R of the used positioning algorithm (8-4) and (8-5) are chosen, to measure the different effect for the step response of the controlled Maxon Motor REmax-29 and three different reference angular positions of 1°, 5° and 90°, to measure the step response using a small, middle and high angular position.

Table 9-3: Arrangements of experimental factors (Taguchi Method)

Test	A	B	C	D	E	F
1	1	1	1	1	1	1
2	1	1	2	1	1	1
3	1	1	1	2	1	1
4	1	1	2	2	1	1
5	2	1	1	1	1	1
6	2	1	2	1	1	1
7	2	1	1	2	1	1
8	2	1	2	2	1	1
9	2	1	1	1	2	1
10	2	1	2	1	2	1
11	2	1	1	2	2	1
12	2	1	2	2	2	1
13	2	2	1	2	2	2
14	2	2	2	2	2	2
15	2	2	3	2	2	2

All the variety of factors combination (Table 9-3) in experimental results (presented in Appendix, Table 13-2and Table 13-3) shows the adequate stability of the new proposed positioning system in the most probable situations of real system use.

9.2 Open-Loop Algorithm

9.2.1 Algorithm 1

Table 9-4: Experimental factors for algorithm 1

Factor	Name	Description	1	2
A	f_S	Sampling rate of positioning algorithm	1kHz	2kHz
B	d_{const}	PWM duty cycle	50%	43%

Experimentations have been realized to observe the effectiveness of an algorithm that follows the theoretical concept, modifying the experimental factors defined in Table 9-4. The parameters varied in the tests are the sampling rate of positioning algorithm, to compare the difference using faster algorithm's iterations and the PWM duty cycle (50% represents $0 - 6V$ and 43% represents $0 - 5.16V$), to observe if there is a variation in the algorithm's behavior using a lower motor armature voltage (u_A).

The tests are performed with 4 different reference angles (φ_r) and 10 samples for each angle, as shown in Table 9-5:

Table 9-5: Arrangements for algorithm 1

Test	A	B
1	1	1
2	2	1
3	1	2
4	2	2

For comparative purpose the relative angular error average ($\bar{\varphi}'_e$) with 10 samples is used, the obtained results are presented in Figure 9-2:

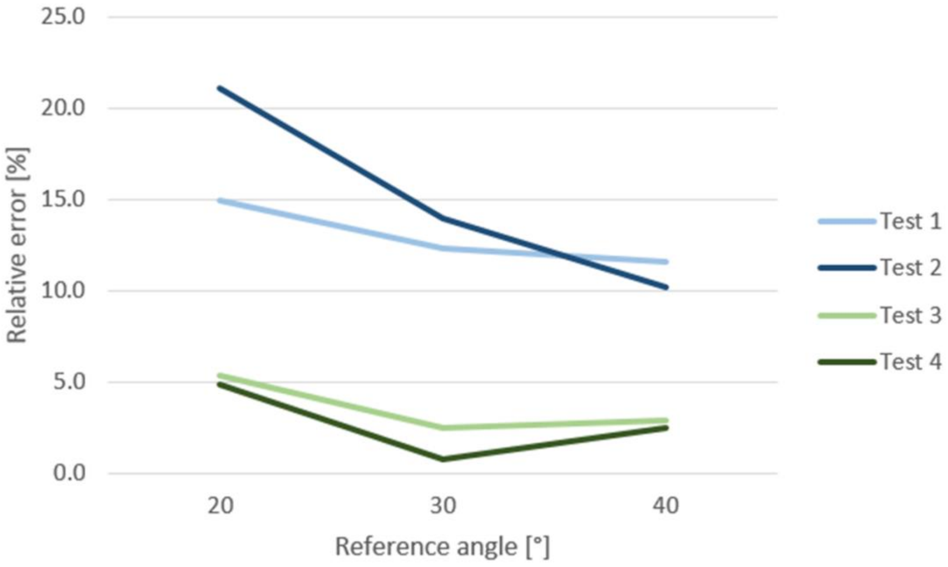

Figure 9-2: Relative angular error average for algorithm 1

Generally it can be seen, that Test 3 and 4, which are using a motor armature voltage $u_A = 5.16V$, contain a lower relative angular error average, than Test 1 and 2. In the first two tests, the relative error average remains above 10%, whereas that in the last two tests the relative error average keeps under 5%.

9.2.2 Algorithm 2

Experimentations have been realized to observe the empirical positioning algorithm behavior varying experimental factors, defined in Table 9-6:

Table 9-6: Experimental factors for algorithm 2

Factor	Name	Description	1	2	3	4	5
A	f_S	Sampling rate of positioning algorithm	1kHz	2kHz	3kHz	5kHz	10kHz
B	d_{var}	Variable PWM duty cycle	16.6%	50%	-	-	-

Two different armature voltage ranges are applied (16% represents $0 - 2V$ and 50% represents $0 - 6V$) and 5 sampling rates of positioning algorithm for 4 different reference angles and 20 samples for each angle. That gives a total of 80 samples for each test. The arrangements of the algorithm 2 experimental factors are shown in Table 9-7:

Table 9-7: Arrangements for algorithm 2

Test	A	B
1	1	1
2	1	2
3	2	1
4	2	2
5	3	1
6	4	1
7	5	1

Statistical calculations are applied for the results, receiving the Mean Absolute Error (MAE) and the Standard Deviation (SD), which represent accuracy and precision of the final angular position φ_∞ respectively. The MAE indicates the absolute angular error average $\bar{\varphi}_e$ and the SD indicates the deviation of the measured values from this average value.

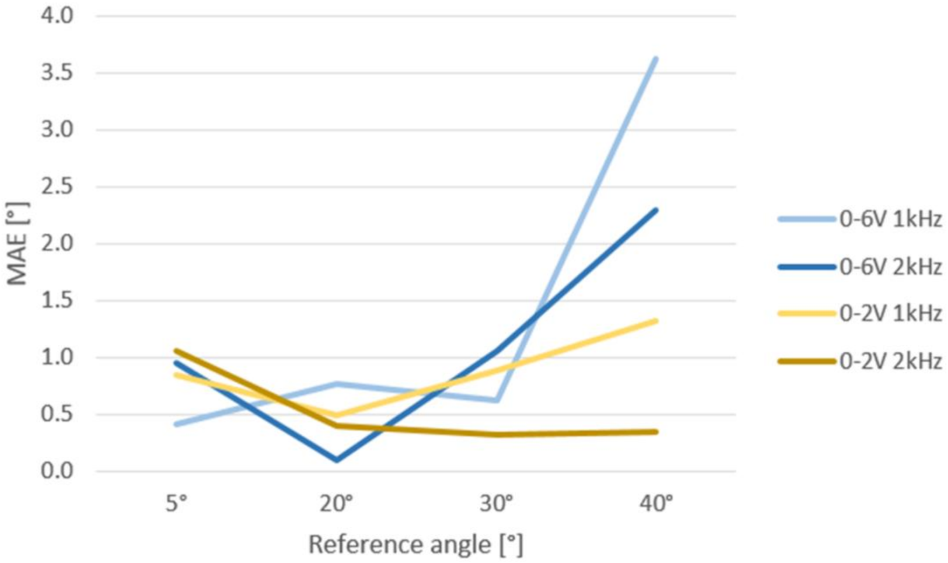

Figure 9-3: MAE for algorithm 2 for different armature voltages

Figure 9-3 compares the MAE for Tests 1, 2, 3 and 4. It can be seen from Figure 9-3, that using a lower motor armature voltage u_A, the algorithm's accuracy is improved, keeping the MAE below 1.5°, while using a higher voltage results in a MAE above 2.0°. Test 3 is determined having the lowest MAE for different reference angular positions φ_r.

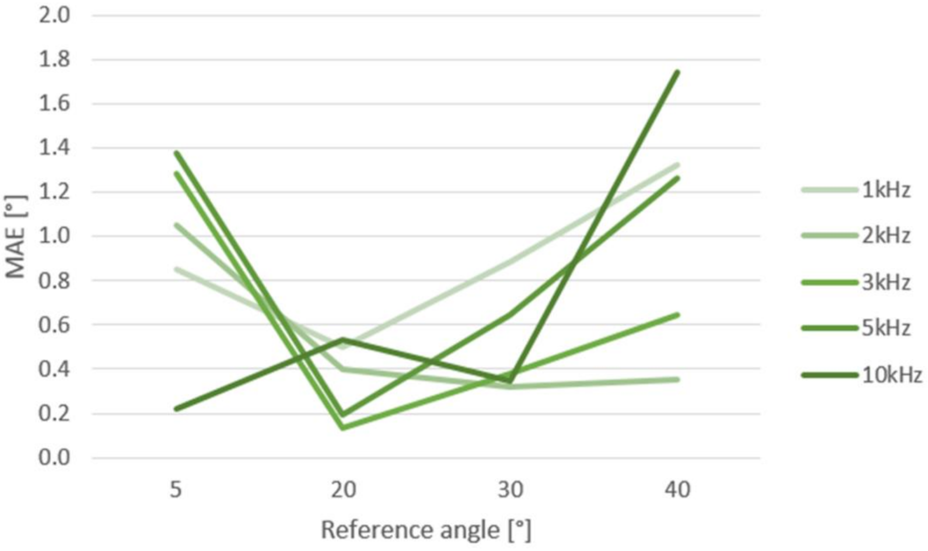

Figure 9-4: MAE for algorithm 2 for different sampling rates

Test 1, 3, 5, 6 and 7 depicted in Figure 9-4, are performed to analyze, if the MAE continues to decrease as the sampling rate f_S increases, maintaining the armature voltage range $u_A = 0 - 2V$.

The best result is still represented by Test 3, when using $2kHz$, producing less variation in measured data and maintaining $MAE < 1°$ for different reference angles.

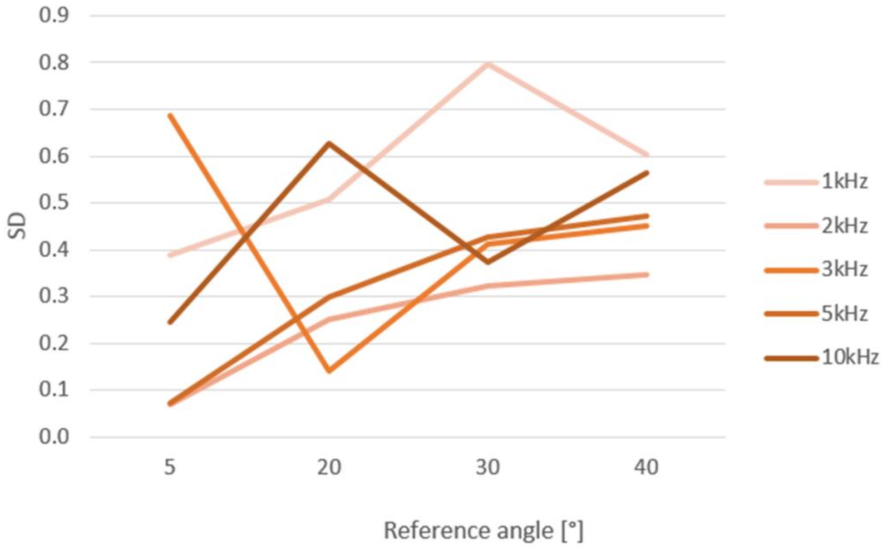

Figure 9-5: SD for algorithm 2 for different sampling rates

Figure 9-5 shows the standard deviation for the measured data. It can be seen that the sampling rate for positioning algorithm $f_S = 2kHz$ results in the least variation, resulting a SD $\sigma < 0.4$.

10 Experimentation Analysis

10.1 Closed-Loop Algorithm

First it can be seen from Table 13-2 and Table 13-3, that there exist tests (marked with red), which could not be executed due to an unstable step response of the DC motor, that is highly motor shaft oscillations around the reference angular position φ_r or increasing the measured angular position φ_m until infinity. It is noted that this unstable step response only appears for Test 1, 2, 5, 6, 9 and 10, where the experimental factor D is on level 1 and always appears in these tests for $\varphi_r = 1°$. By using the reference value for relative position error calculation $K_{ref} = \varphi_r$ equation (8-14) shows, that the relative controller output variable y'_{φ_r} not depend of the reference angular φ_r and so, at the beginning of the motor shaft positioning is always present a relative controller output variable of $y'_{\varphi_r} = 1.0$, which leads to the same acceleration of the motor shaft, regardless of the reference position φ_r. However, the acceleration of the motor shaft should be reduced, the smaller is the absolute angular error φ_e, which leads to equation (8-15), where the pulses per revolution of encoder ppr is used as reference value for relative position error calculation. Thus, the relative controller output variable y'_{360} now depends of the reference angular φ_r and a stable step response of the DC motor can be seen in tests where the experimental factor $D = 2$; that is Test 3, 4, 7, 8, 11 - 15.

To analyze the conclusions made by condition 4) of the positioning algorithm, the floating-point algorithm is converted to a fixed-point algorithm, maintaining other conditions identical. Thereby Test 1 - 4 contains the positioning algorithm using the float datatype and Test 5 - 15 the positioning algorithm using the integer datatype. Especially Test 5 - 8 contains the same experiment factors, as Test 1 - 4. Since in Test 3, 4, 7 and 8 the relative angular error φ'_e depends of the reference angular φ_r ($D = 2$) and this reference angular $\varphi_r < 360°$, an amplification factor of positioning algorithm $K_R > 1$ and clamping the output to 100% is chosen, to analyze the effect. Test 3 and 7 use the same sampling rate $f_S = 100Hz$ and Test 4 and 8 use the same sampling rate $f_S = 200Hz$. Between Test

3, 7 and Test 4, 8, the relative angular error average $\bar{\varphi}_e'$ remains approximately the same, what confirms the functionality and equality of the positioning algorithm using integer datatypes. Here, a relative angular error average $\bar{\varphi}_e' = 100\%$ means that the motor shaft was not moving. Hence, the step response time average was defined with 0s.

A significant improvement of the relative angular error average $\bar{\varphi}_e'$ and the step response rising time average $\bar{t}_{rise}$ can be observed for Test 11 – 15, where a fixed-point algorithm ($A = 2$), a reference value for relative positioning error calculation $K_{ref} = ppr$ ($D = 2$) and a resolution of the integer positioning algorithm with 3 digits ($E = 2$) is used. Especially an improvement can be noted when using the PWM signal with high resolution ($F = 2$), a high sampling rate of positioning algorithm $f_S = 500Hz$ ($C = 3$) and a high amplification factor $K_R = 500$. The best experimental results are given by Test 15 and are marked with green. Acceptable test results are marked with yellow and failing test results with red.

10.2 Open-Loop Algorithm

10.2.1 Algorithm 1

Figure 9-4 shows that all tests performed with $\varphi_r = 5°$ presents irregular results and significant relative errors, due to small reference angular positions φ_r, which implies small positioning times and friction forces acting in opposition to the motor shaft revolution.

Test 3 and 4, with lower motor armature voltage (Factor B = 2), present a relative angular error average $\bar{\varphi}_e' < 6\%$, while Test 1 and 2 contain a relative angular error average $\bar{\varphi}_e' > 10\%$. Therefore, using a lower motor armature voltage, improves the positioning accuracy.

The sampling rate of positioning algorithm f_S is doubled in Test 2 and 4 (Factor A = 2), thereby the microcontroller timer count is changed from 16,000 to 8,000. As the sampling rate f_S and the PWM resolution K_{PWM} are synchronized with the same microcontroller timer, the K_{PWM} from equation (8-19) must be reduced in the same proportion to keep the same PWM duty cycle.

10.2.2 Algorithm 2

Analyzing algorithm 2, first it can be seen, that positioning is improved and the statistical results lead to the conclusion, that MAE and SD are better than for algorithm 1.

During the tests, experimental factors like position algorithm sampling rate and motor armature voltage are varied to select the best algorithm configuration to achieve a good position result. It can be seen in Test 2 and 4 (blue) and Test 1 and 3 (yellow) in Figure 9-3, that using a higher voltage in the algorithm, increases the absolute error for greater reference angular positions. A better result is obtained with a armature voltage range $u_A = 0 - 2V$, which represents $0 - 16.6\%$ of PWM duty cycle. That is, using a lower motor armature voltage improves positioning accuracy also for algorithm 2.

The MAE is maintained less than $1°$ using an algorithm sampling rate $f_S = 2Khz$. Setting the $f_P = 1, 3, 5$ or $10kHz$ results in greater absolute errors, the MAE is more than 1° for these frequencies.

Considering the positioning algorithm is calibrated for $\varphi_r = 20°$. The experimentation results accuracy decreases as the reference angular position is different from $20°$. The absolute error increases proportionally to the sampling rate of positioning algorithm. As it can be seen from the standard deviation in Figure 9-5, using $2kHz$ generates a lower profile in standard deviation and a more constant result for different reference angles. Therefore, accuracy and precision are improved using $2kHz$ sampling rate of positioning algorithm.

Both constants K_{emp} and K_{PWM} from (8-18) and (8-19) are empirically defined for best results of DC motor shaft positioning. Using the best values according the experiments realized in section 9.2.2, which correspond to $f_P = 2kHz$ and $u_A = 0 - 2V$, these constants are set to $K_{emp} = 3.7$ and $K_{PWM} = 2666$.

10.2.3 Algorithm Comparison

Because of motor mechanical and electrical limitations, the open-loop algorithm presents problems when positioning the motor shaft with small angles. The inherent and not negligible breakaway torque omits a linear and constant movement under low speeds of the motor shaft. Because of the inherent rotor inertia, time is required to accelerate and decelerate the rotor and thereby position with small angles.

Recalling, that the Maxon RE-max29 mechanical time constant $T_M = 4.35\,ms$, where the motor shaft is accelerating to 63.2% of its final speed. Considering the approximation that the motor needs T_M to reach the final speed and thereby work at constant speed. The motor moves maximal 1° in $0.489\,ms$ (8-17) using constant speed, thereby the open-loop algorithm is not working properly, when position the motor shaft with less than $\varphi_r = 8.89°$:

$$\frac{4.35\,ms}{0.489\,\frac{ms}{deg}} = 8.89° \qquad (\ 10\text{-}1\ )$$

Concluding, the open-loop algorithm is working properly only after the motor has reached its final speed, positioning angles of 8.89° or less will present insufficient positioning results.

As mentioned above, the empirical algorithm (algorithm 2) presents better results than the theoretical algorithm (algorithm 1), with relative angular error average $\bar{\varphi}_e' < 2.1\%$. The problem of impossibility to position small angles is still present, considering the armature voltage u_A is less in algorithm 2 than in algorithm 1, positioning small angles results in greater relative error averages in algorithm 1, shown in Table 10-1:

Table 10-1: Algorithms relative error average comparison

φ_r	Algorithm 1	Algorithm 2
$5°$	20.76	28.23
$20°$	4.86	2.00
$30°$	0.81	1.07
$40°$	2.50	0.88

11 Conclusions

Present work introduces a novel theoretical method for continuous laser scanning of a Technical Vision System (TVS), based on closed-loop Direct-Current Motor (DC Motor) control using digital controller. This TVS, researched and further developed in this work, represents a laser scanning system, which by using the Dynamic Triangulation measurement method determines 3D coordinates of any examined object. In order to accomplish this theoretical method for continuous scanning, in the present work were provided:

1. The use of a novel physical principle of laser beam propulsion with the aim to achieve the possibility to position the laser beam in any 3D point, to displace this beam from any initial to another predefined 3D point in the shortest possible time using any arbitrary trajectory; the ability to apply any angular value of the scanning step with the aim to achieve the novel theoretical possibility realize scanning with variable step size.
2. Novel geometrical strategy allows to perform the 3D scanning in non-discontinued way, where any of preliminary desired 3D point can be reached by the laser beam with predefined and adjusted during multiple experimentation uncertainty of scanning element positioning; this concept permits to eliminate the dead zones of previous prototype, i.e. to convert the discontinued FOV into continuous one.
3. Novel algorithm of continuous laser scanner opens the possibility of applications implementation, which previously were limited by the fixed step size or by the observed object. By using the continuous scanning element for positioning the laser beam, the positioning time is significant shortened, while keeping constant or decreasing the relative positioning error less than 1 per cent.
4. Novel formalism using the Routh Criterion proofs the stability of the DC motor continuous model laser scanning for different controller parameters and for different control loop configurations by simulation results and comparison. The frequency response of the continuous DC motor model gives information about the input and output behavior of the linear system in the frequency domain.

5. Digital control algorithm design for realization of DC motor control with the aim to perform a continuous laser scan of dynamic triangulation. The digital control algorithm was designed using various parameters and constants associated with real TVS functioning, and algorithms were defined for different control loop configurations.
6. Analytic comparison of several control algorithms in order to reach the optimization of laser beam propulsion under such criterions as the laser beam positioning accuracy / precision and step response rising time of the mechanical actuator.
7. To proof the several control algorithms to perform a continuous scan in the TVS field of view, extensive experimentations have been designed and realized, using Taguchi Statistical Method. The experimentation results are summarized in tabular form, analyzed in detail and used to optimize the different control algorithms for different control loop configurations.
8. Experimentations are proving the novel theoretical method for continuous laser scanning. Experimentation results show the possibility of positioning the DC motor shaft on any desired position in the TVS field of view, with minimal step response rising time and a minimal relative angular error.

12 Bibliography

[1] F. R. Helmert, Die mathematischen und physikalischen Theorien der Höheren Geodäsie (in German), Bd. 1, Leipzig: Teubner, 1880.

[2] H. Schlemmer und G. Mueller, Handbuch Ingenieurgeodäsie. Grundlagen (in German), Bd. 3, Herbert Wichmann Verlag, 2000, p. 642.

[3] K. Wendt, M. Franke and F. Härtig, "Measuring large 3D structures using four portable tracking laser interferometers," *Measurement,* vol. 45, pp. 2339 - 2345, December 2012.

[4] P. Morandi, F. Breman, P. Doumalin, A. Germaneau und J. Dupre, „New Optical Scanning Tomography using a rotating slicing for time-resolved measurements of 3D full field displacements in structures," *Optics and Laser in Engineering,* Bd. 58, pp. 85-92, July 2014.

[5] F. Li, A. P. Longstaff, S. Fletcher und A. Myers, „A practical coordinate unification method for integrated tactile-optical measuring system," *Optics and Lasers in Engineering,* Bd. 55, pp. 189-196, April 2014.

[6] G. Ma, B. Zhao und Y. Fan, „Non-diffracting beam based probe technology for measuring coordinates of hidden parts," *Optics and Laser in Engineering,* Bd. 51, pp. 585-591, May 2013.

[7] Y. Wang, B. Bhattacharya, E. H. Winer, P. Kosmicki, W. H. El-Ratal und S. Zhang, „Digital micromirror transient response influence on superfast 3D shape measurement," *Optics and Lasers in Engineering,* pp. 19-26, July 2014.

[8] D. Colombo, B. M. Colosimo und B. Previtali, „Comparison of methods for data analysis in the remote monitoring of remote laser welding," *Optics and Lasers in Engineering,* Bd. 51, pp. 34-46, January 2013.

[9] V. Flores, L. Casaletto, K. Genovese, A. Martinez, A. Montes und J. Rayas, „A Panoramic Fringe Projection System," *Optics and Lasers in Engineering,* pp. 80-84, July 2014.

[10] K. Genovese, L. Casaletto, J. Rayas, V. Flores und A. Martinez, „Stereo-Digital Image

Correlation (DIC) measurements with a single camera using a biprism,“ *Optics and Lasers in Engineering,* pp. 278-285, March 2013.

[11] Q. Sun, Y. Hou, Q. Tan und C. Li, „Shaft diameter measurement using a digital image,“ *Optics and Lasers in Engineering,* Bd. 55, pp. 183-188, April 2014.

[12] T. Toth and J. Zivcak, "A Comparison of the Outputs of 3D Scanners," in *24th DAAAM International Symposium on Intelligent Manufacturing and Automation, 2013,* Kosice, 2014.

[13] O. Y. Sergiyenko, „Optoelectronic System for Mobile Robot Navigation, Optoelectronics,“ *Instrumentation and Data Processing,* Bd. 46, pp. 414-428, 2010.

[14] Y. Zhongdong, W. Peng, L. Xiaohui and S. Changku, "3D laser scanner system using high dynamic range imaging," *Optics and Lasers in Engineering,* vol. 54, pp. 31-41, March 2014.

[15] N. Ohnishi und A. Imiya, „Appearance-based navigation and homing for autonomous mobile robot,“ *Image and Vision Computing,* Bd. 31, pp. 511-532, June - July 2013.

[16] R. Correal, G. Pajares und J. Ruz, „Automatic expert system for 3D terrain reconstruction based on stereo vision and histogram matching,“ *Expert system with application,* Bd. 41, pp. 2043-2051, March 2014.

[17] P. Kumar, C. P. McElhinney, P. Lewis und T. McCarthy, „An automated algorithm for extracting road edges from terrestrial mobile LiDAR data,“ *ISPRS Journal of Photogrammetry and Remote Sensing,* Bd. 85, pp. 44-55, November 2013.

[18] S. A. Hiremath, G. W. van der Heijden, F. K. van Evert, A. Stein und C. J. ter Braak, „Laser range finder model for autonomous navigation of a robot in a maize field using a particle filter,“ *Computers and Electronics in Agriculture,* Bd. 100, pp. 41-50, January 2014.

[19] G. Benet, F. Blanes, J. Simo and P. Perez, "Using infrared sensors for distance measurement in mobile robots," *Robotics and Autonomous Systems,* pp. 255-266, 30 September 2002.

[20] C. Volos, I. Kyprianidis and I. Stouboulos, "Experimental investigation on coverage performance of a chaotic autonomous mobile robot," *Robotics and Autonomous Systems,* vol. 61, no. 12, pp. 1314-1322, December 2013.

[21] L. C. Basaca-Preciado, O. Y. Sergiyenko, J. C. Rodriguez-Quinonez, X. Garcia, V. V. Tyrsa, M. Rivas-Lopez, D. Hernandez-Balbuena, P. Mercorelli, M. Podrygalo, A. Gurko, I. Tabakova and O. Starostenko, "Optical 3D laser measurement system for navigation of autonomous mobile robot," *Optics and Lasers in Engineering,* vol. 54, pp. 159-169, March 2014.

[22] L. C. Basaca-Preciado, J. C. Rodriguez-Quinonez, O. Sergiyenko, V. V. Tyrsa, W. Hernandez, J. I. Nieto Hipolito und O. Starostenko, „3D Laser Scanning Vision System for Autonomous Robot Navigation,“ in *Industrial Electronics (ISIE) International Symposium Bari*, 2010.

[23] L. C. Basaca-Preciado, J. C. Rodriguez-Quinonez, O. Sergiyenko, V. V. Tyrsa, W. Hernandez, J. I. Nieto Hipolito und O. Starostenko, „Resolution improvement of Dynamic Triangulation method for 3D Vision System in Robot Navigation Task,“ in *IECON 2010 – 36th Annual Conference on IEEE in Glendale Arizona*, 2010.

[24] L. C. Basaca-Preciado, O. Sergiyenko, J. C. Rodriguez-Quinonez und M. Rivas-Lopez, „Optoelectronic 3D Laser Scanning Technical Vision System based on Dynamic Triangulation,“ in *Photonics Conference (IPC) in Burlingame California*, 2012.

[25] O. Sergiyenko, L. Burtseva, M. Bravo, I. G. Rendon und V. Tyrsa, „Scanning Vision System For Mobile Vehicle Navigation,“ in *Electronics and Photonics Multiconferences in Guanajuato*, 2006.

[26] O. Sergiyenko, V. Tyrsa, D. Hernandez-Balbuena, M. Rivas-Lopez and L. Devia-Cruz, "Precise optical scanning for practical multi-applications," in *Industrial Electronics, 2008. IECON 2008. 34th Annual Conference of IEEE*, Orlando, 2008.

[27] O. Sergiyenko, V. Tyrsa, L. C. Basaca-Preciado, J. C. Rodriguez-Quinonez, W. Hernandez, J. I. Nieto-Hipolito, M. Rivas-Lopez und O. Starostenko, „Electromechanical 3D Optoelectronic Scanners: Resolution Constraints and Possible Ways of Improvement,“ in *Optoelectronic Devices and Properties*, InTech, 2011.

[28] W. Flores-Fuentes, M. Rivas-Lopez, D. Hernandez-Balbuena, O. Sergiyenko, J. C. Rodriguez-Quinonez, J. Rivera-Castillo, L. Lindner and L. C. Basaca-Preciado, "Applying Optoelectronic Devices Fusion in Machine Vision: Spatial Coordinate Measurement," in *Developing and Applying Optoelectronics in Machine Vision*, O. Sergiyenko and J. C. Rodriguez-Quinonez, Eds., Hershey, Pensilvania: IGI Global, 2016, p. 37.

[29] W. Flores-Fuentes, M. Rivas-Lopez, O. Sergiyenko y L. Lindner, «Barrido opto-electrónico para cuerpos macroscópicos en la infraestructura industrial (in Spanish),» de *ARGOS 2014*, Mexicali, 2014.

[30] W. Flores-Fuentes, O. Sergiyenko, F. Gonzalez-Navarro, M. Rivas-Lopez, J. C. Rodriguez-Quinonez, D. Hernandez-Balbuena, V. Tyrsa and L. Lindner, "Multivariate outlier mining and regression feedback for 3D measurement improvement in opto-mechanical system," *Optical and Quantum Electronics*, vol. 48, no. 8, p. 21, August 2016.

[31] W. Flores-Fuentes, J. C. Rodriguez-Quinonez, D. Hernandez-Balbuena, M. Rivas-Lopez, O. Sergiyenko, J. Rivera-Castillo, L. Lindner, L. C. Basaca-Preciado and P. Mayorga-Ortiz, "Photodiode and charge-coupled device fusioned sensors," in *2015 IEEE 24th International Symposium on Industrial Electronics (ISIE)*, Buzios, 2015.

[32] W. Flores-Fuentes, O. Sergiyenko, L. Lindner, M. Rivas-Lopez y J. Rodriguez-Quinonez,

«Tecnologías de Inteligencia Artificial en Colaboración con el Desarrollo de la Infraestructura Industrial (in Spanish),» de *ARGOS 2015*, Tijuana, 2015.

[33] L. Lindner, "Laser Scanners," in *Developing and Applying Optoelectronics in Machine Vision*, O. Sergiyenko and J. C. Rodriguez-Quinonez, Eds., Hershey, Pensilvania: IGI Global, 2016, p. 38.

[34] L. Lindner, O. Sergiyenko, J. Rodriguez-Quinonez und W. Flores-Fuentes, „Sustitución de motores de pasos con servomotores en triangulación dinámica de láser para escaneo continúo de coordenadas espaciales (in Spanish),“ in *ARGOS 2014*, Mexicali, 2014.

[35] L. Lindner, O. Sergiyenko, J. C. Rodriguez-Quinonez, M. Rivas-Lopez, D. Hernandez-Balbuena, W. Flores-Fuentes, F. N. Murrieta-Rico and V. Tyrsa, "Mobile robot vision system using continuous laser scanning for industrial application," *Industrial Robot,* vol. 43, no. 4, pp. 360-369, 2016.

[36] L. Lindner, O. Sergiyenko, M. Rivas-Lopez, B. Valdez-Salas, J. C. Rodriguez-Quinonez, D. Hernandez-Balbuena, W. Flores-Fuentes, V. Tyrsa, M. Medina Barrera, F. Muerrieta-Rico and P. Mercorelli, "UAV remote laser scanner improvement by continuous scanning using DC motors," in *Industrial Electronics Society, IECON 2016*, Florence, 2016.

[37] L. Lindner, O. Sergiyenko, M. Rivas-Lopez, J. C. Rodriguez-Quinonez, D. Hernandez-Balbuena, W. Flores-Fuentes, V. Tyrsa, J. I. Nieto Hipolito, F. N. Muerrieta Rico and V. M. Kartashov, "Issues of exact laser ray positioning using DC motors for vision-based target detection," in *2016 IEEE 25th International Symposium on Industrial Electronics (ISIE)*, Santa Clara, 2016.

[38] F. N. Murrieta Rico, V. Petranovskii, O. Raymond-Herrera, O. Sergiyenko, L. Lindner, D. Hernandez-Balbuena, J. C. Rodriguez-Quinonez, J. I. Nieto-Hipolito, W. Hernandez, P. Mercorelli and V. Tyrsa, "High resolution measurement of physical variables change for INS," in *2016 IEEE 25th International Symposium on Industrial Electronics (ISIE)*, Santa Clara, 2016.

[39] F. N. Murrieta-Rico, D. Hernandez-Balbuena, J. C. Rodriguez-Quinonez, V. Petranovskii, O. Raymond-Herrera, J. I. Nieto-Hipolito, O. Sergiyenko, L. Lindner, V. Tyrsa and V. I. Melnyk, "Instability measurement in time-frequency references used on autonomous navigation systems," in *2015 IEEE 24th International Symposium on Industrial Electronics (ISIE)*, Buzios, 2015.

[40] F. N. Murrieta-Rico, V. Petranovskii, O. Raymond-Herrera, O. Sergiyenko, L. Lindner, B. Valdez-Salas, D. Hernandez-Balbuena, J. C. Rodriguez-Quinonez, A. Gurko, P. Mercorelli and V. Tyrsa, "Resolution improvement of accelerometers measurement for drones in agricultural

applications," in *Industrial Electronics Society, IECON 2016*, Florence, 2016.

[41] F. N. Murrieta-Rico, O. Y. Sergiyenko, V. Petranovskii, D. Hernandez-Balbuena, L. Lindner, V. Tyrsa, M. Rivas-Lopez, J. I. Nieto-Hipolito and V. M. Karthashov, "Pulse width influence in fast frequency measurements using rational approximations," *Measurement,* vol. 86, pp. 67-78, May 2016.

[42] J. C. Rodriguez-Quinonez, O. Sergiyenko, L. C. Basaca-Preciado, V. V. Tyrsa, A. G. Gurko, M. A. Podrygalo, M. Rivas-Lopez und D. Hernandez-Balbuena, „Optical monitoring of scoliosis by 3D medical laser scanner,“ *Optics and Lasers in Engineering,* Bd. 54, pp. 175-186, March 2014.

[43] J. C. Rodriguez-Quinonez, O. Sergiyenko, F. F. Gonzalez-Navarro, L. C. Basaca-Preciado and V. Tyrsa, "Surface recognition improvement in 3D medical laser scanner using Levenberg–Marquardt method," *Signal Processing,* vol. 93, no. 2, pp. 378-386, February 2013.

[44] J. C. Rodriguez-Quinonez, O. Sergiyenko, V. V. Tyrsa, L. C. Basaca-Preciado y J. I. Nieto-Hipolito, «Monitoreo continuo de rehabilitación en pacientes con escoliosis utilizando barrido laser automático (in Spanish),» de *Health Care Exchanges (PAHCE) Conference Rio de Janeiro,* 2011.

[45] X. Garcia-Cruz, O. Y. Sergiyenko, V. Tyrsa, M. Rivas-Lopez, D. Hernandez-Balbuena, J. C. Rodriguez-Quinonez, L. C. Basaca-Preciado und P. Mercorelli, „Optimization of 3D laser scanning speed by use of combined variable step,“ *Optics and Lasers in Engineering,* Bd. 54, pp. 141-151, March 2014.

[46] W. Flores-Fuentes, M. Rivas-Lopez, O. Sergiyenko, F. F. Gonzalez-Navarro, J. Rivera-Castillo, D. Hernandez-Balbuena und J. C. Rodriguez-Quinonez, „Combined application of Power Spectrum Centroid and Support Vector Machines for measurement improvement in Optical Scanning Systems,“ *Signal Processing,* Bd. 98, pp. 37-51, May 2014.

[47] L. Lindner, O. Sergiyenko, V. Tyrsa und P. Mercorelli, „An approach for dynamic triangulation using servomotors,“ in *Industrial Electronics (ISIE), 2014 IEEE 23rd International Symposium on*, Istanbul, 2014.

[48] L. Lindner, O. Sergiyenko, J. Rodriguez-Quinonez, V. Tyrsa, P. Mercorelli, W. Fuentes-Flores, F. Murrieta-Rico and J. I. Nieto-Hipolito, "Continuous 3D scanning mode using servomotors instead of stepping motors in dynamic laser triangulation," in *Industrial Electronics (ISIE), 2015 IEEE 24th International Symposium on*, Buzios, 2015.

[49] R. Fischer, Elektrische Maschinen (in German), 12 Hrsg., Carl Hanser Verlag GmbH & Co. KG, 2003.

[50] H. Lindner, H. Bauer und C. Lehmann, Taschenbuch der Elektrotechnik und Elektronik (in

German), 7 Hrsg., Carl Hanser Verlag GmbH & Co. KG, 1999.

[51] "Faulhaber Drive Systems," Faulhaber, [Online]. Available: www.faulhaber.com. [Accessed 09 November 2016].

[52] "Maxon Academy," Maxon Motor, [Online]. Available: www.maxonmotor.com. [Accessed 09 November 2016].

[53] M. Schulze, Elektrische Servoantriebe: Baugruppen mechatronischer Systeme (in German), 1 Hrsg., Carl Hanser Verlag GmbH & Co. KG, 2008.

[54] R. Gohar and H. Rahnejat, Fundamentals Of Tribology, T. K. Wei, Ed., London: Imperial College Press, 2008, p. 450.

[55] V. Popov, Kontaktmechanik und Reibung (in German), 3 Hrsg., Berlin: Springer Vieweg, 2016, p. 397.

[56] K. Reinschke, Lineare Regelungs- und Steuerungstheorie (in German), 2. Auflage Hrsg., S. B. Heidelberg, Hrsg., Berlin, 2014.

[57] H. Lutz und W. Wendt, Taschenbuch der Regelungstechnik (in German), 9 Hrsg., Harri Deutsch, 2012, p. 1471.

[58] T. Lickteig and M.-F. Roy, "Cauchy index computation," in *Calcolo*, Pisa, Springer, 1996, pp. 337-351.

[59] K. Fuest und P. Doering, Elektrische Maschinen und Antriebe, 6. Auflage Hrsg., V. +. T. Verlag, Hrsg., 2004.

[60] S. J. Chapman, Electric Machinery Fundamentals, 4. Edition Hrsg., M. H. Education, Hrsg., 2005.

[61] J.-B. Song und K.-S. Byun, „Throttle actuator control system for vehicle traction control,“ *Mechatronics*, Bd. 9, Nr. 5, pp. 477-495, August 1999.

[62] S. E. Lyshevski, „Nonlinear control of mechatronic systems with permanent-magnet DC motors,“ *Mechatronics*, Bd. 9, Nr. 5, pp. 539-552, August 1999.

13 List of Publications

13.1 Indexed Journal Publications

[1] L. Lindner, O. Sergiyenko, J. C. Rodriguez-Quinonez, M. Rivas-Lopez, D. Hernandez-Balbuena, W. Flores-Fuentes, F. N. Murrieta-Rico and V. Tyrsa, "Mobile robot vision system using continuous laser scanning for industrial application," *Industrial Robot,* vol. 43, no. 4, pp. 360-369, 2016.

13.2 Book Chapter

[1] L. Lindner, "Laser Scanners," in *Developing and Applying Optoelectronics in Machine Vision*, O. Sergiyenko and J. C. Rodriguez-Quinonez, Eds., Hershey, Pensilvania: IGI Global, 2016, p. 38.

13.3 International Conferences

[1] L. Lindner, O. Sergiyenko, V. Tyrsa and P. Mercorelli, "An approach for dynamic triangulation using servomotors," in *Industrial Electronics (ISIE), 2014 IEEE 23rd International Symposium on,* Istanbul, 2014.

[2] L. Lindner, O. Sergiyenko, J. Rodriguez-Quinonez, V. Tyrsa, P. Mercorelli, W. Fuentes-Flores, F. Murrieta-Rico and J. I. Nieto-Hipolito, "Continuous 3D scanning mode using servomotors instead of stepping motors in dynamic laser triangulation," in *Industrial Electronics (ISIE), 2015 IEEE 24th International Symposium on*, Buzios, 2015.

[3] L. Lindner, O. Sergiyenko, M. Rivas-Lopez, J. C. Rodriguez-Quinonez, D. Hernandez-

Balbuena, W. Flores-Fuentes, V. Tyrsa, J. I. Nieto Hipolito, F. N. Muerrieta Rico and V. M. Kartashov, "Issues of exact laser ray positioning using DC motors for vision-based target detection," in *2016 IEEE 25th International Symposium on Industrial Electronics (ISIE)*, Santa Clara, 2016.

[4] L. Lindner, O. Sergiyenko, M. Rivas-Lopez, B. Valdez-Salas, J. C. Rodriguez-Quinonez, D. Hernandez-Balbuena, W. Flores-Fuentes, V. Tyrsa, M. Medina Barrera, F. Muerrieta-Rico and P. Mercorelli, "UAV remote laser scanner improvement by continuous scanning using DC motors," in Industrial Electronics Society, IECON 2016, Florence, 2016.

13.4 National Conferences

[1] L. Lindner, O. Sergiyenko, J. Rodriguez-Quinonez and W. Flores-Fuentes, "Sustitución de motores de pasos con servomotores en triangulación dinámica de láser para escaneo continúo de coordenadas espaciales," in ARGOS 2014, Mexicali, 2014.

[2] W. Flores-Fuentes, O. Sergiyenko, L. Lindner, M. Rivas-Lopez and J. Rodriguez-Quinonez, "Tecnologías de Inteligencia Artificial en Colaboración con el Desarrollo de la Infraestructura Industrial," in ARGOS 2015, Tijuana, 2015.

Appendix

Table 13-1: System parameters of selected DC Motors

Parameter	Unity	RE-max29	A-max16	GPM9	DCX22S
U_N	V	48	12	14.5	48
I_N	A	0.153	0.21	6.9	0.180
Ω_N	rpm	1820	4900	3000	4240
R_A	Ω	104	31.1	1.1	76.2
L_A	mH	8.46	1.13	n/a	4.08
K_E	-	0.0096	0.0322	0.9091	0.0131
T_E	ms	0.0813	0.0363	n/a	0.0535
K_T	$\frac{Nm}{A}$	0.168	0.0107	0.022	0.0772
r	$\frac{Nm}{rad/s}$	$2.71 \cdot 10^{-4}$	$3.673 \cdot 10^{-6}$	n/a	$7.827 \cdot 10^{-5}$
J_R	gcm^2	11.8	0.857	n/a	4.84
J_{Mi}	gcm^2	0.265	0.265	-	-

Table 13-2: Relative angular error average for 15 tests

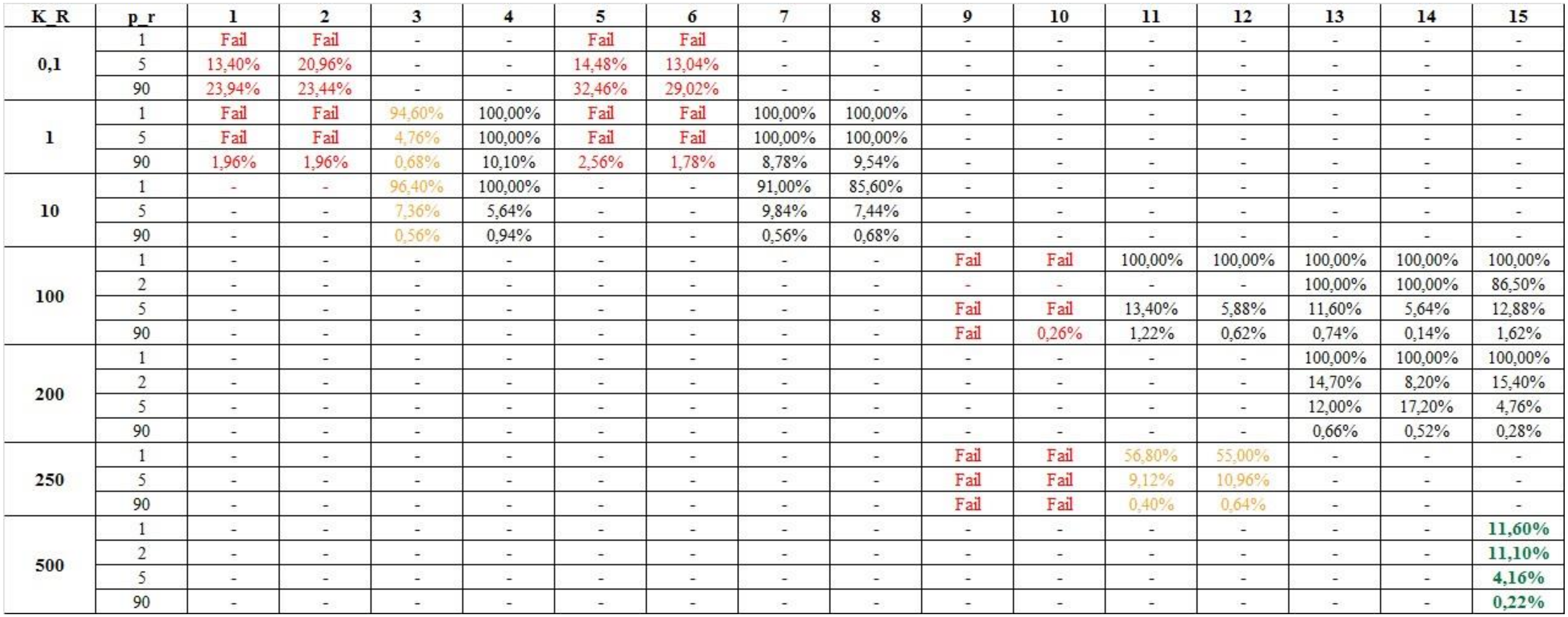

K_R	p_r	1	2	3	4	5	6	7	8	9	10	11	12	13	14	15
0,1	1	Fail	Fail	-	-	Fail	Fail	-	-	-	-	-	-	-	-	-
	5	13,40%	20,96%	-	-	14,48%	13,04%	-	-	-	-	-	-	-	-	-
	90	23,94%	23,44%	-	-	32,46%	29,02%	-	-	-	-	-	-	-	-	-
1	1	Fail	Fail	94,60%	100,00%	Fail	Fail	100,00%	100,00%	-	-	-	-	-	-	-
	5	Fail	Fail	4,76%	100,00%	Fail	Fail	100,00%	100,00%	-	-	-	-	-	-	-
	90	1,96%	1,96%	0,68%	10,10%	2,56%	1,78%	8,78%	9,54%	-	-	-	-	-	-	-
10	1	-	-	96,40%	100,00%	-	-	91,00%	85,60%	-	-	-	-	-	-	-
	5	-	-	7,36%	5,64%	-	-	9,84%	7,44%	-	-	-	-	-	-	-
	90	-	-	0,56%	0,94%	-	-	0,56%	0,68%	-	-	-	-	-	-	-
100	1	-	-	-	-	-	-	-	-	Fail	Fail	100,00%	100,00%	100,00%	100,00%	100,00%
	2	-	-	-	-	-	-	-	-	-	-	-	-	100,00%	100,00%	86,50%
	5	-	-	-	-	-	-	-	-	Fail	Fail	13,40%	5,88%	11,60%	5,64%	12,88%
	90	-	-	-	-	-	-	-	-	Fail	0,26%	1,22%	0,62%	0,74%	0,14%	1,62%
200	1	-	-	-	-	-	-	-	-	-	-	-	-	100,00%	100,00%	100,00%
	2	-	-	-	-	-	-	-	-	-	-	-	-	14,70%	8,20%	15,40%
	5	-	-	-	-	-	-	-	-	-	-	-	-	12,00%	17,20%	4,76%
	90	-	-	-	-	-	-	-	-	-	-	-	-	0,66%	0,52%	0,28%
250	1	-	-	-	-	-	-	-	-	Fail	Fail	56,80%	55,00%	-	-	-
	5	-	-	-	-	-	-	-	-	Fail	Fail	9,12%	10,96%	-	-	-
	90	-	-	-	-	-	-	-	-	Fail	Fail	0,40%	0,64%	-	-	-
500	1	-	-	-	-	-	-	-	-	-	-	-	-	-	-	**11,60%**
	2	-	-	-	-	-	-	-	-	-	-	-	-	-	-	**11,10%**
	5	-	-	-	-	-	-	-	-	-	-	-	-	-	-	**4,16%**
	90	-	-	-	-	-	-	-	-	-	-	-	-	-	-	**0,22%**

Table 13-3: Step response rising time average for 15 tests

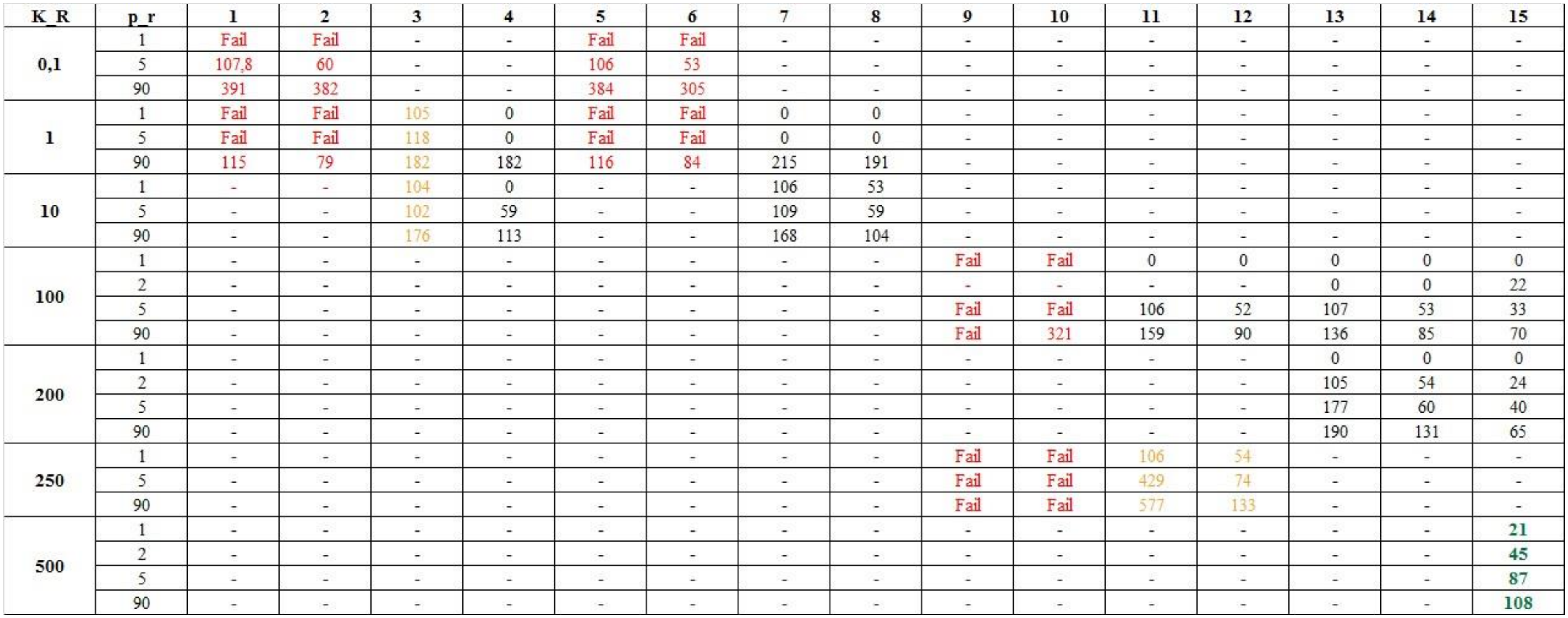

K_R	p_r	1	2	3	4	5	6	7	8	9	10	11	12	13	14	15
0,1	1	Fail	Fail	-	-	Fail	Fail	-	-	-	-	-	-	-	-	-
	5	107,8	60	-	-	106	53	-	-	-	-	-	-	-	-	-
	90	391	382	-	-	384	305	-	-	-	-	-	-	-	-	-
1	1	Fail	Fail	105	0	Fail	Fail	0	0	-	-	-	-	-	-	-
	5	Fail	Fail	118	0	Fail	Fail	0	0	-	-	-	-	-	-	-
	90	115	79	182	182	116	84	215	191	-	-	-	-	-	-	-
10	1	-	-	104	0	-	-	106	53	-	-	-	-	-	-	-
	5	-	-	102	59	-	-	109	59	-	-	-	-	-	-	-
	90	-	-	176	113	-	-	168	104	-	-	-	-	-	-	-
100	1	-	-	-	-	-	-	-	-	Fail	Fail	0	0	0	0	0
	2	-	-	-	-	-	-	-	-	-	-	-	-	0	0	22
	5	-	-	-	-	-	-	-	-	Fail	Fail	106	52	107	53	33
	90	-	-	-	-	-	-	-	-	Fail	321	159	90	136	85	70
200	1	-	-	-	-	-	-	-	-	-	-	-	-	0	0	0
	2	-	-	-	-	-	-	-	-	-	-	-	-	105	54	24
	5	-	-	-	-	-	-	-	-	-	-	-	-	177	60	40
	90	-	-	-	-	-	-	-	-	-	-	-	-	190	131	65
250	1	-	-	-	-	-	-	-	-	Fail	Fail	106	54	-	-	-
	5	-	-	-	-	-	-	-	-	Fail	Fail	429	74	-	-	-
	90	-	-	-	-	-	-	-	-	Fail	Fail	577	133	-	-	-
500	1	-	-	-	-	-	-	-	-	-	-	-	-	-	-	**21**
	2	-	-	-	-	-	-	-	-	-	-	-	-	-	-	**45**
	5	-	-	-	-	-	-	-	-	-	-	-	-	-	-	**87**
	90	-	-	-	-	-	-	-	-	-	-	-	-	-	-	**108**